1968

Surface reactions of C2, C3, and C4 hydrocarbons by field emission microscopy, field ion microscopy and flash filament spectroscopy

James William Gambell
Iowa State University

SURFACE REACTIONS OF C_2, C_3, AND C_4 HYDROCARBONS BY FIELD EMISSION MICROSCOPY, FIELD ION MICROSCOPY AND FLASH FILAMENT SPECTROSCOPY

by

James William Gambell

A Dissertation Submitted to the
Graduate Faculty in Partial Fulfillment of
The Requirements for the Degree of
DOCTOR OF PHILOSOPHY

Major Subject: Physical Chemistry

Approved:

Signature was redacted for privacy.

In Charge of Major Work

Signature was redacted for privacy.

Head of Major Department

Signature was redacted for privacy.

Dean of Graduate College

Iowa State University
Ames, Iowa
1968

TABLE OF CONTENTS

PHILOSOPHY OF SURFACE CHEMISTRY RESEARCH

Surface reactions of hydrocarbons have been extensively studied; yet, there seems no clear consensus as to even the basic steps in the hydrogenation of the simplest olefin, ethylene. If hydrogen and ethylene are to combine to form ethane, the transition state is presumably reached by hydrogen, in some form, reacting with ethylene, in some form. For a heterogeneous gas-solid reaction system there are four general pathways to the activated complex.

Table 1. General reaction mechanisms for the hydrogenation of ethylene

	Hydrogen from:	Ethylene from:	Investigator
1)	gas	gas	non-catalytic process
2)	surface	surface	Horiuti and Polanyi (1934) (46)
3)	gas	surface	Twigg and Rideal (1939) (137)
4)	surface	gas	Farkas and Farkas (1938) (32)

These are but general categories, each of which still has its proponents today, and each of which has, in turn, spawned innumerable sub-groups with slight modifications on the general idea. As pointed out by Brennan (1964), the approach used by early investigators was mainly kinetic in character (17)

> "Once again, the chief reason for this proliferation of reaction schemes has been ignorance of the nature of the adsorbed state under the conditions of the reaction. Recent work, in contrast, has been directed more to the problem of elucidating the adsorbed state and its relation to the reaction, although some interesting kinetic studies have also been made."

Brennan goes on to say that only by determining the nature of the adsorbed state can hope for eventual clarification of the problem be based. This view is to be contrasted with the statement of Bond only two years later (7).

> "The positive surface potential found for ethylene on nickel films also related to species of unknown structure, and infrared studies have been less helpful than might have been hoped in resolving these problems. Virtually nothing is known of the interaction of alkynes and diolefins with metal surfaces ... It is, in any event, doubtful whether species formed in such circumstances are those which participate in catalytic reactions, and more emphasis should be placed on indirect assessments of chemisorption strengths, arising from kinetic analysis of reacting systems."

These two statements point out most graphically philosophies of two opposing camps in surface chemistry studies. One large group of workers prefer to work with idealized systems, controlling as many variables as possible, while an even larger group of experimenters study the same type of reactions on catalytic surfaces more nearly equivalent to those in commercial use. An example from current catalytic literature will serve to illustrate the magnitude of the discrepancies in results between the two sides. Jenkins and Rideal observed, at room temperature on nickel films, extensive decomposition of ethylene accompanied by self-hydrogenation of ethylene to ethane (48). Selwood, on

the other hand, using a silica supported nickel catalyst inferred that room temperature ethylene adsorption was non-dissociative (127. No self-hydrogenation was observed. The latter experimenter summed up the feelings of far too many workers in the field today when he stated:

> "The adsorption of ethylene on nickel on silica is thus seen to proceed by a mechanism quite different from that observed on related adsorbent systems. It is doubtful if anything is to be gained by trying to relate the results on nickel on silica to those obtained on nickel films and wires ..."

I share in the despair many workers feel when viewing results obtained by physical techniques which probe the catalytic surface. If an indictment of those using physical methods must be made, however, it must be made on the basis that most physical studies have been conducted on poorly characterized surfaces. Another literature example will illustrate the importance of conducting surface studies on well-characterized surfaces. Roberts found that ethane cracked extensively on clean rhodium films at 27°C (118). The presence of surface oxygen, however, inhibited the cracking reaction, even at 100°C. Furthermore, the product formed in the latter case was mostly water; methane was the major gas phase product on the clean film at 27°C. A carbon monoxide monolayer completely blocked the decomposition reaction at 100°C.

Vacuums commonly employed by most workers are rarely better than 10^{-5} to 10^{-6} torr. The rate of impact of gas

molecules onto a plane surface is, from the kinetic theory of gases:

$$Z/cm^2 = P/\sqrt{2\pi mkT}. \qquad (1)$$

For $P = 10^{-6}$ torr, m = 28 amu, and T = 300°K, it is readily calculated that 3.8×10^{14} gas atoms strike each square centimeter of exposed surface each second. Since surface metal atom densities of $5\text{-}10 \times 10^{14}/cm^2$ are typical, any reasonable value for a sticking coefficient will result in substantial contamination of an initially clean surface in a few seconds.

Most catalyst systems never start from a clean state; i.e., there exists no treatment, thermal or chemical, by which a supported metal surface layer can be depleted of refractory contaminants. This is inferred both from experimental data, of which an example has been given, and also from the extreme difficulties encountered in cleaning surfaces employing the most elaborate ultra-high vacuum conditions. It is ironic that perhaps the two most widely used catalytic metals, nickel and platinum, prove to be among the toughest surfaces to clean (61, 62, 140).

It can be seen, from the discussion just presented, that there are two philosophies as to the kinds of surfaces on which to conduct experiments.

The "clean surface" approach starts with surfaces containing nothing but the desired metal. Most workers preferring this method are from the academic world or non-profit

research institutes. There are, of course, notable exceptions to this generalization, a large group at General Electric, another at Bell Telephone and a third with Shell in the Netherlands, to name but a few. Most industrial people, however, prefer to work with more "practical" surfaces, closer to those used in commercial processes. This generally means use of supported metal catalysts along with powders.

We have also seen a further large sub-division within both of these groups, one group employing direct physical observation of the reacting surface, another relying on kinetic analysis of products and reactants to determine the nature of the surface intermediates.

This writer believes it is imperative to begin studies on clean surfaces. If desired, contaminants can be added to the well-characterized surface in a controlled manner to approximate conditions on more practical catalysts. Evidence that small amounts of contaminants alter both the rate and course of a wide variety of catalytic reactions is too strong to be ignored. Determination of the surface species present on well-characterized metal surfaces should be the starting point in any fundamental analysis of a reaction system.

The possibility must be reckoned with, as noted by Bond, that the surface species may not be the intermediates in the reaction being studied. In rebuttal, it is important to realize that even if this is true, the nature of the predominant ad-species will determine the sites available for

those species which do participate in the reaction. In addition, it will often be possible to determine if the detected surface species is the "active" species.

Finally, it is also important to employ the kinetic approach after the nature of the surface species has been established. Knowledge of the ad-species present, however, provides a more sound basis for promulgating a reaction mechanism to conform to kinetic data. The hydrocarbon surface species detected by physical methods in this study moreover agree almost exactly with those predicted by experimenters employing commercial catalysts and kinetic methods.

FIELD ELECTRON EMISSION MICROSCOPY

Field Electron Emission from Metals

The field emission microscope (FEEM) is, in principle, a miniature television tube. The electron gun in the FEEM is a sharp metal tip of radius ≈1,000Å. Electrons are emitted from the tip when a potential difference of about 1,000 volts is applied between the tip and a conductive coating, on which the phosphor screen is bonded. A schematic of the type of tube employed in the present studies (with attendant electronic equipment) is shown in Figure 1.

After leaving the tip, the emitted electrons are in an essentially zero field region, and follow the radially directed electric lines of force to the phosphor screen. The electron image at the phosphor screen records the relative electron emitting characteristics of the various crystallographic regions on the tip. A field electron micrograph of a clean tungsten tip is shown in Figure 2. A cubic orthographic projection for a [110]-oriented tungsten emitter is shown in Figure 3. [110]-oriented, body-centered-cubic-, tungsten emission patterns possess two mirror planes. Planes with a given atom arrangement are duplicated, for example, by a mirror operation through a plane connecting the two axial {100} planes, or the two equatorial {111} planes. The symmetry of the tungsten field electron

image in Figure 2 has been used to indicate both crystal plane location (upper right hand portion) and work function values in eV (lower left).

Work Function

The electron image on the phosphor screen provides important ancillary information for adsorption processes. The parameter of primary interest, however, is the work function value itself. Work functions are computed from the relationship between applied voltage and emission current first derived by R. H. Fowler and L. Nordheim (34).

Theory

The physical model for electron emission from metals assumes no thermal contributions. Instead, electrons in the metal with energies close to the Fermi level tunnel through a potential barrier thinned by an image force potential, $-e^2/4x$, and action of the applied field, $-eFx$. This is shown in Figure 4 for tungsten. The result for current density, $J(amps/cm^2)$, in terms of work function, $\Phi(eV)$, and applied field, $F(V/cm)$, can be written as:

$$J = 1.54 \times 10^{-6} F^2/\Phi t^2(y) \exp. [(-6.83 \times 10^{-7} \Phi^{3/2}/F) f(y)] \quad (2)$$

$t(y)$ and $f(y)$ are slowly varying functions of F/Φ and are tabulated by van Oostrom (138). Under conditions pertinent to field electron microscope operation, $t(y)$ is nearly 1, while $f(y)$ varies between 0.5 and 0.75.

The experimentally encountered parameters are not J and F, but the total emission current, i(amp), and applied voltage, V(volts). These are related to J and F by:

$$i = J\,A \tag{3}$$

$$F = \beta\,V \tag{4}$$

A is the emitting area of the tip in cm^2, while β is a geometrical factor in cm^{-1} related to tip geometry. For tip radii larger than 500Å, β assumes a value of $1/5\,r$ (41).

The result of using Equations 3 and 4 in Equation 2 yields the desired dependence of the emission current on applied voltage.

$$i = 1.54\text{x}10^{-6}\beta^2V^2A/\Phi t^2(y)\ \exp.\ [(-6.83\text{x}10^{-7}\Phi^{3/2}/\beta V)f(y)] \tag{5}$$

A plot of $\ln(i/V^2)$ versus $1/V$, termed a Fowler-Nordheim plot (F-N plot), yields nearly a straight line with slope, s:

$$s = (-6.83\text{x}10^{-7}\Phi^{3/2}/\beta)\ s(y) \tag{6}$$

s(y) is a slowly varying function of F/Φ and assumes values between 0.94 and 0.97. If the image force is neglected, s(y) becomes 1 and a plot of $\ln(i/V^2)$ versus $1/V$ would be a straight line.

It can be seen from Equation 6 that a F-N slope yields a value for $\Phi^{3/2}/\beta$. Likewise, the intercept contains terms for $A\beta^2/\Phi$. To determine an absolute value for Φ, some independent measurement of Φ or β is required. Alternatively, two separate means for measuring the ratio of Φ/β are

needed. There are several ways available for tackling this problem:

1. From F-N plots alone, van Oostrom was able to show that Φ could be computed (138). He defined an operational parameter $K = s/V$ which was found to be nearly independent of Φ. This enables the current density, J, to be computed from any point on the F-N plot. The simple relationship between current density and emission current yields the emitting area, A. The second relationship involving Φ and β is found by eliminating A from the pre-exponential term in Equation 5. The F-N slope and intercept then give the two desired relations.

2. Total energy distributions of field emitted electrons yield a half-width value which is a function of $F/\Phi^{1/2}$, providing a second relationship between β and Φ (144).

Determination of work functions in the FEEM

There are many ways for obtaining relative values of Φ. In adsorption experiments only the value of Φ for the adsorbate covered surface relative to the clean metal surface value is desired. This is readily computed by comparing the F-N slopes for the two cases. It is assumed that β does not change during the adsorption process. For thermally annealed tips, appreciable changes in tip geometry are not observed in the temperature regions used in this study, 4°K to 800°K.

$$\Phi_{ads} = (s_{ads}/s_o)^{2/3} \cdot \Phi_o \qquad (7)$$

The work function for the clean tungsten surface, Φ_o, is assumed to be 4.50 eV from literature values. The work function of the adsorbate covered surface can then be computed from Equation 7.

An alternative approach, permitting work functions of adsorbate covered surfaces to be obtained without F-N plots, is the so-called "single point" method (126). The F-N relation, written as:

$$i = aV^2 \exp. [-b\Phi^{3/2}] \tag{8}$$

can be rearranged to yield:

$$V_{ads}/V_o = (\Phi_{ads}/\Phi_o)^{3/2} + V_{ads}/b_o\Phi_o^{3/2} \ln[a_oV_o^2/a_{ads}V_{ads}^2] \tag{9}$$

If the second term on the right hand side of Equation 9 is small compared to the first term, ($\leq$10%)

$$(V_{ads}/V_o) = (\Phi_{ads}/\Phi_o)^{3/2} \tag{10}$$

If $\Delta\Phi/\Phi_o = (\Phi_{ads} - \Phi_o)/\Phi_o \ll 1$, the right hand term of (10) can be expanded to yield:

$$(\Delta\Phi/\Delta V/V_o) \cong (2/3)\Phi_o = 3\text{eV for tungsten.} \tag{11}$$

The assumptions leading to Equation 11 should be experimentally justified before computing work functions by the single point method. This involves computing work functions for a given surface by both the F-N and single point method. For hydrocarbons, adsorbed on tungsten, the absolute value of Φ computed by the two techniques will not, in general, be equal. Experience, however, has shown that the trends

of the work function versus temperature curves for hydrocarbon decomposition reactions computed by the more accurate F-N method are mirrored in single point plots.

The voltage required to produce a given emission current for the clean surface, V_o, is recorded. After adsorption, or after a given operation on the adsorbed layer, the voltage needed to produce the same emission current, V_{ads}, is noted. Φ_{ads} is then computed from Equation 11. Emission currents of about 5×10^{-8} amps were generally chosen as the current to be reproduced in my work. This is well out of the range where electron bombardment of the screen evolves contaminant gases. This method has the advantage of being much quicker than taking data for F-N plots. For initial experiments with a given adsorbate-adsorbent system, the general features to be expected from the more precise F-N plot method could be anticipated. Data for trans-2-butene were taken in this manner and parallel those for the cis-2 isomer taken by the more time consuming method.

Nature of bulk work functions

The work functions measured in this study are termed "bulk" work functions. Each is an average value from the many crystallographic planes of the tip, weighted heavily toward those planes of lowest Φ, i.e.,

$$\bar{\Phi}^{3/2} = \sum_j (i_j/\bar{i}) \cdot (b_j/\bar{b}) \cdot \Phi_j^{3/2} \qquad (12)$$

For two different crystal planes of equal area, with different work functions, 4.5 eV and 5.0 eV, Equation 12 predicts the measured work function to be 4.51 eV. When using bulk work function values in surface studies it is important to realize that only tip areas with certain atom arrangements contribute to the measured work function. On tungsten, this means that the most densely packed planes, e.g., the {211}, {100} and {110} planes are not investigated in hydrocarbon decomposition experiments. The surface reactions investigated in this FEEM study are those which occur on the more open planes.

This could have serious implications if surface heterogeneity effects were so striking as to cause different reactions to occur on different sets of planes. This does not appear to be the case for hydrocarbon reactions on tungsten. For one thing, emission patterns of the associative adsorption of the 2-butene's and 1,3-butadiene displayed uniform emission indicating, at least on the set of high index planes sampled, that adsorption occurred uniformly. Secondly, flash filament data will be shown to correllate beautifully with field emission observations. The tungsten wires used in the flash filament experiments expose exclusively low index planes.

Relation of Φ_{ads} to properties of the ad-layer

Work function values for an adsorbate covered surface can be related to the chemical identity of the surface species

by the "condensor model" for the surface layer. Upon adsorption, the adsorbate molecules are pictured as forming a double layer of oriented dipoles. The result can be formulated as:

$$\Delta\Phi = 4\pi N \Theta H = 3.76 \times 10^{-15} N \Theta H \qquad (13)$$

With 5×10^{14} sites per cm^2 = N, and a surface ad-species dipole moment, H = 0.1 debye, Equation 13 implies that surface coverages of several hundredths of a monolayer can be detected. (This results since F-N data can reliably differentiate between work function differences of about 0.01 eV.) A surface species with a larger surface dipole moment could, of course, be detected at even lower coverages. Generally, field emission experiments detect only the product of surface coverage times surface dipole moment. If, however, means are available to determine the flux incident on the tip (and if the sticking coefficient for the process concerned is known) the surface dipole moment can be calculated from Equation 13.

In practice, surface adsorbate layers are found to increase or decrease the work function of an initially clean metal surface depending upon the chemical identity of the ad-species. For example, hydrogen gives rise to a positive $\Delta\Phi$ on tungsten, while olefins, diolefins and alkynes give a negative $\Delta\Phi$. The interpretation given the sign of the work function change assumes

$\Delta\Phi < 0$ implies a surface dipole positive out,

$\Delta\Phi > 0$ implies a surface dipole negative out.

From this, some idea as to the identity of the surface species arises. Thus for olefins, associative adsorption will be seen to give a negative work function change. This is interpreted as meaning that olefin adsorption involves opening of the hydrocarbon π-bond, electrons from the π-bond being partially transferred to the metal. Since hydrogen should also bond to transition metals by some form of electron sharing process, the positive work function change for hydrogen adsorption may seem non-tenable with the ideas expressed above. The answer to the difference between expected sign of the work function change and that observed is thought to be that hydrogen atoms are small enough to sit below the electronic surface, thus giving a negative dipole out.

Since a lower work function leads to enhanced electron emission from a given portion of the tip, it is again apparent that bulk work function values can possibly lead the observer astray. This could result, for example, if a surface process occurred on face A to give a rise in work function which did not occur on face B. If face A and face B initially had the same work function, any subsequent surface reactions on face A could conceivably be overlooked.

The usefulness of bulk work function measurements is that <u>if</u> a work function change does occur during an experiment, one

of two things must have occurred:

1) the number of ad-species have either increased or decreased in number or

2) the chemical identity of the surface species has changed.

It is unfortunate that so many writers have seen fit to deprecate the value of bulk work functions. This viewpoint is perhaps legitimate when the adsorbate is a simple diatomic gas. In this case, the thrust of the investigation is likely to be toward establishing the presence of different binding states, absolute values of the surface dipole moment, etc. When working with hydrocarbons, however, the information desired is of a different nature. For example, in the present work, the most important single piece of information is the thermal stability of the ad-species. The change in work function observed on heating ad-layers to increasingly higher temperatures rather unambiguously signals when surface reactions have occurred. In combination with flash filament experiments, which monitor appearance of products in the gas phase as a function of temperature, the nature of the hydrocarbon surface reactions can be rather elegantly followed.

The validity of the F-N relation for determining the work function of clean metal surfaces has been experimentally verified many times. The case for determining work functions for adsorbate covered surfaces is not nearly so complete. In his 1963 review article on field emission, Ehrlich

discusses the problems involved and concludes that work functions determined from F-N plots are valid within experimental error (1%) (25). Van Oostrom arrives at the same conclusion in a 1966 treatment of the problem (138). Gardner and others have considered the effect of different barrier shapes to electron emission, introduced by different types of adsorbates (25,36). For situations likely to be met in practice the field dependence of the emission current was found to yield the correct work function value.

Experimental Procedures

Conductive coating

A schematic of the type of field emission microscope used in these studies was shown in Figure 1. The tube itself was fashioned from a 125 ml round bottom flask. This size would fit nicely into the liquid helium cryostat inner dewar. The complete microscope-to-be, minus the two press seals, was first rinsed in 10% ammonium bi-fluoride (by weight) solution. The port to the cold finger was plugged with glass wool and the tube heated to 525°C in an annealing oven. Places where glass blowing seals were to be made could be covered with a suspension of platinum paint to prevent stannous oxide formation. It proved possible, however, to make seals through a stannous oxide layer, and since removal of the platinum paint (by dipping in the ammonium bi-fluoride solution) was a tedious task, the protective coating was ordinarily omitted.

Stannous oxide coatings were applied by blowing nitrogen over a stannic chloride solution, entraining $SnCl_4$ vapor in the nitrogen stream. The nitrogen-$SnCl_4$ stream was then joined to a stream of air or oxygen as shown in Figure 5. Transparent stannous oxide coatings with suitable resistances were more readily obtained if a trace of water was present in the air line. The presence of a small amount of water was quite striking. The coating process at 525°C required several seconds with water present; without water, several minutes were required and the coatings produced were generally inferior.

Phosphor screens

After cooling back to room temperature, the resistance of the conductive coating was checked (generally resistances of $\leq$500 ohms per centimeter of screen were obtained). If satisfactory, the application of screen phosphor was begun. The method described by Gomer was used (41). Ten small glass beads were placed inside the tube and six drops of a solution of ten drops of phosphoric acid in five ml of acetone were dropped onto the glass beads. The solution was spread around the face of the tube within the confines of the future phosphor screen after which the beads were dumped out and the acetone allowed to evaporate. The tube was then clamped so that the screen-to-be was in the vertical plane and phosphor was puffed onto the phosphoric acid coated tube areas with an atomizer bulb as described by Gardner (36). Sylvania

zinc ortho-silicate phosphor #221 was generally used (a P-1 phosphor, Willemite) and proved to have excellent properties for puffing. An earlier P-1 zinc-ortho-silicate phosphor, #160, from the same distributor, never gave decent screens without a great deal of effort (see Field Ion section). Excess phosphor was removed by blowing a vigorous stream of dry air in the tube and screen preparation was completed by baking in an annealing oven at 400°C for one hour.

Electrical connections to conductive coating

The next step was to make electrical connection to the stannous oxide coating. This was accomplished in the fashion described by Gardner (36). Tungsten hair springs, made from five mil tungsten wire, were spotted onto a 1-lead nickel press seal. When the press seal was glass blown onto the small side arm of the flask, the hair springs made contact with the conductive coating (Figure 6). The resistance path from the outside of the tube to the conductive screen was checked to complete this operation.

Extreme care was exercised to prevent sharp edge formation on any metal parts which were to go inside the microscope to avoid spurious emission. All nickel, nichrome or chromel wires were a.c. etched in aqueous HCl, tungsten in aqueous KOH, while platinum pieces were flamed to smooth any rough edges.

Tip etching

Tungsten tips were etched in the manner originally given by Gomer (41). Generally, a two inch segment of 5 mil tungsten wire (supplied by Phillips-Elmet) was a.c. etched in 1 N aqueous KOH to perhaps 1/10 to 1/5 of its original diameter. About 1/2 inch of the thinned end of the wire was cut off and the remaining longer piece spot welded onto a 10 mil tungsten loop fashioned in the shape of an elongated U. The spot welder employed was purchased from Unitek (Unitek-Weldmatic, Model 1059B, Dual Range). Power dissipated during spot welding was variable up to 40 watt-seconds while discharging pressure at the electrodes was variable up to about 300 grams. Tungsten-based electrodes were found most convenient for making spot welds with small pieces of tungsten. The small end of the etched tungsten segment was spotted at ~25 grams pressure and 0.8-1 watt-seconds.

The tip fashioning operation was continued by placing the ~1 - 1/2 inch section vertically into the etchant. The tip loop was conveniently held by a micro-manipulator to facilitate positioning. A schematic of the tip etching process is shown in Figure 7. The meniscus of the solution at the wire was placed near, but not snug up-against, the 10 mil support loop and etching was initiated at just above the voltage setting required for gas evolution. When the wire had thinned to a point where rupture appeared imminent, (as judged by a fluttering movement of the lower portion of the

immersed wire) the tip assembly was lowered slightly into the etchant. Rupture usually occurred within five seconds, at which time the variac was turned off and the tip assembly removed from the micro-manipulator. The variac was turned back on at a slightly higher voltage setting and the whole tip assembly, loop and all, was dipped into the etchant several times in a rapid in-out sequence. The latter operation served to remove any strained material which might have been caused by gas evolution during etching, or by the act of wire rupture.

This operation almost always yielded sharp tips with smooth tapers when viewed in a light microscope at 500 magnification. If the taper was gradual and the tip end not visible, the tip was suitable for field electron emission experiments. A washing of the whole tip assembly in distilled water completed the etching operation.

Rhodium tips were conveniently a.c.-etched in a 10% (wt.) aqueous solution of potassium chloride. 5 mil rhodium wire was first spot-welded onto a 10 mil tungsten loop. Tip etching was initiated by inserting the rhodium segment into the etchant. Since rhodium tips were not formed via rupture of the wire, as in the case of tungsten, shorter segments of rhodium wire could be used. A 1 cm section was generally used which thinned and shortened when etched at settings a bit above the point required for gas evolution. Clean field emission patterns of rhodium tips etched in this manner

generally were obtained at 1000 to 1,500 volts. For decomposition studies tungsten support loops are undesirable. In this case, 10 mil rhodium wire, d.c. annealed at roughly 2/3 the melting point of rhodium to remove impurities such as silicon and oxygen, must be employed.

Tip support assembly

A four lead tungsten press seal was adapted by spotting a 0.5 cm section of 40 mil nickel to the tungsten rods. A 1 cm section of 20 mil nichrome was then spotted onto the nickel. The nickel segment was used as it was discovered that nickel spotted easily to tungsten while nichrome did not. The higher resistance nichrome segment served as a thermal barrier between the tip segment and outside leads which were generally at 4°K. Small changes in current at low temperatures would produce large changes in temperature if the tungsten loop were spotted directly to the press seal leads, due to the very large thermal conductivities of pure metals at low temperatures.

The 10 mil tungsten tip loop was spotted onto the nichrome inserts at 100 grams pressure and 4 watt-seconds. 5 mil tungsten segments, containing a single spiral to accommodate stresses, were then spotted onto the remaining two nichrome inserts at 100 grams and 2 watt seconds. The other end of the 5 mil tungsten segments were then spotted to the tip support loop at 30 grams pressure and 2 watt-seconds, tapping off approximately a 2 cm length equally distributed on both

sides of the tip. When a heating current was passed through the tip-loop, the voltage drop sensed across the end segment of the tip loop nearest the tip gave the segment resistance, hence the tip temperature.

The final process in preparing the tip assembly was to etch the four spot welds just described. This was conveniently accomplished by inserting a metal wire through the rubber bulb of an eye dropper and running it near the bottom of the dropper tube. The eye dropper was filled with etchant and a complete electrical circuit could be made when a drop of etchant hung on the end of the eye dropper and contacted the spot weld. After washing the whole assembly in distilled water and drying it for a short period, the glass seal between microscope and press seal (containing the tip assembly) was made. It is not possible to check for leaks with a Tesla coil at this juncture as the electrostatic coil "pops" the small tips. For this reason, the seals for the high voltage lead-in and tip assembly were generally made prior to applying the stannous oxide coating. A new break was made prior to conductive coating application, which facilitated fitting the pieces back together again later and ensured against the possibility of leaks.

Gas handling

The completed microscope tube was attached to an ultra-high vacuum system and baked out overnight at ~400°C. While the oven was still hot, the tip assembly was partially outgassed, after which the system was allowed to cool to room temperature. Generally pressures of 5×10^{-8} to 1×10^{-9} were obtained without adding a final trap. A one-inch UHV valve was closed to seal the microscope section off from the pumps and the desired hydrocarbon was admitted into the baked portion of the vacuum system through a variable leak valve.

The hydrocarbons used in the studies described in this report (field electron emission and flash filament) are listed in Table 2 with their cracking patterns from API Research Project 44 tables and those obtained with the G. E. Partial Pressure Analyzer used in the present work.

Generally, about 10 torr of gas was admitted into the baked portion (~500 cc) as measured by a Hastings Model SP-1C controller (DV-4D gauge). Liquid nitrogen was then added to the outer dewar of the microscope to freeze the hydrocarbon onto the inner cold finger of the tube and the valve to the pumps was reopened to pump away non-condensable gases. Outgassing of the phosphor screen with a hot air gun followed, after which the tube was allowed to cool slightly before the thick walled tubing connecting the microscope to the vacuum system was collapsed. This procedure undoubtedly resulted in a significant surface contamination of the hydrocarbon deposit

Table 2. Cracking patterns. [Experimental/API Research Project 44][a]

Hydrocarbon/ Mass Number	1	2	12	13	14	15
Methane [a]	3.4	0.2	2.8	8.1	16.1	85.9
Ethane [a,b]	2.6	0.3	0.5	1.2	3.4	4.6
Ethylene [a,b]	4.1	0.5	2.1	3.5	6.3	0.6
Acetylene [a]	-	-	2.5	5.6	0.2	-
Propane [a,b]	2.0	0.1	0.4	0.7	2.1	6.2
Propylene [a,b]	3.7	0.4	1.3	1.8	3.6	5.4
Methyl Acetylene	16.3	8.1	3.0	2.7	2.6	6.3
	-	-	3.9	3.3	1.9	1.1
Allene	23.2	5.0	3.8	3.1	4.7	tr
	-	-	4.1	3.4	4.0	0.3
n-Butane [b]	3.2	-	3.0	0.1	0.2	0.9
	1.1	-	0.1	0.1	0.3	1.0
iso-Butane [a,b]	1.0	0.1	0.1	0.3	1.2	6.4
1-Butene [b]	8.4	10.6	0.4	0.4	1.3	5.3
	1.7	0.2	0.4	0.6	1.7	4.4
2-Butene	11.0	3.1	0.3	0.3	1.6	7.2
(cis- and trans-) [b]	2.1	0.3	0.4	0.5	1.1	4.2
iso-Butylene [b]	6.5	11.9	0.4	0.6	2.0	5.4
	1.9	0.2	0.4	0.7	1.9	4.9
Ethyl Acetylene	13.6	14.4	2.1	2.0	3.3	9.3
	3.8	0.9	1.7	1.8	2.4	5.3
1,3-Butadiene [b]	8.0	6.7	1.3	0.9	2.1	1.5
	3.9	0.4	1.6	1.7	2.7	1.8

[a] Where only one set of numbers is given, they refer to the API Table value.

[b] Phillips Research Grade Hydrocarbons, all others-technical grade.

Table 2. (Continued)

Hydrocarbon/ Mass Number	16	19	19.5	20	25	25.5	26
Methane	100.0	-	-	-	-	-	-
Ethane	0.1	--	-	-	4.1	-	23.0
Ethylene	-	-	-	-	11.7	-	62.3
Acetylene	-	-	-	-	20.1	-	100.0
Propane	0.2	1.1	0.6	1.1	0.8	-	8.6
Propylene	0.2	3.2	2.0	2.4	2.2	-	10.5
Methyl acetylene	0.5	2.9	2.3	0.8	3.4	-	3.5
	0.1	3.8	2.7	0.9	4.3	-	3.4
Allene	tr	3.3	3.9	3.9	4.4	-	5.3
	tr	3.1	3.9	3.8	4.6	-	4.8
n-Butane	5.8	-	-	-	tr	-	6.9
	5.3	-	-	-	0.5	-	6.2
iso-Butane	0.2	0.1	tr	tr	0.2	0.2	2.4
1-Butene	2.4	-	-	-	1.1	-	12.9
	0.1	-	-	-	1.2	-	10.1
2-Butene (cis-	0.2	-	-	-	1.7	-	18.0
and trans-)	0.1	-	-	-	1.6	-	12.6
iso-Butylene	0.4	-	-	-	0.8	0.8	6.2
	0.1	-	-	-	0.8	1.0	5.4
Ethyl Acetylene	0.8	1.1	-	-	4.7	2.5	22.9
	0.1	tr	-	-	4.2	3.6	14.8
1,3-Butadiene	0.3	-	-	-	3.3	2.5	23.1
	tr	-	-	-	4.4	4.0	25.7

Table 2. (Continued)

Hydrocarbon/ Mass Number	27	28	29	30	31	32
Methane	-	-	-	-	-	-
Ethane	33.3	100.0	21.7	26.2	0.5	-
Ethylene	64.8	100.0	2.2	-	-	-
Acetylene	2.8	0.2	-	-	-	-
Propane	39.4	59.1	100.0	2.2	-	-
Propylene	38.3	1.3	-	-	-	-
Methyl Acetylene	1.8	9.9	5.4	tr	0.5	-
	0.8	0.3	tr	tr	tr	-
Allene	1.3	8.4	-	-	-	-
	0.7	0.2	-	-	-	-
n-Butane	43.1	37.9	46.7	1.0	-	tr
	37.1	32.6	44.2	1.0	-	tr
iso-Butane	27.8	2.6	6.2	0.1	-	-
1-Butene	38.5	36.0	20.0	0.5	-	-
	30.0	29.5	13.1	0.5	-	-
2-Butene (cis- and trans-)	45.6	41.0	22.4	0.5	-	-
	33.4	31.7	15.6	0.7	-	-
iso-Butylene	24.7	27.5	12.5	0.9	-	-
	20.6	21.5	10.8	0.5	-	-
Ethyl Acetylene	54.2	51.2	12.1	0.7	18.3	tr
	41.2	34.5	1.1	-	-	-
1,3-Butadiene	62.8	47.7	1.1	-	-	-
	67.9	45.6	1.0	-	-	-

Table 2. (Continued)

Hydrocarbon/ Mass Number	36	37	38	39	40	41
Methane	-	-	-	-	-	-
Ethane	-	-	-	-	-	-
Ethylene	-	-	-	-	-	-
Acetylene	-	-	-	-	-	-
Propane	0.5	3.4	5.3	17.0	25.0	12.7
Propylene	2.4	13.6	14.3	71.1	28.9	100.0
Methyl Acetylene	7.7	27.6	38.0	91.4	100.0	3.9
	9.7	28.0	36.1	92.5	100.0	3.1
Allene	9.8	35.8	45.0	94.2	100.0	4.5
	9.4	32.6	40.5	96.2	100.0	3.3
n-Butane	-	1.0	2.4	17.5	2.9	38.2
	-	1.0	1.9	12.5	1.6	27.8
iso-Butane	0.1	1.4	2.8	16.5	2.4	38.1
1-Butene	0.2	3.0	5.7	46.3	9.8	100.0
	0.3	2.9	4.5	34.5	6.4	100.0
2-Butene (cis- and trans-)	0.5	4.6	9.8	52.6	16.8	100.0
	0.3	3.0	4.5	35.8	6.6	100.0
iso-Butylene	0.2	3.8	8.0	55.1	13.8	100.0
	0.4	4.2	6.6	43.7	10.2	100.0
Ethyl Acetylene	1.3	10.5	17.3	89.9	4.4	6.4
	1.6	8.8	14.6	76.3	2.5	tr
1,3-Butadiene	0.9	6.1	8.3	100.0	3.7	1.0
	1.2	6.2	7.5	100.0	3.4	0.1

Table 2. (Continued)

Hydrocarbon/ Mass Number	42	43	44	45	46	47
Methane	-	-	-	-	-	-
Ethane	-	-	-	-	-	-
Ethylene	-	-	-	-	-	-
Acetylene	-	-	-	-	-	-
Propane	5.8	22.3	29.0	0.9	-	-
Propylene	67.7	2.2	tr	-	-	-
Methyl Acetylene	tr 0.1	tr tr	tr =	tr =	tr =	tr =
Allene	- -	- -	- -	- -	- -	- -
n-Butane	17.4 12.2	100.0 100.0	3.5 3.3	tr tr	- -	- -
iso-Butane	33.5	100.0	3.3	tr	-	-
1-Butene	3.7 3.5	- -	- -	- -	- -	- -
2-Butene (cis- and trans-)	4.4 3.3	- -	- -	- -	- -	- -
iso-Butylene	3.8 3.6	0.2 0.1	- -	- -	- -	- -
Ethyl Acetylene	1.2 -	3.2 -	0.5 -	10.6 -	tr -	- -
1,3-Butadiene	- -	- -	- -	- -	- -	- -

Table 2. (Continued)

Hydrocarbon/ Mass Number	48	49	50	51	52	53
Methane	-	-	-	-	-	-
Ethane	-	-	-	-	-	-
Ethylene	-	-	-	-	-	-
Acetylene	-	-	-	-	-	-
Propane	-	-	-	-	-	-
Propylene	-	-	-	-	-	-
Methyl Acetylene	tr	tr	.5	tr	tr	0.9
	-	-	-	-	-	-
Allene	-	-	-	-	-	-
	-	-	-	-	-	-
n-Butane	-	tr	1.5	1.3	tr	1.1
	-	0.4	1.3	1.1	0.3	0.7
iso-Butane	-	-	-	-	-	-
1-Butene	0.2	2.1	8.1	7.0	2.3	9.7
	0.3	1.5	4.8	3.9	1.2	5.2
2-Butene (cis- and trans-)	0.4	3.3	11.6	10.1	3.9	13.5
	0.4	2.1	6.8	5.8	1.8	7.4
iso-Butylene	0.2	1.6	6.2	5.3	1.4	5.6
	0.3	1.6	5.3	4.4	1.2	5.0
Ethyl Acetylene	1.2	8.9	27.6	23.7	9.8	46.7
	1.7	8.0	22.4	18.8	7.6	43.0
1,3-Butadiene	1.1	6.4	25.2	23.4	10.4	49.7
	1.6	8.2	24.5	21.7	10.6	59.3

Table 2. (Continued)

Hydrocarbon/ Mass Number	54	55	56	57	58	59
Methane	-	-	-	-	-	-
Ethane	-	-	-	-	-	-
Ethylene	-	-	-	-	-	-
Acetylene	-	-	-	-	-	-
Propane	-	-	-	-	-	-
Propylene	-	-	-	-	-	-
Methyl Acetylene	2.0	-	-	-	-	-
	-	-	-	-	-	-
Allene	-	-	-	-	-	-
	-	-	-	-	-	-
n-Butane	tr	1.2	1.0	2.8	17.0	0.8
	.2	0.9	0.7	2.4	12.3	0.5
iso-Butane	-	-	-	-	-	-
1-Butene	4.1	2.5	49.7	2.2	-	-
	2.4	1.8	37.0	1.6	-	-
2-Butene (cis- and trans-)	7.9	33.9	56.6	3.1	-	-
	3.8	22.1	47.9	2.1	-	-
iso-Butylene	1.4	18.2	44.5	2.0	tr	-
	2.3	16.1	42.8	1.9	tr	-
Ethyl Acetylene	100.0	4.9	0.5	tr	7.3	0.5
	100.0	4.3	0.1	-	-	-
1,3-Butadiene	72.3	3.7	0.5	-	-	-
	85.9	3.8	0.1	-	-	-

as confirmed by the fact that often initial doses from the cold finger deposit gave slightly different results from subsequent doses. In these cases, the first data obtained were discarded.

Liquid helium cryostat

Cryostat design A schematic of the type of cryostat used in these studies is shown in Figure 8. While loading the hydrocarbon into the microscope the cryostat was readied for operation. This consisted of taking the head off and replacing it with a large rubber stopper. The inner dewar space was then roughed out through port C with a fore-pump. The vacuum jacket around the inner space was roughed out through port D with another pump. Before filling the space between the inner and outer dewar with liquid nitrogen, the vacuum jacket around the inner dewar was flushed several times with dry nitrogen and pumped out again to get rid of any helium which might have entered this space. All gases but hydrogen and helium would condense in this space with liquid helium in the inner dewar. A trace of helium, however, would transfer heat from the nitrogen cooled side of the inner dewar to the inner dewar walls resulting in excessive helium boil-off. Nitrogen was added to the dewar jacket a final time but not pumped out completely. When liquid nitrogen was now added to the space between the two dewars, the nitrogen gas helped to cool the inside wall of the inner dewar.

Cryostat operation The head, containing the electrical lead-throughs (I), port for transfering liquid helium (A) and high voltage lead-in (B) was supported during this time on the cryostat stand. The microscope was attached to the 10 mm O.D. evacuated glass tubing enclosing the high voltage lead through a 1/4 inch thick teflon block. Holes were cut in the teflon to accommodate the dewar of the microscope and the high voltage protective shield. The two pieces were fastened securely together by tightening nylon set screws.

Electrical connections were made from the high voltage lead to the press seal connected to the conductive coating. Connections to the tip assembly, i.e. current and monitor leads, were then made. To facilitate identification of these leads, the two current leads were always made of thicker copper wire than the monitor leads. The copper wire itself was lacquered and all four leads were shielded inside the cryostat by encasing them in braided nickel sleeving which was held at ground.

At this point, the room temperature resistance of the tip segment was measured by passing a 1 ma. test current through the heating leads and recording the voltage drop across the end of the tip loop. Liquid nitrogen was still in the microscope dewar, but independent experiments showed this to have no detectable effect on the resistance.

The final electrical connection made was to a small resistance heater placed in the bottom of the cold finger. The heater itself consisted of a high resistance alloy such as nichrome or chromel and was encased in a ball of Sauereisen high temperature cement to fit snugly against the inner dewar walls.

To insert the microscope tube into the inner dewar, the inner space was brought back to atmospheric pressure with a stream of helium. With the helium flow uninterrupted, the rubber stopper was removed and replaced with the cryostat head containing the microscope. The head was bolted down and the inner space evacuated to remove the liquid nitrogen in the microscope dewar. This generally required several hours, a time which conveniently was used to warm up electrical equipment.

The double dewar assembly was surrounded by a brass container which acts as a protective shield for the larger (~5 feet tall) glass dewars. When grounded, it also served as a shield against extraneous fields.

When the nitrogen was completely removed from the inner space, liquid helium was transferred through port A. The inner space held ~5 liters. Normal helium consumption, including losses during transfer, rapid boil-off during tip cleaning, and boil-off during data taking generally amounted to 10-12 liters per five hour experiment.

Tip-temperature controller Ordinarily, with a new tip installed, the first operation was to calibrate dial setting on the tip-temperature controller versus tip temperature. The Kelvin-Double Bridge controller used is shown in schematic form in Figure 9. The calibration procedure amounted to measuring current supplied to the tip loop versus voltage drop across the tip-segment tapped off by the monitor leads on an X-Y recorder. The recorder employed was a Moseley Autograf Model 7000A.

Tip cleaning Next, the tip was cleaned by flashing the tip loop to successively higher temperatures with a d.c. current supply which supplied up to 10 amps. Generally about 5-6 amps sufficed to produce a clean emission pattern at this initial stage. The emission pattern was checked after each flash. The criteria for a clean pattern are two:

1. a general lack of detail with uniform intensity for the emitting areas. Gradations between emitting and non-emitting areas should be gradual with the boundaries non-distinct.
2. The clean pattern must be retained after heating intervals through various temperature regions up to the temperature required for cleaning. The temperature interval where diffusion of impurities from the bulk occurs must be observed with particular care (about (800-1600°K for tungsten).

The initial cleaning generally was a simple process as the primary contaminants are surface oxides which decompose above ~2200°K. After hydrocarbons have decomposed on the tip, however, a surface carbide is left which is much more difficult to remove. Figure 10 presents a portion of the tungsten-carbon phase diagram. Two stoichiometric tungsten-carbon compounds are present, W_2C and WC. WC is stable only at lower temperatures, but W_2C is decomposed only at temperatures of 3000°K or higher. Since the melting point of tungsten is greater than 3600°K, this need pose no problem as long as the tip can be heated to temperatures higher than 3000°K.

Taking of Fowler-Nordheim data The next operation is to take F-N data for the clean surface. This involves measuring the voltages required to produce emission currents over the range $1x10^{-8}$ to $5x10^{-10}$ amps. The high voltage power supply used was a calibrated Fluke, model 410B, the voltage being measured directly from the decade dials. Currents were measured with either a Keithley model 610B electrometer or its battery operated equivalent, Keithley model 601. The F-N slope was then computed via a computer program designed by R. R. Frost and J. B. Condon.

Tip dosing Hydrocarbon adsorption studies were begun by distilling a fraction of the frozen hydrocarbon from the cold finger onto the tip. In practice, this required a hit and miss approach wherein the current supplied to the

heating element in the microscope dewar was increased very gradually until adsorption could be detected. With a hydrocarbon which had not been run before, initial experiments were performed with the high voltage set to provide a current of 5×10^{-8} amps. Adsorption was indicated by a increase in emission current. This is an interesting observation in itself, for an increase in emission current at constant voltage can only be interpreted as chemisorption. Physisorbed gas acts as a dielectric layer giving a current decrease. An essentially instantaneous chemisorption process at 4°K implies an adsorption process with an activation energy no greater than 1 Kcal/mole.

Molecular images If the dosing interval was too long, the emission current dropped again, indicating a work function increase. This is due to multilayer formation or physisorption. In general, multilayer adsorption had to be handled carefully as it often gave rise to "molecular images". Molecular images, m.i., are thought to result from individual molecules or groups of molecules. Since the resolution of the FEEM is only 20Å, resolution of individual molecules may seem impossible. There is, in fact, no contradiction for the resolution limit for resolving two image points is computed mainly by considering the transverse electron velocity in a metal (perpendicular to emission direction). The distribution of transverse velocities of emitted electrons may be quite

different if emission occurs through an individual ad-species. In addition, rates of electron emission have been seen to depend exponentially on the local field at the surface. A small asperity on a flat surface-leads to a local field enhancement at the protrusion.

Ethylene molecules occupy several metal atom diameters (several angstroms) space on the emitter surface. The molecular images observed, however, occupy much larger areas in the field electron micrographs. Apparent image sizes vary from 10-20Å, in accord with predictions based on transverse velocity considerations. Individual molecules are visible since practically all electron emission occurs through one point on the metal surface. In the m.i.'s seen in Figures 11 and 12, more than 90% of the total emission current of $\sim 10^{-8}$ amps appears to come from the molecular image.

In Figure 11, molecular images from ethylene adsorption at 4°K are shown. Multi-layer adsorption is not necessary as shown in 11-c where much less than a complete monolayer of ethylene is present, the clean field evaporated surface being visible. The molecular image itself is visible in 11-d which is a shorter exposure of the same emission pattern. A shadow deposit of ethylene on a field evaporated tungsten surface is shown in Figure 11-e with the clean tungsten surface visible at the bottom of the micrograph. In this case, the molecular image emanates from a physisorbed layer of

ethylene. Figures 11-a and 11-b show a clean field evaporated tungsten pattern and a similar tip with a monolayer of ethylene (heated to 200°K) for comparison purposes.

Figure 12 shows variation in the structure of a single ethylene m.i. Ordinarily, doublets are observed with ethylene. The doublet structure originally observed in Figure 12, however, interchanges with a variety of other patterns, some with three-fold and four-fold symmetry. Figure 12-h exhibits two dark spots in the original m.i. with a new m.i. apparent to the left of the original. Figures 12-i and 12-j show the doublet structure's symmetry axis rotated by 90°.

When the 2-butenes and butadiene were studied an even wider range of shapes was observed. In general, however, these interesting little image dots were avoided. For one thing, if many were present tip rupture often resulted. More importantly, F-N data could not be taken when m.i.'s were present.

There is no consensus at this time as to what the molecular images represent. One school of thought considers them to originate from polymeric strands which align with the electric field and act as wave guides for electron emission. We have seen (and literature references are also available to show-) that individual chemisorbed species can give rise to the bright emission centers.

Dosing with the field on does not, generally, result in uniform coverage over the entire tip cap. The reason is obvious from looking at Figure 1. The geometry of the tip-doser arrangement is such that, in the absence of the field, only the portion of the tip surface facing the doser can receive a hydrocarbon flux. Any hydrocarbon missing the tip assembly will be trapped out on the 4°K walls of the microscope. The presence of a viewing field can bend some hydrocarbon molecule trajectories into the rear side of the tip, but the side of the tip facing the doser will, however, receive a much heavier dose.

Migration experiments

A better way of achieving uniform coverages is to dose with the field off. In this case, only the portion of the tip cap within the solid angle from end of tip cap to the doser will receive any hydrocarbon. A multi-layer deposit is laid down; very careful heating of the tip to just the temperature needed to cause the physisorbed multi-layer to move distributes the second layer (and higher layers) over the entire tip surface. The process involves migration in the second layer over the chemisorbed layer until bare metal surface is encountered, where the physisorbed molecule is trapped by chemisorption. Migration over crystallographic regions containing different metal atom arrangements samples the atom densities suitable for chemisorption. The boundary

between clean metal surface and chemisorbed hydrocarbon should be anisotropic if a particular atom arrangement provides better trap sites than an alternative grouping.

Purity of samples

We have already seen how high purity hydrocarbons were loaded into the microscope tube. A reasonable limit for impurities would be the purity of the gas from the distributor, which was, for the three hydrocarbons used in FEEM studies, about 99.8%. Thus, 1 part in 1,000 is the maximum amount of impurity that can be delivered to the tip surface. Any molecules not striking the tip during the initial pass are removed from the gas phase. The only possibility for their re-evolution is through electron impact of the phosphor screen. Emission currents were never raised above 5×10^{-7} amps to guard against this occurrence. Contamination of the tip could be observed if emission currents were raised to 1×10^{-6} amps or higher.

Decomposition experiments

The major thrust of the field electron emission studies was to determine the thermal stability of selected hydrocarbons on clean tungsten surfaces. After dosing to obtain a monolayer coverage, the emitter was heated to 100°K with the field off for about 20 seconds, a period found sufficient to ensure that the surface reaction was complete. After cooling back to 4°K (several minutes), F-N data was taken.

This procedure was then repeated at higher temperatures, the interval spacing being chosen to cover the interesting regions found in earlier single point studies.

Photography

A photograph of the emission pattern was taken after each heating interval. Since the microscope screens were curved, a camera with a reasonable depth of field had to be employed. A 4x5 in. view camera with an f/4.5 objective was found adequate and gave 1:1 reproductions, if desired. Polaroid film, type 57 (ASA 3000) was used throughout the experiments. Its obvious advantage was the positive print which was produced. A disadvantage was poor sensitivity to wide ranges in image intensity which often necessitated several exposures before the desired details were captured. A further disadvantage was that only a positive was obtained, from which a copy negative had to be made for reproductive purposes.

Cost of a Field Emission Laboratory

Table 3 presents an itemized cost listing of equipment required for conducting field electron emission microscopy experiments.

Table 3. Field emission laboratory

Equipment	Cost
Calibrated High Voltage Power Supply	$ 800
Liquid Helium Cryostat	600
Liquid Helium (5-15 liters per experiment)	
Picoammeter	800
Kelvin Double Bridge Tip Temperature Controller	600
Diffusion Pumps	250
Ultra-high Vacuum Valves	1000
Ionization Gauge Controller	500
Ionization gauges (2)	100
2 Pen X-Y recorder	2000
Spot Welder	500
Glass cut-off wheel	100
Fore-pump	250
Vacuum Rack	100
Bake-out oven	200
4-5 View Camera	350
Oven (for annealing, screen application)	
Gas Supplies, torque wrenches, metals, phosphor, chemicals, switches, etc.	500
	$9000 +

Experimental Arrangement

Figure 13 shows a photograph of the experimental arrangement of equipment for field electron microscopy experiments including necessary graduate student operator. Not shown is the x-y recorder used for calibration purposes.

Results of FEEM Investigations

Work function versus temperature (Φ vs. T) plots for cis- and trans-2-butene and 1,3-butadiene show a somewhat discouraging lack of detail. The C-4 system was chosen for initial field emission experiments because many more surface reactions could be imagined than for the more extensively studied C-2 system. While the latter group of compounds undergo exchange, hydrogenation, cracking, dehydrogenation (and related decomposition), the C-4 system also undergoes double bond isomerization and cis-trans isomerization. In addition, the presence of at least three carbon atom means that allylically-bonded surface species are possible.

Decomposition of 2-butene

Figure 14 shows the results for cis- and trans-2-butene. Adsorption of either isomer at 4°K, followed by heating to 100°K for twenty seconds, produces a surface species which lowers the work function below the clean surface value. This is ascribed, as indicated in previous discussion, to associative adsorption of the olefin. Following the curve for cis-2-butene, heating to temperatures between 100 and

225°K results in a further decrease in work function. At ~225, a sharp break upwards occurs, with another break apparent at ~350°K. The clean surface work function value is reached at ~425°K. A small plateau is seen at ~500°K after which the work function values reach a maximum at 750°K. A small decrease in work function throughout the temperature interval 750-1,000°K completes the curve.

Single point data for trans-2-butene parallel the results just described for cis-2-butene.

The open-circle plot for a partially dosed tungsten surface (trans-2-butene) shows a gradual increase in Φ with increasing flash temperatures throughout the 150-600°K temperature range. This plot was included to show a danger inherent in interpreting Φ vs. T plots of non-uniformity dosed surfaces. In this experiment, only enough trans-2-butene was added to the tip to form about one-half a monolayer after spreading. From the previous discussion of work function measurements, it is apparent that the experimentally determined work function is representative only of those tip areas which are strongly emitting. For the partially covered tip, this means at lower flash temperatures the recorded work function is the average work function of the hydrocarbon covered portion of the tip. When the flash temperature is raised to about 400°K, the emission patterns show that the tip regions not covered with the initial dose become the

strongly emitting areas. Hence, between 400-500°K, the work function versus temperature plot switches from reflecting changes on the hydrocarbon covered tip portion, to the clean surface portion.

Field electron emission patterns from partially dosed tips, show no evidence of mobility of chemisorbed hydrocarbon species below the temperature where carbon migration is known to occur. This is illustrated in Figure 15 for trans-2-butene. The boundary formed from 4°K adsorption and heating to 100°K does not move until nearly the temperature required for carbon migration (~600°K in the bulk metal, lower temperatures on the tip surface).

The work function changes from Figure 14 are mirrored in the electron emission patterns recorded along with the work function data. These are shown in Figure 16 for cis- and trans-2-butene. Adsorption of the 2-butene's, followed by flashing to 100°K, results in a fairly uniform pattern with no marked emission anisotropy. Increasing the flash temperature to ~200°K gives rise to relatively more emission from the areas immediately surrounding the central (110) plane. Further temperature increases accentuate this pattern change until, at 350-400°K, a new pattern emerges with strongest emission oriented along the [100] direction. The new pattern persists throughout the temperature range 400-550°K. At about 600°K, only the areas surrounding the $\{100\}$ planes themselves

exhibit enhanced emission relative to the rest of the tip surface. Finally, at 600-750°K bright emission spots are seen in the central (110) region.

At least three surface reactions, occurring in the temperature range of catalytic interest, can be inferred from the work function plots and pattern changes. Something is occurring in the temperature ranges 100-200°K, 200-350°K and 350-500°K for both cis-2-butene and trans-2-butene. Field emission data, however, can tell us merely that a surface reaction has occurred. Some idea as to the nature of the surface species can be inferred from the work function values themselves but it will be convenient to delay discussion of the nature of the reactions until flash filament data has been presented. The latter technique monitors the species which occur in the gas phase as a function of temperature of the catalytic surface.

Migration of cis-2-butene

Migration studies in the FEEM can provide data concerning surface heterogeneity effects. A multi-layer shadow deposit is first made at a temperature below that at which physisorbed material is mobile. Careful heating to just the temperature required for mobility of the physisorbed layer causes second layer migration as described previously. The boundary between clean metal and metal covered with chemisorbed olefin is readily observed since chemisorption results in a work function

decrease. This causes a bright boundary to appear due to the lower work function of the boundary areas relative to their surroundings. The movement of the boundary reflects the density of sites available for chemisorption. Boundary movement will be most rapid in crystallographic directions containing low densities of sites suitable for chemisorption.

Gardner was able to show that acetylene migration was slowest over tip regions containing 3.16Å spacings in high densities. Ethylene migration, on the other hand, was retarded on planes with 4.5Å spacings in large numbers (36). The results for the C-4 hydrocarbons in this study were not nearly so clear cut. Figure 17 shows migration micrographs for cis-2-butene. The initial deposit is covering the upper half of the micrographs, the direction of migration being generally $[1\bar{1}0]$. Some retardation of the boundary may possibly be inferred at the (211) plane from the patterns in 17-e,f,g, in agreement with Gardner's results. This suggests that cis-2-butene, like ethylene, finds a high density of sites available for chemisorption on the $\{211\}$ planes.

Atom spacings for some of the more prominent low index planes of tungsten are shown in Figure 18.

The direction of migration in this series of experiments was $[1\bar{1}0]$ which is parallel to the atom rows of the [211] plane. Gardner's [001] migration direction for ethylene was, on the other hand, across atom rows. Ehrlich, in FIM

migration studies of tungsten self-diffusion, was able to show that ad-atom migration along atom rows of the [211] was appreciably easier than across atom rows (30). The same sort of phenomenon may be occurring for olefin migration across tungsten [211] planes. Unfortunately, the data supporting this conclusion were taken for ethylene migration on one field emitter tip, and cis-2-butene migration on a different tip. Further migration studies with a single olefin are needed before firm conclusions can be reached.

In a second migration experiment with cis-2-butene, with migration direction the same as previously described, the boundary was observed to move very rapidly along the approaches to the central (110), and also on the stepped structure going away from the central plane. This also would be predicted on the basis of Gardner's observations that the closely packed (110) would not have a high density of sites suitable for olefin adsorption.

Decomposition of 1,3-butadiene

Decomposition of 1,3-butadiene on clean tungsten surfaces differed in several respects from that of the 2-butenes. The work function versus temperature plot is shown in Figure 19. Dosing at 4°K, and heating for twenty seconds at 100°K, resulted in a work function value about 0.35 eV below the clean tungsten value. Heating the adsorbed layer to temperatures between 100-150°K gave a work function increase.

Subsequent heating periods at temperatures between 150-200°K gave a work function decrease. The small maximum in the Φ vs. T plot between 100-200°K was reproducible, both as to the work function maximum at ~150°K and also with respect to the absolute value of the work function at any point in the temperature interval.

Heating intervals at 200-400°K gave a steady increase in Φ which fell off at about 400°K. Further heating intervals between 400°K and 600°K gave a slower rate of increase in work function with increasing temperature. The electron emission patterns for selected temperatures from 100-900°K are shown in Figure 20. The work function maximum at 150°K is not reflected in the emission patterns which remain fairly uniform in overall intensity between 100-200°K. The patterns obtained for temperatures between 200-750°K are the equivalents of those for the 2-butenes and also nearly identical to those obtained by Gardner for acetylene on tungsten (36).

FEEM evidence implies a surface reaction for 1,3-butadiene between 100-200°K, and a second reaction occurring over a broad temperature interval beginning at 200°K.

FIELD ION MICROSCOPY

Introduction

The field electron emission microscope, (FEEM), employing electrons as the imaging species, cannot depict emitter surfaces in atomic resolution. This is due to a broadening of the impact area for each emitting center, owing to the emitted electrons substantial transverse velocity component. Coupled with the fact that electrons possess a wave nature, and hence undergo diffraction, this means that objects separated by distances less than 20Å will not be imaged separately.

The obvious solution, in retrospect, to this seeming impasse is to use positive ions as the imaging species rather than electrons. The larger mass of the ion, with accompanying decrease in de Broglie wave length, decreases diffraction effects. In addition, the ion formed initially above the metal surface is essentially at rest. As a result, its transverse velocity component can be reduced by lowering the temperature of the imaging gas. Mueller, in 1941, reversed the polarity of a field emitter and discovered that in high positive fields of 70-130 MV/cm, electropositive adsorbates such as barium could be stripped from metal surfaces as ions; their presence was detected at the screen phosphor as an ion current (80). The new effect was termed <u>field desorption</u>. The desorption of barium monolayers, however, yielded single ion pulses much too small for visual observation.

This difficulty was surmounted, at least in theory, by Mueller (1951), who conceived the idea of continuously supplying the imaging medium by filling the emission tube with a gas which would ionize in the high field near the metal tip (89). After ionization, the ions are nearly at rest in the presence of the high electric field. As a result, they are accelerated along the electric lines of force and impact the phosphor screen.

Where the field electron emission microscope presents a radial projection of the relative rates of electron emission from a metal tip, ion microscopy displays a radial projection of the relative imaging gas ionization rates above different surface atoms. In Figure 21, a field ion image of a field evaporated tungsten tip is compared with a field electron image for a tip of comparable size. Each dot in 21-a locates the position of an individual tungsten surface atom while the electron image shows only the location of certain planes with highest work function.*

---

*The most comprehensive review article on the subject of field ion microscopy is to be found in Advances in Electronics and Electron Physics, Volume 13, page 83 (1960). This work by E. W. Mueller, covers field ion literature prior to 1960. Mueller has updated the 1960 work to cover the period 1960-1966 in Annual Reviews of Physical Chemistry, Vol. 18, p. 35 (1967). The same writer has written a comprehensive history of field emission (field electron and field ion) (79).

Field Ionization

The ionization of the imaging gas by high electrical fields of 2-5 V/Å occurs by tunneling of electrons from the gas phase atoms, the phenomenon being referred to as <u>field ionization</u>.

The ion current, i, can be formulated as:

$$i = Z\,P\,e \tag{14}$$

where: Z = number of gas atoms arriving at the tip per second,

P = total probability that one of them be ionized, and

e = unit of electrical charge.

Gas kinetic theory considerations would predict Z to have the form, $P/\sqrt{2\pi mkT}$ per cm^2, whereas, in practice the number of gas atoms supplied to the tip is some 10-100 times larger (84). The supply increment is due to the generation of an induced dipole moment of αF in each gas atom of polarizability α, and its subsequent attraction in the inhomogeneous field at the tip. Brandon has discussed the subject in some detail and reports that the supply function for spherical emitters of radius r goes as (10):

$$Z \cong (4\pi r^2 P/\sqrt{2\pi mkT})\ (\tfrac{1}{2}\pi\alpha F^2/kT)^{1/2}\ . \tag{15}$$

<u>Accommodation of gas atoms to tip temperature</u>

As intimated above, the imaging gas atom picks up approximately 0.1 eV in polarization energy ($E_p = \frac{1}{2}\alpha F^2$).

When translated into thermal energy, this means that an impacting gas atom behaves as if it originated from a reservoir at 1100°K. Neutral gas atoms will thus impact the tip and rebound, giving up an amount of energy γE_o, (where γ is the accommodation coefficient for the gas-metal collision process). Accommodation coefficients for the noble gases on clean tungsten surfaces are given in Table 4 from room temperature to 4°K (132).

Table 4. Accommodation coefficients for noble gases on clean tungsten surfaces

T(gas) (°K)	He	Ne	Ar	Kr	Xe
303	.0166	.045	.271	.46	.77
243	.0155	.0425	.30	.51	.81
193	.0148	.042	.34	.57	.85
153	.0142	.044	.39	.63	.89
113	.0137	.049	.47	.74	.93
90	.0133	.054	.54	.86	.96
77	.0131	.058	.60	.94	-
40[a]	.0082	-	-	-	-
35[a]	-	.09	-	-	-
20[a]	.012	.14	-	-	-
4[a]	.019	-	-	-	-

[a] Minimum values.

Hopping height

Once an amount of energy equal to $3/2kT_{gas}$ has been transferred to the metal, the gas atom becomes trapped in the tip region. There is no adsorption, at least for He-W, between impacts (93). The helium atom thus returns to the surface again and again in a hopping motion of gradually decreasing amplitude. From Table 4 (for He) it can be seen that several hundred collisions may be required before equilibration to tip temperatures is achieved. The amplitude of the hopping motion, or hopping height, decreases with each equilibration, the average hopping height, $\bar{h}$, being (70):

$$\bar{h} = 3kTr/4\alpha F^2. \qquad (16)$$

For the case of helium, thermally equilibrated with a tip at 21°K, and for $\alpha = 2\times10^{-25}$ cm^3, F = 4.5V/Å, and tip radius r = 1,000Å,

$$\bar{h} = 4.8\text{Å}.$$

Once equilibrated sufficiently so that the hopping height is ~5Å, there are several possibilities for any given gas atom:

1. The sequence of hops may bring the atom near the shank of the tip where the field is diminished in strength, in which case the gas atom can escape by evaporation.

2. The hopping atom may move through a region where the field is strong enough to cause field ionization.*

*The process of field ionization has been extensively treated by Gomer (41), and by Mueller (70), among others.

Tunnel mechanism of field ionization

Field ionization in free space In the presence of a high electric field, the potential barrier behind which the valence electron of the gas atom is trapped is lowered on the anode side, relative to the field free case. If the barrier is thinned sufficiently, electrons can tunnel through. The quantum mechanical problem for ionization in free space has been solved explicitly for hydrogen atoms (54,117), and hydrogen molecule ions (44). For hydrogen atoms the rate constant for field ionization is:

$$k = 0.944 \times 10^{15} \, F/I^{1/2} \exp. \, (-0.68 \, I^{3/2}/F) \, sec^{-1}. \qquad (17)$$

The probability of ionization varies essentially as the exponential term while the pre-exponential contains the number of collisions a valence electron makes with the potential barrier.

The result for field electron emission, the Fowler-Nordheim equation, can be written for comparative purposes as:

$$i = 1.54 \times 10^{10} \, \frac{A \, F^2 K}{\Phi} \exp. \, (-0.68 \, \Phi^{3/2} K'/F). \qquad (18)$$

The form of Equation 17 and 18 is the same, with ionization potentials in field ionization replacing work functions in field electron emission. In fact, field ionization has been referred to as field emission in reverse (41).

Field ionization at a metal surface In the presence of metal surfaces, the process is more complex. Even in the

absence of an applied field, the barrier toward the metal is reduced due to overlapping of the Coulomb potential of the ion core with an image potential term. The latter results when the emerging electron of the helium atom induces in the metal a charge, equal in magnitude to its own, but opposite in sign. This is shown in Figure 22. The dotted line represents the superposition of image and Coulomb potentials. The solid line shows that the effect of the applied field is to lower the height and thin the width of the barrier still further.

The probability for field ionization depends critically on the distance of the gas atom from the metal surface. Figure 22 displays the most favorable or "optimum" distance, x_c. An emerging electron from the gas atom has just the energy required to enter an empty metal energy level at the Fermi level. If the gas atom were further away from the surface when ionization occurred, it would have to penetrate a thicker barrier. Movement closer to the metal surface than x_c encounters a thinner potential barrier; there are, however, no vacant metal energy levels below the Fermi level to accept electrons.

Energetics of field ionization

The energetics of field ionization are more clearly displayed in Figure 23. To create an ion in the absence of an electric field requires an energy input $I - \Phi$. The presence of a field, however, lowers the energy of the ionic state by

$\frac{1}{2}\alpha F_+^2 + eF\,x + e^2/4x$, while the atomic state is depressed by only $\frac{1}{2}\alpha_o F^2$. At the critical distance, an iso-energetic conversion from atom to ion is possible when:

$$0 = I - \Phi + \frac{1}{2}F_+^2(\alpha_o - \alpha_+) + eFx_c - e^2/4x_c \quad . \qquad (19)$$

Using F = 4.5V/Å and solving for the critical distance yields (25):

$x_4 \cong 4.3$Å.

Ionization occurs, not <u>on</u> the metal surface, but, some 4-1/2Å <u>above</u> the metal surface!

As noted in Figure 23, the presence of the field shifts the image plane because field penetration of the metal surface depletes the supply of conduction electrons at the metal. The critical distance is thus a weak function of the applied field.

Retarding potential measurements provide direct experimental evidence concerning the location of the ionization event. If ions were formed at the surface of an emitter, they would be accelerated through the full potential difference between tip and screen. Ionized at any intermediate distance, the ions must display less energy. At best image voltages (BIV) for helium, the disc-shaped ionization zones above each imaged surface atom are only several tenths of an angstrom deep (136). One-half of the ionizations take place within a depth of only 0.17Å, while 95% take place within a depth of 0.6Å.

The significance of ionization occurring several metal atoms diameters above the tip surface, as well as other effects the field has on the formation of the ion image, will be taken up in the discussion of the interpretation of ion images.

Experimental studies on ion current versus applied voltage

The ion current has been seen to depend critically (exponentially) on the applied field. Plots of experimentally determined ion currents (log i) versus V are found to yield two linear portions (128, 135). At lower fields (first linear portion), the probability for ionization increases rapidly with increasing field. The supply of gas atoms to the tip likewise increases while the average hopping height decreases. At a certain applied voltage, the field above some atoms on the emitter surface attains the strength needed for ionization (termed the threshold field, F_c). Further increases in voltage result in a second linear portion in which the ion current increases at a slower rate with increasing voltage. As the applied voltage is increased still more, the field strength at certain points on the emitter surface reaches a value high enough to rip metal atoms from the tip surface (termed the evaporation field, F_e).

Stable field ion images are possibly only between F_c and F_e (the working range in applied voltage). For some metals F_e is greater than F_c using helium as the imaging gas. For example, tungsten falls in this class, in which case stable

helium ion images of tungsten are possible. For other metals (such as gold) field evaporation fields are reached before the critical field strength using helium as the imaging gas. In this case, stable helium ion images are not possible. Even for tungsten, the working range does not extend from F_c to F_e due to the fact that the imaging gas ionizes too far away from the metal surface at fields approaching F_e to yield a resolvable ion image.

Studies of the variation in ion current with applied voltage are critical to the development of an adequate theory for field ionization above metal surfaces. Such a general theory is, unfortunately, not available at this date. The ionization process is highly complex (135). Thus, in one study (128), the second linear portion of a log i (amps) vs. F(V/Å) yielded a fairly reproducible slope of ~3 for various metals. The dependence of ion current on tip temperature went as $1/T^2$. A later study, using isothermal conditions (imaging gas and tip temperature the same) and employing a photometric method for determining i, found that in the working range log i - F slopes varied between 3.2 and 5.2 depending on the cone angle of the emitter. A temperature dependence of 1/T was observed.

A consideration of the factors likely to affect a temperature dependence study illustrates the complexity of the ionization process. Image intensities generally decrease

with increasing temperatures. This reflects in part a difference in ionization probability with increasing temperature. Thus, a temperature increase should increase the average hopping height. The accommodation process is a weak function of temperature as shown in Table 4. In addition, accommodation of impacting gas atoms depends markedly on the presence of an adsorption layer on the shank of the tip.

Tip shapes have already been noted to have an effect on ionization rates of image gas (cone angle variations). In a recent study, tip radii were systematically changed while the maximum field for non-blurred image was held constant, and the tip temperature required for good resolution was observed. Three-hundred angstrom tip radii at 100°K yielded non-blurred images while 700Å tips required cooling to ~20°K in order to obtain a non-blurred, well resolved image (143).

Ion Images, Interpretation

Geometrical considerations

Figure 24 shows a hemispherical cut through a face-centered-cubic metal lattice. Lattic atoms outside the hemispherical cut have been discarded. Field ion micrographs present radial projections of local field distributions about 4.5Å above the tip surface. Most theories of field ionization begin by assuming that atomic protrusions on the emitter surface give rise to high local fields (13). This is illustrated in Figure 24 by drawing equipotential surfaces at various

distances from the metal surface, by constructing intersecting circles centered at the middle of surface atoms. This simple approach clearly shows that at the tip surface, the field profile is quite ragged; at a distance of 4-5Å above the surface, however, considerable smoothing has occurred. Since the probability for ionization goes as exp. $(-1/V^n)$, where n = 1 for free space field ionization of hydrogen atoms and 3-5 for experimentally encountered conditions with helium, small differences in field intensities, however, can be expected to give rise to large differences in ionization probability. Using the exponential dependence predicted by Equation 17 for helium at BIV, a 1% difference in field leads to ~ a 30% difference in ionization probability.

The basic idea behind formation of the ion image are thus understandable in simple terms. It is easily seen, by reference to Figure 24, that only the most exposed surface atoms, i.e., those at the edges of net planes and those inside loosely packed planes, will yield image spots at the phosphor screen. In practice, only about one in five of the outermost tip atoms are found to produce a resolvable image spot (22).

Computer simulation of ion images, employing basically a cut through a metal lattice, have duplicated almost exactly the atom arrangements observed in ion images (15,66,67,68, 101,107,108,112,121,122,123).

Effect of charge distribution at metal surfaces

Ion images display more subtle details than would be expected from the simple geometrical model just outlined. The geometrical model is limited chiefly because it assumes surface metal atoms can be treated as hard spherical balls. A refined approach to estimating relative fields above different atom locations takes into account charge distribution at the metal surface. At a plane metal surface, the electron cloud does not terminate abruptly, but spills over, resulting in an electrical double layer with negative side out (13,138). On stepped surfaces, a second kind of double layer occurs, with positive end out, the result of conduction electrons leaving exposed corners and filling in the step depressions.

The "smoothing" effect of the second process will proceed to a different degree on different crystallographic planes. This is shown in Figures 25-a and 25-b. The electron gas at the metal surface will be held most tightly at ion core positions. Between ion cores, the spill over phenomenon will be most pronounced on planes with lowest surface ion core densities. Qualitative predictions, based on this sort of model, can be used to explain work function variations on different planes (13). The original negative-out surface dipole layer predicted for a plane metal surface is diminished on planes with different atom arrangements by the degree of charge transfer into the void spaces between ion cores. The resulting positive-out dipole layer from this type of charge

transfer will be greatest on more loosely packed planes. Hence, work functions will be highest on smooth planes where less of a positive-out dipole layer can be formed, and lower on rougher surfaces.

In field electron emission, the applied field facilitates electron removal from the tip. When a high positive voltage is applied to an emitter, electrons will instead be drawn into the metal as shown in Figure 25-c, leaving the positive atom centers in even more exposed positions. The effect of the high positive field, then, is to make exposed surface atoms even more positive. The charge density induced in a surface atom, σ_i, by a field of magnitude F can be formulated as (86):

$$\sigma = F/4\pi. \qquad (20)$$

Field penetration of the metal surface thus leads to an enhancement of the local fields above exposed tip atoms. In addition, field profiles are "roughened" as a result of rearrangement of surface charge.

Effect of spatially directed surface metal orbitals

So far, the charge distribution at a metal surface has been considered in terms of a sheet of charge. A further refinement attributes directional bonding orbitals to surface metal atoms (much the same as can be done for bulk metal atoms) (53). With this refinement, not only the geometrical arrangement of tip atoms must be considered but also:

1. the spatial arrangement of surface metal orbitals, and
2. the degree of occupancy of the surface metal orbitals.

Qualitatively, the mechanism of image formation is readily understood. Only those surface atoms will be imaged, above which:

1. the field is high enough,
2. gas atoms are present in sufficient numbers, and
3. the field profile is rough enough to produce sufficient contrast for the individual image spot to be resolved.

Ball models of emitter surfaces

In Figure 26 four photographs of a quarter-section of a [100]-oriented face-centered-cubic emitter have been arranged to form a pattern for a hemispherical tip. The ball model was constructed by making a hemispherical cut through a fcc lattice in the manner previously described. Prominent planes observed in ion images of [100]-oriented fcc emitters, e.g. the {110}, {210}, {311} and central {100}, are shown with black balls to emphasize the perfection of the atomic planes developed in field evaporated tips. Green balls (which photograph as grey) were used elsewhere to indicate protruding atoms likely to be imaged while the {531} planes are shown in yellow (which show up a very light grey).* Ball models of [110]-oriented

*J. F. Nicholas's, "An Atlas of Models of Crystal Structures", (103) is an invaluable aid in such esoteric pursuits as construction of tip models. Photographs of ball models of b.c.c., f.c.c., h.c.p., NaCl and diamond planes, with angles and distances indicated also are useful as an interpretative aid in catalytic studies.

b.c.c. emitters have been published to aid in understanding field ion patterns (24,41,70). The latter reference (24) contains a rather complete [110]-oriented b.c.c. orthographic projection which is also compared with observed tungsten helium ion micrographs.

Field Evaporation

Introduction

In field electron microscopy, field emitters were cleaned and shaped thermally. This method, however, is not practical in field ion microscopy as it leads to excessive blunting, which cannot be tolerated in the FIM due to the excessively high voltages that would be required. For a given tip, the voltage required to obtain a helium ion image is 10-12 times that required for electron emission (70). The surfaces of thermally shaped emitters are disordered on an atomic scale due to a freezing in of the thermal disordering process which occurs during cleaning flashes. The imaged surface atoms lie at the edges of low index planes and on top of perfectly ordered tip material which can be reached by field evaporating away several layers of the disordered material. In the case of tungsten this requires raising the voltage about 10% higher than helium ion best image voltage. Surface atoms are removed in the high fields of ~5 V/Å leading to an end form with surface atoms again lying on flat planes. The tip shaping process, mentioned previously, is field evaporation (82).

Image force theory for field evaporation

The original explanation of field evaporation assumed that f.e. involved thermal evaporation of an ion of charge n over a potential barrier, Q_n (75). The image force theory for field evaporation can be formulated by first writing down the activation energy, Q_o, required for evaporation of metal atoms as M^{n+} in the absence of an applied field.

$$Q_o = \Delta H_s + \sum_{m=1}^{n} I_m - n\Phi \qquad (21)$$

where ΔH_s = sublimation energy
I_m = m^{th} ionization potential } of metal
Φ = work function.

Equation 21 summarizes the energetics of a thermionic cycle which removes a surface atom to a point an infinite distance from the surface; at that point the metal atom is ionized, the electron being returned to the surface.

In the presence of an applied field, the energy requirement is lowered due to the induction of an image force by the field.

$$Q_n = Q_o - \sqrt{n^3 e^3 F.} \qquad (22)$$

The time constant, τ, for the process can be written as (70):

$$\tau = \tau_o \exp. (Q_n/kT) \qquad (23)$$

where $\tau_o = 1/\upsilon$ and υ is the vibration frequency of the bound particle.

Solving Equation 22 for the evaporation field, F_n, and using Equations 21 and 23 yields:

$$F_n = \frac{[\Delta H_s + \sum_{m=1}^{n} I_m - n\Phi - kT \ln (\tau/\tau_o)]^2}{0.144\ n^3} \quad (MV/cm) \qquad (24)$$

For field evaporation temperatures less than 100°K, the temperature dependent term can be ignored.

Table 5 presents calculated values for the evaporation field for singly and doubly charged ions using Equation 24. This crude model predicts that for the metals listed in Table 5, all but copper should evaporate as M^{2+}. The few experimental studies so far conducted are generally in agreement with this prediction. Thus, a Re-Mo alloy field evaporated as Mo^{2+}, Re^{2+} while tungsten tip materials yielded W^{2+} (96). At temperatures of 21-300°K, iron, zinc and cadmium yielded mostly M^{2+} ions (133). Higher temperatures favor formation of single-charged ions. At 700°K, iron gave largely Fe^{2+} (133). For platinum at 1450°K, Pt^{+} was the predominant species (141). The temperature dependence of the ratio M^{+}/M^{2+} was found to be quite striking for copper and beryllium (133). Beryllium forms mostly Be^{2+} at temperatures below 150°K, while Be^{+} became the predominant species at higher temperatures. Cu^{+} is formed in equal amounts with Cu^{2+} at 75°K, but soon becomes the major species with higher evaporation temperatures.

Table 5. Evaporation field, Fe, at absolute zero for singly (F_+), and doubly (F_{++}) charged ions[a]

Metal	Heat Sublimation ΔH_s (eV) (14,25)	Work Function ϕ(eV) (14, 70)	I_1 eV (69)	I_2 eV (14, 69)	F_+ (V/Å)	F_{++} (V/Å)
W	8.67	4.35	7.98	17.7	11.40	5.71
Ta	8.10	4.20	7.7	16.2	11.03	4.83
Re	8.10 (7.97) (55)	5.1	7.87	16.6	8.25	4.34
Ir	6.50	5.0	9.2	-	7.95	-
Nb	6.87	4.01	6.88	14.32	6.59	4.22
Mo	6.82	4.30	7.13	15.72	7.88	4.22
Pt	5.84	5.32	8.96	18.56	7.63	4.88
Rh	5.77 (5.68)	4.8	7.46	15.92	6.18	3.67
Au	3.68	4.82	9.22	20.5	5.72	5.31
Fe	4.30	4.17	7.90	16.8	5.66	3.96
Co	4.40	4.40	7.86	17.05	5.45	4.24
Pd	4.08 (3.87)	4.99	8.33	19.42	4.92	4.53
Ni	4.38	5.01	7.63	18.15	4.44	4.07
Cu	3.52	4.55	7.72	20.29	4.22	4.72

[a]A constant value for the polarization contribution to the binding energy was taken to be 1. eV (84).

Refinements to the image force model Refinements to the simple ionic evaporation model have been made including references to polarization effects, field penetration of the metal surface, short range repulsive potentials in addition to the attractive image potential, different forms for the attractive potential, variations in surface bonding, and the

finite width of the conduction band of the evaporating atom. A comprehensive review article on field evaporation including calculated values for the evaporation fields of singly, doubly and triply charged ions, which takes into account some of the effects mentioned above, is available (14). As in the case of a more recent look at the problem (133), the qualitative results expressed in Table 5 are found to hold.

The latter treatment, however, also considered field evaporation as a strictly quantum mechanical problem (133). The tunneling mechanism for field evaporation was found to be as probable as, if not more likely than, the thermal mechanism.

End form of field evaporated tips

Each of the theories, however, concludes that an emitter shape resulting from field evaporation will be determined by requiring constant fields over a large portion of the emitter surface. Any asperity on the surface which causes a higher local field will be removed (85). Local fields will vary in different crystallographic regions due to variations in work function and surface polarizability. Thus, the end forms developed by field evaporation can be expected to be quite distinctive of the metal under study. In addition to the numerous observations on tungsten, platinum and iridium, the end forms of iron (93), tantalum (91), molybdenum (78), ruthenium (63), cobalt (105), and rhenium (115) have been analyzed in some detail.

Stability of various metals under field evarporation fields

Fields on the order of 4-6 V/Å (Table 5) are required to shape tips for the ion microscope. At a field of 4.8 V/Å, the mechanical stress, δ, on a tip specimen is $\sim 10^{11}$ dynes/cm^2 or stated, differently, 1 ton/mm^2. ($\delta = F^2/8\pi$). This enormous stress is some eighty times the technical tensile strength of platinum (115). Of critical importance, then, when considering a metal for field ion studies, is whether or not the tip material can withstand the rigorous tip shaping conditions. Only W, Ta, Ir, Pt, Rh, Ru and Au have been found capable of withstanding the field stress at their respective evaporation fields and develop perfect end forms (64, 85). Re, Mo, Nb, V, Pd, Fe, Ni and Co yield, but only in specific crystallographic areas, other areas of the tip remaining perfect (105).

Hydrogen field induced reaction

The application of the hydrogen field induced reaction, as a means of lowering evaporation field requirements, has enabled tip specimens of the non-refractory metals to be routinely used (1, 93). Small amounts of hydrogen or deuterium lower the evaporation field enough so that areas of a niobium tip, which ordinarily would have yielded, were developed in near perfect form. This phenomenon occurs with all metals, the extent of the interaction varying markedly. Reductions in evaporation field requirements for tantalum and

molybdenum were observed as 15% and 8% respectively. With the non-refractory metals, the effect is much more pronounced. Iron (hence, steel emitters), nickel and cobalt all yield disordered end forms when field evaporated in vacuum. Neon images of emitters shaped in the presence of small amounts of hydrogen show much more perfect end forms (92, 93, 105).

The promotion effect of hydrogen on field evaporation is closely related to the corrosive effects on emitters observed previously for water and nitrogen (53, 70, 73, 87). I had occasion to observe the etching effects that contaminant water molecules have on helium ion images of tungsten at liquid nitrogen temperature. (This was before I became aware of the nature of field induced reactions.) My original microscope design contained a grease joint to join the microscope flask to the vacuum system and residual vacuums were rarely better than 1×10^{-6} torr. When observing ion images, which initially were fully developed, I often observed marked instability of the image starting at the periphery of the image. The initially well developed image deteriorated in size until all that remained was the central (110) area. The voltage required to obtain images of the developed areas steadily decreased, and if the process went unchecked tip rupture resulted.

The bothersome "tip sharpening" reaction (as indicated by the lowered voltage required for image formation) is due to adsorption of contaminant molecules such as water and

nitrogen on the low field portion of the emitter cap. At 78°K the contaminant species can migrate onto the higher field portions of the emitter, where the field is high enough to field desorb both the contaminant and underlying metal atoms. The process is reduced in intensity by cooling the emitter to temperatures where migration from the shank cannot occur (e.g., 20°K or lower) and in baked systems the "etching" phenomenon was rarely observed.

The effect of the applied field has already been noted as reducing electron density in metal atom bonding orbitals (with reference to increasing the relative positive charge of a metal surface atom (90)). Presumably, a chemisorbed adspecies in effect does the same thing. Metal-metal bonds are weakened in this process (45). The surface metal atom, or the adsorbate-m etal complex itself, can then be removed at a reduced field relative to vacuum field evaporation requirements.

Imaging Gases

Resolution and image intensities are far better with helium than with any other imaging gas (60), and most FIM studies are made with helium. Table 6 lists pertinent data for gases suitable for ion microscopy. The field required for helium ion imaging (for BIV) is given as 4.5V/Å. From this, it can be seen that all metals cannot be imaged with helium. For example, although gold developes perfect field

Table 6. Data for imaging gases

Gas	Ionization Potential (eV)	Best Image Field (93) (V/Å)	Operation Temperature (°K)	Potential Resolution (500Å tip)	Polarizability (25,70, 104) ($Å^3$)	Covalent Radius	Phosphor Efficiency ('43) ($ZnSiO_4$)
He	24.6	4.50	4+	1.2	0.21	0.93	6%
Ne	21.6	3.70	21	1.3	0.392	1.31	0.9%
Ar	15.7	2.30	77	3.3	1.65	1.74	
H_2	15.6	2.28	21	1.7	0.8	0.37	
N_2	15.5	2.26	77	3.3		0.75	
Kr	14.0	1.94	77	3.6	2.50	1.89	
O_2	14.0	1.94	77	3.9		0.73	
Xe	12.1	1.56	77	4.0	4.10	2.09	0.65%

evaporated end forms in vacuum, gold emitters cannot be imaged in helium (evaporation sets in before best imaging fields are reached). Only metals which field evaporate at fields in excess of 4.5 V/Å can yield stable helium images. All metals in Table 5 can be imaged at, or below, their evaporation fields with neon (84). Neon images, however, are many times less bright than their helium counterparts. (At BIV for tungsten at 21°K, a neon image required thirty times as long an exposure as a helium image (13,104).) This stems from a number of factors, a six-fold loss in phosphor efficiency, a reduced imaging voltage, and the lower neon pressure that must be employed.

In general, it has been found that image brightness goes as the first power of the pressure, but the cube (or higher power) of the voltage (16,115,118,142). Helium pressures up to

$$\text{Int.} \sim P\ V^3 \qquad (25)$$

5×10^{-3} torr (5 microns) can be utilized without appreciable loss in image quality (10,100). (In my studies, helium pressures of 1-2 microns were generally used.) The actual pressure that can be used will, of course, depend on the tip-to-screen distance in the microscope employed. The upper limit in pressure is reached when the mean free path of helium ions is on the order of the tip-to-screen distance (mean free paths $\sim 1/(2r)^2$). A quoted pressure for neon is 1.5 microns (16).

The other commonly used imaging gas, hydrogen, suffers from several disadvantages. Comparing best image fields for

hydrogen with nitrogen or oxygen (likely contaminants in vacuum systems), it is apparent that bakeable systems capable of ultra-high vacuum are needed when using hydrogen as the imaging gas. With helium, or neon, on the other hand, any contaminant gases present in the microscope cannot reach the tip cap from the gas phase. With their lower ionization potentials, the contaminant species will be "space" ionized long before they get near the tip surface and contribute only a diffuse background to the ion pattern.

The lower ionization potential for hydrogen means a correspondingly less bright image. Hydrogen pressures of only 0.5 microns are quoted as optimum (70). Thirdly, the lower melting point metals cannot, in general, be imaged satisfactorily in hydrogen due to the field induced evaporation process mentioned previously (70). Finally, adsorption studies are precluded using hydrogen as the imaging gas if work function measurements are to be taken.

Only one instance of the use of argon as an imaging gas has been reported; it was used to image a germanium emitter (1). The reported image intensity at 77°K was 1/10 that for a hydrogen image.

A novel "imaging gas" recently employed is lithium (38). A pulse desorption microscope was designed, which at 500°K could be operated to give a visible image. The idea is similar to Mueller's field desorption of barium monolayers.

In this case repetitive pulses are used to obtain higher image intensities.

Hydrogen promoted helium images

A recent discovery has provided hope for imaging the common transition metals with helium (104). The initial experiment involved additions of small amounts of neon to the helium imaging gas. Image contrast was improved while the BIV was lowered slightly. The effect was attributed to improved accommodation of the helium through weakly adsorbed neon atoms. Hydrogen (or deuterium) provides a much better match in collision masses and when 0.1-1% hydrogen was added to the imaging gas, a new sharp image at only 75% of the previous BIV for helium was reported (93). The new image was found to be entirely due to helium.

The original explanation for the phenomenon of hydrogen promotion of field ionization has been scrapped; the effect is now believed to involve rearrangement of surface charge through chemisorption of the hydrogen (86). Hydrogen atoms, sitting below the electronic surface, bond to protruding metal atoms to give a "hydride-like" linkage. The process results in a greater positive charge on the metal atom to produce a local field enhancement.

The hydrogen promotion effect occurs only in the narrow voltage range of 65-67% of the initial helium BIV. The effect is observable with hydrogen partial pressures of 10^{-6}

torr but is most pronounced at 10^{-5} to $5x10^{-4}$ torr. Hydrogen promoted images are reported to be 1.2-1.8 times brighter than the original helium image, image details being the same. The image spots, themselves, are smaller in the promoted helium image. 78°K images display the promotion effect, although 21°K tip temperatures yield a maximum effect. No further improvement was observed at 12°K.

Xenon also lowers the BIV for helium ion images and also promotes hydrogen ion images.* The promoted image quality of the Xe/He image (66% He BIV) was reported to be excellent, while the xenon promoted hydrogen image (at 69% hydrogen BIV) was of poorer quality. In both cases the image intensity of the promoted images exceeded those obtained with pure imaging gases.

Visibility of adatoms The mechanism for hydrogen promotion of field ionization has relevance for alloy and adsorption studies. The more electronegative moiety in a surface adsorbate-adsorbent complex will withdraw electrons from the more electropositive species. For example, in an ordered platinum-cobalt alloy studied, two types of planes were observed. In one, the first layer consists entirely of cobalt, the next layer entirely of platinum. In the

---

* Swanson, L. W., Reed, D. E., and Bell, A.E., Lowering of the BIV for the He and H_2 ion microscope by the addition of xenon. Unpublished results reported at the 14th Field Emission Symposium, Gaithersburg, Md., June, 1967.

second type of plane, both elements are present; but only one of the atomic species is imaged (134). Cobalt, being more electronegative, is believed to be invisible, while only platinum is imaged on the mixed planes.

The pertinence of the present discussion to adsorption studies is that all adsorbates studied to date in the FIM are more electronegative than the metal substrates on which they were adsorbed. Carbon monoxide, nitrogen and oxygen might well be expected to act in a fashion similar to hydrogen (5,27,39,45,56,73,94,98,100). Generally, image spots attributable to adsorbed species are larger and brighter than metal atom image dots. Furthermore, only individual spots are generally detected even in adsorption studies where molecules are known to be involved. (A large central dot flanked by two dimmer satellites has been observed for the CO/W adsorption system (27)). A distance of ~13Å separated the two satellite image points. The area of the image dot clearly is not dependent on the size of the adsorbed species; this suggested to Mueller that image point size for adsorbates depends on the region of the metal surface which is depleted of conduction electrons (85).

It is difficult to see how an electronegative species would be imaged by itself. In fact, there is some agreement that oxygen ad-atoms are invisible (83). The question remains, though, as to exactly what the bright image dots do represent.

Sachtler *et al.* believe that carbon monoxide adsorption on tungsten leads to rearrangement of the metal substrate (45). The corrosive effect leads to substantial rearrangement of the metal-adsorbate complex for 300°K adsorption. At 78°K little rearrangement occurs. Tungsten atoms, whose metal-metal bonds had been weakened by the act of chemisorption, are thought to move out of their lattice positions. The "rearranged" tungsten atoms are then held responsible for the brighter image spots.

The ion images in the CO/W study just described were, however, taken at 78°K. Field induced reactions with liquid nitrogen cooling have already been discussed. It may be that the phenomenon observed with carbon monoxide is a field induced artifact, and does not truly show that metal atom rearrangement does occur.

Ehrlich has shown the surface species identified as adsorbed nitrogen atoms exhibit thermal behavior much different from that of tungsten ad-atoms (25). In addition, a recent single face FEEM study confirmed that nitrogen adsorption at 89°K and 295°K did not result in surface rearrangement of metal atoms on a scale required by Sachtler's arguments (139).

The problem of what the ion microscope actually observes during an adsorption study is by no means solved. The atom probe field ion microscope recently reported on by Mueller *et al.*, may be able to assist in clarifying this question (96).

An image point of interest is centered over a small hole in the phosphor screen of the conventional part of an ion microscope. The surface species is then pulse-field desorbed. After passing through the probe hole in the phosphor screen the unknown ion strikes the detector of a time-of-flight mass spectrometer. The problem with this ingenious device would seem to be that, even knowing the exact chemical identity of the desorbed species, it still may be unclear what the surface species was.

Field Effects, Limitations of Ion Microscope

The problems, and dangers, inherent in interpreting field ion patterns are particularly acute in adsorption studies. The primary cause of many of the difficulties encountered is the extremely high electric field employed in the imaging process. Field induced artifacts should be expected (some have already been described) even for metal surfaces by themselves. Among the effects catalogued to date are (116):

1. occupation of unusual sites (decoration atoms)
2. spontaneous formations of vacancies
3. dislocation loops in Mo, Nb and Ir (114) and Pt (116)
4. plastic deformation of iron
5. tip rupture (less refractory metals).

The occupation of unusual sites is an interesting phenomenon. Figure 27 is an enlarged reproduction of the ion image previously shown in Figure 21-a. The location of

decoration atoms are noted, e.g., along the [100]-zone lines. The brighter dots are believed to be individual metal atoms occupying positions where they are co-ordinated to only three other tungsten atoms (90). In moving from a kink site (CN = 4) to relatively more exposed positions, the tungsten atom sacrifices in metal-metal bonding. In return, however, its more exposed position leads to greater field penetration (increase in local field) and also to an increase in surface polarizability. The criterion for decoration atom stability, then, can be formulated as (90):

$$\alpha_3 F^2 - \alpha_4 F^2 \geq \Delta H_s/2. \qquad (26)$$

The negative pressure on the tip exerted by the viewing field results in a volume expansion (115). The resultant elastic expansion of the tip is found to be proportional to the voltage squared (i.e., field stress, $\sim V^2$, is proportional to strain -- Hooke's Law). Precise atom locations at the tip surface therefore cannot be inferred from ion images. Even if the linear displacements described just above could be estimated (as done in Reference 115) one would still have to contend with the effect of unsymmetrical atom arrangements. This factor can be expected to lead to curvature in the lines of force streaming radially outward from the tip surface, and hence to result in image distortion (22).

In order to be imaged, an adsorbate must be able to withstand the high field stress under imaging conditions. The

energetics for field desorption of an electronegative adsorbate parallel those of field ionization, with the exception that now the atomic state also interacts with the surface. To cause field desorption of an adsorbed species, the field must now overcome an additional energy term reflecting the adsorbate-substrate bond energy. At 21°K, fields required to remove an adsorbate layer from the central (110) plane of tungsten have been quoted as 5.3 V/Å for CO, 4.6 V/Å for nitrogen and greater than 5.0 for tungsten adatoms (25). Fields of 5.4 V/angstrom or more are required to remove hydrogen from tunsten.

Adsorbed hydrogen has not, however, been observed in the ion microscope (25,98). Field electron emission studies have established that adsorbed hydrogen is stable in the absence of imaging gas at best imaging conditions. However, after attempting to image adsorbed hydrogen in the ion mode, FEEM measurements indicate that hydrogen is gone. The presence of the imaging gas somehow promoted the desorption of hydrogen. Ehrlich, et al., attribute this to electron impact desorption by electrons originating beyond the critical distance during field ionization of the imaging gas (28). Mueller, et al., on the other hand, conclude that removal of the ad-layer during imaging is due to bombardment of the surface by neutral gas atoms possessing polarization energy due to dipole attraction (93). Bassett has reported a similar

effect when studying oxygen adsorption; he attributes loss of oxygen during the imaging process to the electron shower mechanism (5).

The impact of high energy electrons has also been observed to fragment adsorbed molecules. Thus, in an adsorption study of CO and N_2 the removal of substrate metal atoms along with the adsorbed layer was held due to the presence of adsorbed oxygen formed by dissociation of adsorbed carbon monoxide (98). An interesting observation in this study raised the question of whether the ion microscope could distinguish between atomic versus molecular adsorption. A nitrogen "ad-atom", adsorbed at 78°K, was observed directly over a tungsten surface atom in the middle of a net plane. On iridium, 78°K nitrogen adsorption was detected between adjacent metal surface atoms and was tentatively associated with molecular nitrogen.

A further problem directly attributable to the imaging conditions in the ion microscope is field decomposition. For example, adsorbed hydrocarbon molecules may have "dangling" hydrogens torn off by mechanical stresses alone, or perhaps through field ionization, provided the hydrogen extends far enough above the tip surface to reach into the ionization zone.

A final problem to be considered when employing the FIM in adsorption studies is that metal substrate atoms, on field

evaporated tips, may move between the time the clean surface micrograph is recorded, and when the micrograph of the adsorbate-covered surface is recorded. An example of this will be shown later. The color superposition micrograph indicates that one of the atoms on the $(1\bar{1}1)$ plane is missing after acetylene adsorption. In this case, the act of adsorption (or the imaging process) is clearly the culprit in causing the lattice atom to move since tip temperatures were never raised above 180°K in the experiment. Appreciable atom migration on field evaporated tips requires room temperature or higher tip temperatures. For example, appreciable iridium substrate atom movement in vacuum required temperatures of 450°C (18). Tungsten substrate atoms begin to migrate at about 420°C around (111) planes, but only at 470°C in (100) areas (6). Atoms at lattice steps, however, are often observed to migrate spontaneously at much lower temperatures. To guard against this, field evaporated tips employed in these studies were always heated to 300°K before adsorption experiments were begun to stabilize edge atoms.

The tone of the immediately preceding discussion has been somewhat negative; its purpose has been to set down the factors which must be considered when interpreting ion images. The history of field ion microscopy, however, belies a negative approach. Several years ago field ion microscopy was limited to a select group of refractory metals. The

introduction of hydrogen promoted-field evaporation and field ionization leap-frogged this obstacle. Alloy studies were of a confused nature, as it was not certain exactly what atomic species the image dots represented. The atom probe microscope should help immensely in this area.

Moreover, the information obtainable with the FIM bears on the basic question in surface studies, the atomic arrangement of surfaces and surface reactions on perfect crystal planes, studied on an atom-by-atom basis. The ion microscope's ability to produce and characterize reproducible surfaces of unbelievable atomic perfection alone makes the technique invaluable.

Experimental

Microscope designs

Designs for field ion microscopes depend, to a large extent, on the type of experiment to be conducted. In many surface studies, the object is to distinguish, unambiguously, the result of adsorbing a particular species on a clean metal surface. In this case, contamination by other species cannot be tolerated, and it is imperative that the entire microscope system be bakeable. An all glass bakeable system for both FEEM and FIM work has been described by Ehrlich, who employed it in his now classic nitrogen on tungsten experiments (29). Metal microscopes, bakeable to 400°C, fully equipped with power supply and vacuum system are available

commercially from Materials Research Corporation. A bakeable glass FIM with provision for easy tip changes has been described (65). Totally immersible field ion tubes have been employed in liquid hydrogen cryostats (33).

Microscope used in present studies The microscope used in the present studies is shown in Figure 28. Figure 29 shows a photograph of the arrangement of microscope and attendant facilities. The liquid helium storage dewar is located on the back of the vacuum rack.

The microscope was separated from back-to-back mercury diffusion pumps by a one-inch UHV valve. The microscope and 35 mm (O.D.) glass tubing connecting the microscope proper and pumping sytem was attached to a one inch piece of marenite. Bakeout temperatures of ~400°C were achieved by placing a movable baking oven against the marenite back board.

The particular design shown in Figure 28 was used to accommodate a continuous helium transfer heat exchanger element in the central dewar. This presented several difficulties in tube preparation and operation. Tip changes necessitated closing the valve to the pumps, backfilling the microscope with nitrogen, and unbolting the flange assembly containing the central dewar. Actually, however, since the time consuming operation in adsorption studies is the bakeout and outgassing routine, the small time required for tip changes was immaterial.

The outer dewar, which served as a radiation shield for the heat exchanger, complicated tube preparation. To obtain satisfactory conductive coatings on the interior walls of the tube it was necessary to cut the assembled microscope around the outer walls and coat the two resulting pieces separately. The problem was that flow patterns of the $SnCl_4$- nitrogen-oxygen mixture did not reach into the corner of the tube where the face-plate and outer tube wall met. At this time the utility of using trace amounts of water had not been realized, and it is possible that this could have obviated the two-step coating operation. To obtain conductive coatings on the walls of the inner dewar walls, the inner piece was placed in a large test tube to keep the coating mixture contained.

Electrical contact to the radiation shield was made by bending a one-half inch wide strip of 1/20th inch stainless steel into the shape of an omega, and forcing the clip over the dewar walls. This procedure resulted in a metal surface to which a tungsten wire, emanating from a 10 mil press seal, could make contact. The metal-metal contact was superior to a direct contact between the tungsten lead-in and the coated glass surface. During tube operation, particularly when the screen was operated hot, the metal-glass junction became non-conducting.

The dimensions of the microscope represent a compromise between many factors. In practice, screen diameters of six

inches have been used (59). Larger screen diameters possess the two-fold advantage of achieving higher magnifications, while assuring that image details are not lost in the grain of the phosphor screen. To take advantage of the larger screens, however, longer tip-to-screen distances must be employed; this limits the gas pressures which can be used to obtain well resolved images. A reasonable compromise has been reported to be about four inches for both screen diameters and tip-to-screen distances (142).

Both vertical and horizontal screen designs have been employed, the horizontal more often due to simplifications in tube construction. Vertical screens, however, are more convenient when the image is to be inspected closely.

Examination of the ion image

Visual observation of the ion image is possible with the naked eye, provided sufficient time is allowed for dark adaptation (generally, about 5-10 minutes before turning on the high voltage). In the present study, the time required for cooling the tip with the continuous helium transfer was spent in becoming acclimated to the dark. All panel lights, etc., were covered with black tape, and all electrical equipment giving off light was shielded to cut down the background light level. Pen-light flash lights were used when light was needed; red light bulbs were employed in the flash lights to maintain proper dark-adaptation.

Image examination on the phosphor screen is facilitated by the use of magnifying lenses. Reading lenses (M ~2) give some help while a watch maker's Loupe (M ~3-5) was used for more careful observation. One-quarter inch of the Loupe's support was sawed off to bring the image on the inside of the microscope face plate into focus when the Loupe was placed flat against the outside of the face plate. A ten-power optical alignment telescope was sometimes used for its excellent light gathering abilities.

Tip assemblies

The tip assembly used in field ion studies was identical to that described for FEEM experiments. The four lead press seal, to which the tip assembly was spotted, was sealed into the bottom of a 29/42 standard glass taper (70).

Radiation shield about tip

Image intensities can be greatly improved by encircling the tip with a metal radiation shield. Electrical contact to the shield is readily made to the metal cone through a press seal in the microscope body. The metal cone serves several purposes. For one thing, it shields the tip from extraneous fields and provides a uniform field gradient in the tip region. In addition, a cone of copper, silver or aluminum, in contact with the inner dewar filled with refrigerant, helps to cool the image gas, resulting in better accommodation. With liquid nitrogen in the central dewar, use of a metal radiation shield

results in a three-fold increase in image brightness (70,80).

To achieve the optimum effect, precautions must be taken to ensure good thermal contact to the inner dewar. In my experiments, this was accomplished by lapping a truncated copper cone over a standard taper similar to the one used on the microscope. To accommodate expansion during bakeout, a small slit was cut along the long axis of the cone. The resulting radiation shield was then wedged over the standard taper and held in placed by a corrugated steel band.

To eliminate sharp edges or spikes which could lead to field emission from cone-to-tip, the copper cone was first polished with fine emery paper to a high luster, and then etched in nitric acid. Aluminum cones, on the other hand, can be etched in a concentrated phosphoric acid-nitric bath (9:1) (94).

High voltage attachments

The microscope is conveniently run with the tip at a high positive voltage and the screen at ground. It is possible to run the screen hot, and an advantage to the latter mode of operation is that electrical discharges occurring during an attempt to photograph the image need not ruin the exposure. A more important advantage is that heating, current and temperature monitoring leads may be attached permanently to the leads running down the inner dewar. With the heat

exchanger element present in the inner dewar, the situation is more complicated. Capacitance effects, induced with the metal transfer tube and heat exchanger block in place, precluded running the screen hot in my experiments. It is possible that, by shielding the current and temperature monitoring leads (for example, with braided nickel shielding cable) this problem could have been overcome. This was not done, primarily, because effective heat transfer between the tips leads and cold helium glass was desired. As a result, the leads in the central dewar were made from 20 gauge nickel wire, encased in glass sleeving to prevent shorts from occurring between metal components in the inner dewar.

The D.C. high voltage power supply used in most of my FIM experiments was a Beta Electronics Model #206 which gave a continuously variable output of ~500-30,000 volts. In experiments requiring accurately known voltages a Sorenson high voltage supply, model 5030-4, was employed. Its output was variable between 1,000-30,000 volts, voltage being determined on a digitial voltmeter after dropping the high voltage across a voltage divider described by Gardner (36). Field electron emission imaging voltages were obtained from a Fluke 405-B, 1-3,000 volt output.

Heat exchanger assembly

Since a relatively gas tight assembly was needed for operating the heat exchanger, the electrical leads were taken

out of the inner dewar by means of electrical feedthroughs sealed in ceramic discs. If bakeout procedures were not employed, the nickel wires could have been soft soldered to the electrical feedthroughs. During bakeout, however, soft solder connections developed leaks. Careful silver soldering was therefore used instead and proved satisfactory.

The heat exchanger element used in these studies is shown in Figure 30. The idea for the heat exchanger was adapted from a variable temperature cryostat design employing a continuous helium transfer (131). Basically, better usage of the total refrigerating capacity of helium liquid was the goal in using the present design. Table 7 presents pertinent data for the three common low temperature coolants, helium, hydrogen and neon. It can be seen that the heat of vaporization of helium is some forty times lower than that of neon. By utilizing the refrigerant capabilities of the cold helium gas after vaporization, however, the potential refrigerating value of one liter of liquid helium at 27°K (b.p. neon) is only six times lower than an equal volume of liquid neon.

The heat exchanger, itself, consisted of an inner threaded copper cylinder, around which was sweated a hollow copper jacket. Copper was employed in the original design for its ease in matching. Lead would have been a better choice, at very low temperatures, as a heat sink material. The grooves in the heat exchanger were connected to stainless

Table 7. Refrigerating values for helium, hydrogen and neon

Refrigerant	Helium	Hydrogen	Neon
Boiling Point (°K)	4	21	27
$\Delta H_{vap.}$			
cal/mole	20	108	431
cal/liter	630	3835	25,645
Heat Cap.			
cal/g-deg	1.25	3.45	-
cal/l-deg	157.5	745.2	-
Total refrigerating value at 27°K			
cal/liter	4250	9050	25,645
Cost/liter	$3	-	~55

steel tubing which formed the receptacle for the transfer tube connecting the heat exchanger to the liquid helium storage dewar.

The transfer tube receptacle was fed through a brass plate. A similar donut shaped brass plate was welded onto a 40 mm metal-to-glass section on the tip of the microscope section. The two brass plates were bolted together, a gas-tight seal being formed by an O-ring which fitted into channels in both brass plates.

To control the rate at which liquid helium passed through the heat exchanger block, the rate at which helium

gas was allowed to leave the inner dewar was regulated by a simple bellows valve. In order to speed up the initial cool down, a port was provided in the tip section of the microscope. When liquid helium started to transfer (liquid could be seen in the inner dewar) the port was stoppered. The pressure applied to the liquid helium storage dewar was ordinarily provided by about 10 torr of helium gas.

The arrangement made rather efficient use of the refrigerant capabilities of liquid helium. The block was cooled to liquid helium temperatures, surrounding tip leads being cooled by radiation. In addition, the helium gas issuing from the bottom of the copper cylinder also cooled the press seal leads through convection. The load capabilities of the heat exchanger assembly were sufficient to restore tip temperatures to ~20°K in a few seconds after the tip had been heated.

No problems were encountered with the bellows valve freezing during six hour runs at ordinary helium throughputs. Absolutely no image blurring due to tip vibration caused by the continuous helium transfer was observed.

Helium consumptions required for a given tip temperature are plotted in Figure 31. Tip temperatures were estimated by using the tip as a resistance thermometer. Calibration points of resistance versus temperature were obtained by filling the central dewar with liquid and solid nitrogen,

liquid hydrogen and liquid helium. Below about 80°K the variation in resistance with temperature, for tungsten, is very slight, and indicated temperatures in Figure 31 are probably only good guesses. The ultimate criterion for this cooling technique, however, is provided by the ion image itself. Excellent low temperature helium ion images (temperature of tip at least as low as 30°K) were obtained with liquid helium consumptions of about one-half liter an hour (determined by measuring STP gas outputs with a wet-test-meter). The liquid helium storage dewar held five liters of liquid, which yielded between 5-8 hours run time in the desired low temperature range.

Helium ion images of a tungsten tip, partially field evaporated at room temperature, are shown in Figure 32 at estimated tip temperatures of 150°K, 80°K, 65°K, 57°K, 50°K, 40°K, 30°K and 20°K. No dramatic increase in either image resolution or image intensity is exhibited in the series of micrographs. Rather, a steady increase in image intensity was observed with lower tip temperatures. Between 150°K and 20°K, a decrease in exposure time of four was noted. The final micrograph in Figure 32 was obtained after field evaporation at liquid helium temperatures.

The advantages offered by the rather simple apparatus just described are two-fold: first, the use of liquid hydrogen, with its inherent dangers, was unnecessary. Second,

tip temperatures between 4°K and room temperature can be readily obtained. Hence, for adsorption systems where imaging gases other than helium are required, the best tip temperature for the desired imaging gas can be used (see Table 6).

If liquid hydrogen were to be used with the microscope design shown in Figure 29, means must be provided to vent escaping hydrogen gas. This is readily accomplished with the design used in my studies by simply capping the inner dewar with a rubber stopper. A glass tube, inserted through the stopper, is then connected directly to a vent line (39,74).

Microscope operation

When the desired tip temperature was achieved, the tip was flashed to ~1500°K to get rid of a portion of the contaminant gas layer. Vacuums obtained with liquid helium cooling were often below the x-ray limit of the Veeco gauge employed (~1×10^{-10} torr). Ordinarily, however, pressures were in the 10^{-10} torr range.

The microscope was then shut off from the pumps by closing the one-inch valve, after which helium was admitted through a helium diffuser obtained from General Electric Vacuum Products Corporation. The vycor thimble of the helium diffuser was outgassed prior to flowing helium gas through the diffuser jacket at a slightly higher temperature than required in microscopy experiments. When hydrogen was employed

as the imaging gas, a variable leak valve was inserted between the microscope and palladium thimble. In earlier experiments, high purity helium (or hydrogen) was admitted through a variable leak valve from one liter pyrex bottles (equipped with break-off-tips, J. T. Baker Chemical Company).

Imaging gas pressures were measured on a Hastings Sl-l Hi-vacuum thermocouple gauge controller, the gauge employed being #DV-18. This particular combination of controller and gauge records pressures in the 10^{-5} to 10^{-2} torr range, with greatest sensitivity in the 1-10 micron range. Ionization gauges can also be employed. The Veeco gauge, used to measure UHV pressures, is linear to ~5×10^{-3} torr (74) and was often used to follow the initial admission of helium, as it responds much more rapidly than a thermocouple gauge. A factor of ten in sensitivity (compared to nitrogen) was determined for Veeco gauges with helium by calibrating gauge pressures versus a McLeod gauge. A high pressure ionization gauge, described by Schulz and Phelps (125), is linear in the desired pressure range and is available commercially from Westinghouse Electric Company.

Phosphor screens

Screen phosphor can be deposited in the same manner described for field electron emission microscopy, i.e., via the puffer technique. As mentioned previously, the original Willemite phosphor employed was difficult to puff, yielding

phosphor particle sizes much too large. Grinding the phosphor in an acetone slurry did not help. A rather awkward looking, but highly efficient puffer was devised (Figure 33) which gave only the desired fine phosphor articles. Larger particle sizes were not swept along in the 1 inch diameter glass tubing nearly as rapidly as finer particles. By inclining the initial portion of the puffer upwards, the larger particles settled out and fell back down the tube; only a fine mist issued from the end of the tubing.

Bound phosphor screens can be removed by putting water into the microscope and rubbing vigorously with a soft cloth. Unfortunately, this procedure also partially removes the conductive coating which must be replaced before the tube can be used again. An alternative technique involves settling the required amount of phosphor from a suspension of phosphor in methanol (or acetone). Since helium ions do not penetrate the phosphor screen as deeply as electrons, field ion screens need to be corresponding thinner in order not to lose image details. A standard density quoted for ion microscopy screens is 0.5 mg/cm^2.

The required amount of phosphor was shaken with enough methanol to form about 1 cm of liquid in the bottom of the microscope. While allowing the larger phosphor particles to settle out (~1 minute), a buffer layer of about 2 cm of methanol was added to the microscope. The supernatant was

then decanted into a funnel leading into the microscope. The bottom of the funnel was bent into the shape of a U and was rotated slowly while the phosphor suspension passed through. This procedure provided uniform phosphor deposition. Without the buffer layer, it was discovered that the central portion of the screen received most of the phosphor, the edges very little. This was found to be due to a circular motion of the solution in the microscope upon addition of the phosphor suspension, which resulted in more rapid solution movement at the edges of the face plate than nearer the center.

Non-bonded screens, formed in this manner, did not appear to deteriorate appreciably faster than bonded screens. They could be replaced readily (merely by washing them off with water) and yielded excellent ion images.

The phosphors employed for FIM and FEEM were Willemite (zinc orthosilicate) phosphors. Zinc sulfide or zinc sulfide-cadmium sulfide phosphors could have been used in FEEM studies, and yield blue images. The blue phosphors are, however, useful only at ion current densities of less than 5×10^{-12} amp/cm^2. At higher currents they undergo rapid deterioration (104), suffering a 50% loss in efficiency in one-half hour at 10^{-9} amp/cm^2 (70). In a study of phosphor lifetimes, Sylvania Type No. 160 ($ZnSiO_4$:Mn) was found to have the longest half-life (~8 hours) and was also, after ZnS, the

most efficient. The No. 160 phosphor is, however, exactly the phosphor that yielded such poor phosphor screens employing ordinary screen making procedures in my experiments.

Phosphor efficiencies are found to be a weak function of temperature (77, 91). At 21°K, for example, the willemite phosphor used in one study was 18% less efficient with helium ions than the same phosphor held at room temperature (77).

Photography of ion images

In photographing ion images, the experimenter must reckon with both very low image intensities and extremely fine image details (image dots are often 0.1 mm in diameter). In addition, in the same image, intensities may vary over two orders in magnitude (9). To deal with the intensity problem, lenses with F/1 objective lenses can be used to advantage. The camera used in my studies was a Tektronix C-27 Oscilloscope camera with an F/1.4 objective lens which yielded 1:1 reproductions of the observed ion image.

In choosing a camera to photograph ion images it is important to realize the factors determining the speed of a particular lens. For example, the diaphragm lens settings (F/1.4 etc.) apply to objects at infinity. When object distances become less than about 5 times the focal length the light from a small area must be spread over the entire negative surface. This requires an increase in exposure time over that needed for objects at infinity. Exposure times at

infinity must be multiplied by a number taking into account this factor. If the ion image is to be reduced, as in 35 mm photography, the multiplicative factor can be formulated as:

$$\frac{t_i}{t_\infty} = \frac{\upsilon + f}{f}^2 = (M + 1)^2 \qquad (27)$$

where f = focal length of lens

M = magnification

υ = increase in lens-negative distance.

For a 1:4 reduction, $t_i/t_\infty \cong 1.6$ while if the object distance is reduced still further for 1:1 images, $t_i/t_\infty = 4$.

Polaroid Type 57-film (ASA rating, 3000) was used, for the most part, in these studies. It had the advantage of producing a positive immediately. If an image detail was missed in one exposure, another could be made. The only disadvantage encountered was the necessity of making a copy negative for reproduction purposes. In practice, however, the extra photographic step in making the negative did not appear to affect image details noticeably.

Tri-X (ASA, 400) and the faster Plus X (ASA,1200) can be used if negatives are desired. Mueller, however, states that Kodak 103 a-G spectroscopic film is best for ion microscopy, when used in combination with ethol 90 developer (78). The film is sensitive to green light of very nearly the same wave length range in which Willemite phosphors emit. Another advantage is low reciprocity failure during long exposures.

When developed for 6 minutes in ethol (no temperature given) the spectroscopic film was reported to have an ASA rating of 3000 (60), while another reference says it is ~20 times more sensitive than Tri-X (88). English workers in field ion microscopy have reported that for 35 mm work, Gevaert Scopic-G is a superior film (10).

The use of fibre optics face plates does away with the need for a camera (47). The contact negatives produces are reported to yield superior enlargements.

Mueller gives an equation for exposure times using an F/1 lens, liquid hydrogen cooling, zinc silicate screens and "high sensitivity photographic film" (75).

$$t(\text{sec}) = A/PV^3 \qquad (28)$$

P is inserted in microns, V in kilovolts, and A is a constant which has the value 10^5 for helium, $1.2\text{x}10^6$ for neon, and $3.3\text{x}10^4$ for hydrogen.

In practice, exposure times are usually determined from experience. An exact method, however, employs a photomultiplier tube to measure image brightness (60) from which exposure times can be estimated after suitable calibration procedures.

Field ion comparator A final photographic technique, which is indispensable for gaining the maximum amount of information from ion images, is color superposition (76,83) To determine ion image features which are different in a

series of micrographs, the first micrograph is illuminated in green light, the next in red light. The two images are optically super-imposed, and the resulting image photographed with color film. Features which are the same in both micrographs will appear yellow. Atoms present only in the first micrograph will show up green, while species present only in the second micrograph will appear red.

A schematic of the comparator built for the present studies is shown in Figure 34. Transparencies of the two micrographs to be compared are attached to opalized glass face plates on the front of the two housings. They are illuminated with opaque light bulbs, light levels being variable via variac control. Colors were provided by appropriate photographic filters or by red and green plastic tape pasted over the face plates.

Movement of the transparencies was accomplished with the aid of screw motion unislide assemblies obtained from Tropel, Incorporated, Fairport, New York (catalogue No. A2506C). The type RAD right angle drives for moving the unislide assemblies were obtained from Allied Electronics Corporation (catalogue item 422173). One of the housings moved permitting variation in distance between the attached transparency and the beam splitting mirror. This operation, in effect, changed the magnification of one of the transparencies. The other

two unislide assemblies moved the face plate of the stationary housing to provide careful adjustments in the other two directions.

The beam splitting mirror was situated to transmit half, and reflect half, of the light passing through each transparency. It was obtained from the Liberty Mirror Division of Libbey-Owens-Ford Glass Company (No. 501, high-efficiency coating).

Color pictures were taken of the superimposed ion images with a Pentax 1-a camera mounted on the comparator body. For color slides, Ektachrome or Ektachrome-B film were used, while if negatives are desired, Kodacolor film can be used.

Figure 35-a shows a low temperature helium ion image of a clean tungsten surface, 35-b, the same surface after a small amount of acetylene had been observed. The color superpostion of transparencies of 35-a and 35-b yielded 35-c where the effects of acetylene adsorption are noted in the several dozen blue-green image points.

Tip dosing

Tips were dosed, usually at 4°K, by admitting the desired hydrocarbon, from a reservoir on the back of the vacuum rack, through a variable leak valve. The delivery tube was bent under the outer nitrogen dewar, out of the ion beam path, and pointed at the tip region. This arrangement was workable, although a better method of introducing gas into the tip

region is to run the delivery tube through the outer dewars of the microscope (25). The required ring seals would not, however, be stable with the microscope design employed in this study, principally because to change tips, the metal high vacuum flanges had to be unbolted and then bolted together again.

After dosing at 4°K, the tip was heated to ~180°K to drive off physisorbed gas and ensure a chemisorbed layer.

A 1967 article discusses various means of dosing emitters with collimated beams (42). Although the Knudsen cell devices discussed are chiefly useful for depositing metals, the discussion of the problems of calibrating adsorption fluxes is pertinent to adsorption studies.

Non-Bakeable Microscopes

For many applications, not requiring stringent vacuum conditions, non-bakeable microscopes can be used. Aiding the experimenter, as discussed previously, is the fact that when helium (or neon) is the imaging gas, clean surfaces, once obtained, can be maintained indefinitely. With voltages kept near BIV, all contaminant gases will be ionized at some distance from the tip. With low temperature operation (4-50°K) to stop migration of impurities onto the tip from the tip shank, no foreign atoms can reach the emitter; one experiment, under conditions described above, recorded not a single impurity atom arriving at the tip over a period of five hours (72).

To take advantage of this, microscopes have been designed with grease joints (71,72), O-rings (59), and iridium metal seals (109). Whereas, to change a tip or make repairs, followed by bakeout requires a minimum of one day, down times with non-bakeable microscopes can be as little as thirty minutes. Pressures of $\sim 10^{-6}$ torr are ordinarily obtained in such microscopes. This can be further reduced, prior to image gas admission, through use of a metal getter (92), or activated charcoal (59). Filling the inner cold finger with a low-temperature refrigerant results in still lower pressures.

A microscope suitable for undergraduate physics laboratory experiments is marketed by CENCO.

A useful simplication for tip mounting assemblies can be used if tip temperature measurements are not required. Metal springs are made (after the idea of Mueller) by winding 10 mil tantalum wire around a 20 mil piece of tungsten rod. The resulting springs are spotted onto the tip mounting press seal pins. The tip loop is inserted through the coils as far as it will go. The protruding legs are bent inward slightly, after which the tip loop is pulled back out of the coils a small distance. In addition to providing a convenient, quick method of replacing tips, the coils also provide efficient cooling of the tip. The legs of the tip loop make good thermal contact with the inside of the coils and are shielded against radiation losses.

Emitter Cooling

Until recently, most FIM experiments have been conducted at either liquid nitrogen (~78°K) or liquid hydrogen (~21°K) temperatures. Compared with any refrigerant with a higher boiling point (save perhaps neon), liquid hydrogen cooled emitters produce images with better resolution and contrast, with greater image intensities. In addition, contamination problems are reduced since residual gases will condense on the 21°K surfaces. For tip radii of ~500 angstroms or larger, only low temperature refrigerants will produce good resolution (78,95). The use of liquid nitrogen cooling is sometimes complicated by the field induced tip etching reaction mentioned previously. In Figure 36 liquid nitrogen cooled helium ion micrographs of a tungsten tip are shown. These micrographs were taken before techniques for good quality ion micrographs were mastered. They do illustrate, however, the much poorer resolution obtained at 78°K versus low temperature micrographs. The two micrographs, one of only a partially field evaporated tip, the other of the fully developed tip, show an interesting streak pattern. The streak is associated with a grain boundary as evidenced by the extra planes apparent in the upper right hand portion of the fully developed tip. On original micrographs an axially directed screw dislocation could be followed for about eight spirals. On the reproductions the contrast is not good

enough to allow the atom rings to be followed. The relative position of the line of mis-orientation in the two crystals did not shift appreciably during repeated field evaporation sequences. This could indicate, for example, an exially directed screw dislocation.

My results on the temperature variation of helium ion images have already been presented. My experiments, however, were conducted without a metal radiation shield about the tip. With the cone in place, liquid nitrogen images are found to be five times more bright with "better resolution" (70) than room temperature images. Pumping on the liquid nitrogen with a fore-pump easily solidifies nitrogen (63°K), and further reduction of the nitrogen pressures above the solid can reduce the temperature even lower. Reducing the emitter temperature from 78°K to 53°K produces a 20% increase in image intensity but a considerable improvement in image resolution (70). Reduction in temperature from 78°K to 21°K results in approximately a two-fold intensity gain. Image contrast and resolution are, however, far better at the lower temperature.

In the last few years other coolants have seen wider use. Liquid neon (b.p. 27°K) cooling produces adequate low temperature images, while the working range (F_e - F_c) for W, Ir, Mo and Ni increased by 10-30% (8). An initial 0.5 liter charge of neon lasted for 10-15 hours. At the moment, the cost of ~$100/liter is prohibitive for most usages.

The remaining low temperature refrigerant, liquid helium (b.p. 4°K) was probably not tried until recently due to an earlier observation that the helium imaging gas, at its boiling point, would be adsorbed (70). This was supposed to smear out field distributions and produce poorly resolved images. Such is not the case, and liquid helium cooled images have been reported by several investigators (4,129). The first reference used a shielded liquid helium reservoir in thermal contact with the tip leads while in the second paper, a metal block was cooled by flowing liquid helium through the block which was in thermal contact with the tip. The quality of liquid helium images has already been shown to be excellent from images obtained with the variable temperature field ion microscope described in this presentation.

Two other variable temperature field ion microscopes have been reported (52,109). The first employed a Collins helium refrigerator to flow cold helium gas around the tip leads. The particular arrangement described operated between 10°K and 35°K. The cost of the refrigerator itself, ~$21,000, precludes widespread use of such a technique. An elegant variable temperature microscope has been described by Klipping and Vanselow (52). A continuous helium transfer, in this design, is fed through a heat exchanger to cool a control medium fluid at the bottom of the cold finger

containing the tip leads. Tip temperatures are determined by measuring the vapor pressure of the control fluid. Liquid helium flow rates, and hence temperatures obtainable by the design, are regulated automatically by a valve operated in conjunction with a mechanical pressure gauge. A table of possible fluids for use from 4°K up to room temperature is provided by Klipping and Vanselow. To maintain tip temperatures in temperature regions where control fluids are not available, Klipping and Vanselow described a second heat exchanger technique similar to the one described in this report. A continuous flow of liquid helium is employed to cool a metal heat sink in thermal contact with the tip. Fine temperature control is achieved by also incorporating an electrical heater in the heat exchanger element. Helium consumptions for the vapor pressure and electrically regulated heat exchangers are quoted as 0.5 and 0.1 liters per hour, respectively.

Commercially available Joule-Thomson hydrogen liquifiers are available for ion microscopy experiments from Air Products and Chemicals, Incorporated.

Resoltuion

Considering resolution to be limited by diffraction and transverse velocity effects, it is possible to derive an expression for the ultimate resolution for the field ion microscope (70). With the imaging gas fully equilibrated

to tip temperatures, and neglecting the diffraction effect, the result can be written as:

$$\lambda \simeq 2.5 \times 10^{-2} \sqrt{Tr/F} \text{ (angstroms)} \qquad (29)$$

with T in degrees K

r in angstroms

F in V/angstrom

Values calculated from Equation 29 are tabulated in Table 6 for the imaging gas considered. The three shortest atom spacings on tungsten are 2.7Å, 3.16Å and 4.5Å. Low index planes for tungsten exhibiting these spacings were shown previously in Figure 18. In Figure 35 previously shown, the $(11\bar{1})$ plane of the clean surface micrograph contains 23 atoms, separated from one another by 4.5Å, completely resolved. In the same Figure, the atom rows of the (121) plane are visible (distance across the atom rows is 4.5Å); inside the atom rows touching atoms with a center-to-center distance of 2.7Å are resolved.

In Figure 37 further illustrations of the resolving power of the helium ion microscope are given. In the first Figure of a partially field evaporated tip 11 atoms are present on the (100) plane. On the (310) plane a chain of atoms is visible. On both of these planes the atom spacing concerned is 3.16Å. In the next micrograph in Figure 37, 16 atoms are visible on the $(11\bar{1})$ plane while the 3.16Å spacing between atom rows is resolved on the (310) and (130)

planes. Two decoration atoms are visible on the central (110) plane.

In the last micrograph of Figure 37, the area around the central (110) has been imaged. Since the local radius of curvature in this tip region is relatively larger than, for example, in the {111} regions the imaging voltage had to be increased above the value where the [110]-zone line planes are in best resolution. Helium ions are imaged too far away from the surface to render the [100]-zone in atomic detail. If the imaging voltage is decreased to record image details there in atomic resolution, the central (110) region will not be imaged since the local field above this tip region will be too low. Helium gas atoms will be drawn to the higher field regions where ionization can occur.

Resolutions experimentally obtained fail to reach calculated values for several reasons, the finite diameter of the imaging gas atoms plus the fact that ionization occurs 4-5 angstroms above the surface. Field profiles at this distance may be smeared out enough such that adjacent atoms will not yield distinct image points.

Tip Radii Determination

Local tip radii can be calculated from an ion image by counting the number of net planes, n, between two known crystallographic planes (70). If S is the step height and ζ the interplanar angle:

$$r = nS/(1 - \cos \xi) \qquad (30)$$

Tables of step heights and angles are provided in Mueller's review article (70). For two of the prominent planes on tungsten, Equation 30 can be written as:

$$r = 16.7\ n \text{ angstroms, } (110) - (112),$$
$$40.5\ n \text{ angstroms, } (110) - (123). \qquad (31)$$

Local tip radii, calculated in this manner can vary over the tip surface by factors of two or three (24, 70). Reasons for variations in local tip radii have been discussed in the section on field evaporation. Radii can also be obtained by direct observation in an electron microscope, from Fowler-Nordheim field emission plots (81) and from knowledge of relative best image voltages for the planes under scrutiny (97).

Magnification

The overall magnification of an ion microscope will, of course, depend upon the tip-to-screen distance. Magnifications can be computed from a given ion image by measuring the linear distance, d, from the (112) plane to the (121). This 60° span of the ion image is equal to the tip radius. The magnification, M, is computed from:

$$M = d\,[(112) - (\bar{1}21)]/r \quad . \qquad (32)$$

Magnifications of one to ten million are commonly obtained. It is important to realize that magnification by itself

is not the important parameter when discussing the field ion microscope's performance capabilities. The electric lines of force from an emitter surface are the same whether the emission microscope is employed in the FEEM or FIM mode. Field electron images represent the same magnifications as ion images. The former image, however, differentiates only between tip regions the size of planes. The ion microscope, on the other hand resolves individual atom spacings.

Characterization of an Ion Image

The ion image is a two dimensional map of atom locations on a three dimensional tip surface. Generally, orthographic projections are used to identify poles in an ion image although none of the stereographic projections commonly used accurately represent field ion images (11). An orthographic projection for a cubic crystal was shown in Figure 3 with the planes commonly observed for b.c.c. tungsten emitters. Numerous references can be found containing crystallographic maps for most of the crystal systems likely to be encountered, and computer programs have been published for obtaining angles between planes in arbitrary crystal systems (49).

A recent publication gives a scheme for identifying the planes in an unknown crystal system from ion micrographs (102). The measured distance between two poles on the micrograph, d, is equated to M, the over-all magnification, R, the projection radius, and the interplanar angle ζ:

$$d = MR\zeta \tag{33}$$

Neither M or R are known in general. If, however, the index of the central pole is known (or guessed), the product MR can be computed if the indices of a second pole on the micrograph are known (hence ζ is known). In practice, a trial and error procedure may be needed. Once MR is determined, the interplanar angle between the central pole and any unknown plane can be determined by a simple measurement of d on the ion image.

Image Intensification

Various methods of producing brighter images have been mentioned thus far, based on lower operating temperatures, radiation shields, higher gas pressures and addition of hydrogen to the imaging gas. Imaging of small tips may still require excessive exposure times employing any of the above techniques. Image intensities can be increased substantially by shielding the tip from the applied field with a coil plugged into the tip mounting springs along with tip loop. The degree of shielding determines the increase in voltage needed to obtain an ion image. Decreases in exposure time of up to one hundred are cited for this simple technique (95). Image intensities are directly proportional to imaging gas pressures. Upper pressure limits for helium have been mentioned as ~5 microns. By enclosing the tip region except for a small aperature through which the ions

can travel to the screen, the pressure in the tip region can be increased to 50-60 microns; the large volume of the microscope can be maintained at a pressure of less than one micron. The "dynamic gas supply" technique can decrease exposure times by as much as a factor of fifty (142).

Additional means of producing an intensified ion image can be grouped into internal and external categories. In the first group belong post acceleration and ion-electron image conversion. Post acceleration takes advantage of increased phosphor efficiencies with higher energy ions. The ion beam is accelerated through a fine mesh whereby gains up to ten are possible for helium imaging (16). Ion-electron image conversion transforms the ion image into an electron image by generating secondary electrons on a fine metal mesh in the path of the ion beam (16,12). Gains of four for helium and eighty for neon are possible.

External image intensification would seem to be the only acceptable procedure for adsorption studies. Drechsler originally proposed that the photon image from the phosphor screen be intensified electronically, suggesting the use of a super-orthicon camera (23). The most successful usage of external image intensifiers has been by Mueller who employed a commercially available three-stage photoelectronic image converter tube (60). The finest resolvable image spacings are resolvable with this arrangement at gains of 10^5 which

permits motion picture taking of rapidly occurring events on an emitter surface.

Photoelectronic image intensifiers are the subject of a review article by McGee (58) while image converter and intensifier research has been reviewed agin more recently (124).

Applications of FIM

Applications of the FIM can be grouped into four major categories:

1. Metallurgical
2. Bio-molecule structure determination
3. Mass spectrometry
4. Adsorption

A discussion of published results from the above listing would require another chapter equivalent to the entire presentation of field ion microscopy thus far given. Rather than elaborate on the results obtained with the technique only a brief outline of the type of problems amenable to study by the FIM will be given. Extensive listings of FIM applications can be found in Mueller's 1960 review article (70). More recent literature is covered by the same author in Ann. Rev. Phys. Chem. 18: 35. (1966).

The FIM has realized its greatest usefulness in the domain of metallurgy; here, its ability to depict the atomic lattice in atomic resolution has been utilized to display

defects in metals that can only be inferred by other experimental approaches. Field evaporation enables the FIM experimenter to peel away outer layers of tip metal one by one to reveal the three dimensional constitution of grain boundaries (and twinned crystals), stacking faults and other dislocations. The distribution of voids and interstitials in the bulk metal can be determined, for example, after irradiation experiments. Alloy constitution, order-disorder transformations and domain structure are all amenable to investigation on an atomic basis in the FIM. Corrosion experiments, for example, oxidation or carbiding, can often be conducted in an ion microscope.

Field ionization of gas phase species generally produces cracking patterns which are considerably more simple than electron fragmentation patterns. Field ionized particles are also nearly iso-energetic, which leads to applications of the techniques of field ion microscopy to molecular beam research.

Bio-molecules are usually so complicated that structure analysis is difficult, if not impossible. The conformation of such species on metal surfaces has been investigated by embedding the molecules in a metal matrix. Field evaporation then yields the outlines of the bio-molecule.

The use of the FIM in adsorption has been touched on previously. Questions remain as to exactly what ion images

of adsorbate ad-layers truly represent. There is, however, no other experimental technique which depicts atomic surfaces in atomic detail, and, if past history in the field is any indication of things to come, the ion microscope will eventually prove its merits in this field. The classic experiments of Ehrlich, et al., with nitrogen adsorption on tungsten, have already demonstrated the power of the technique (25). Whereas the central (110) plane in field emission is dark and cannot be investigated easily, the ion microscope has clearly demonstrated that adsorption does occur on the (110). Moreover, the (110) form of nitrogen, visible in 78°K adsorption experiments, has been identified as the so-called γ-nitrogen observed by a variety of other techniques. It is exactly in the area of determining surface heterogeneity effects in adsorption and migration experiments that the field ion microscope should find its greatest application.

Results

Goals

The goals set in my field ion microscopy studies of hydrocarbon adsorption were two in number:

1. to ascertain whether surface heterogeneity effects were operating in olefin and alkyne adsorption, and
2. to determine whether adsorption geometries could be inferred from ion microscopy, i.e., to determine

over what surface metal atoms hydrocarbons were bonded.

Most experiments with ethylene were conducted at tip temperatures of 78°K prior to development of the continuous helium flow heat exchanger. A field induced tip etching reaction was observed with liquid nitrogen cooling which precluded adsorption experiments at this temperature. Ion micrographs taken, however, showed rather uniform adsorption as indicated by a random arrangement of bright emission centers. In this respect, my results with ethylene are similar to unpublished results of J. R. Arthur. Image points due to ethylene adsorption appear in all crystallographic planes. Of particular note is the fact that ethylene adsorption occurs on all the low index planes of tungsten including the central (110) plane. In field electron emission experiments, the low index planes remain dark after adsorption.

Acetylene adsorption experiments were conducted with the tip cooled by liquid helium. Generally, adsorption was carried out at liquid helium temperatures, after which the tip was heated to 180°K to ensure a chemisorbed deposit. Dosage levels were monitored with a field electron field. Generally, the variable leak valve to the hydrocarbon supply flask was opened carefully until a current increase was detected; the valve was then immediately closed. This procedure enabled very light hydrocarbon doses to be administered. To protect the tip from further adsorption, the FEEM field to the

screen was turned off and a positive voltage, slightly less than the BIV recorded for the clean surface image, was applied to the tip leads. The valve to the pumps was closed and helium imaging gas was admitted, after which the voltage applied to the tip could be adjusted to obtain the desired image details.

Results for light acetylene doses were given previously in Figure 35. Heavier acetylene doses are shown in Figure 38. As with ethylene, acetylene adsorption occurs uniformly on all crystallographic planes. The central (110) exhibits several new bright dots in all three cases shown in Figure 38. Removal of substrate metal atoms has occurred on the $(11\bar{1})$ in the micrographs after acetylene adsorption in Figure 38-a and from the (111) plane in Figure 38-c.

Image points for acetylene were most often circular. In some cases, however, the circular dots had a single tail or streamer appended. This is illustrated in Figure 38-b. Such streamers have been observed previously for CO, N_2 and O_2 as well as for tungsten adatoms; in these cases triplet structures were observed (27). The exact nature of the structured image point is not understood at this time. Ehrlich, however, has pointed out that the screening charge about an impurity in a metal does not decrease monitonically with distance (27). Rather, it oscillates in intensity, falling off with distance. Presumably the satellite image dots represent, from this sort of picture, a maximum in the

oscillatory behavior of the electronic perturbation caused by the presence of an adatom on the metal surface.

Helium ion microscopy of hydrocarbon surfaces definitely shows that ethylene and acetylene adsorption can occur on all tungsten planes exposed on a field evaporated tip. The question remained, at this point in my studies; what do the bright emission centers observed after adsorption represent? Problems caused by the imaging field have been discussed in previous sections on "visibility of adatoms", and "field effects, limitations of the FIM". Being aware of these problems, real or only feared, an attempt was made to ascertain the effect of the imaging field on the stability of hydrocarbon ad-layers.

Decomposition experiments were conducted in which, rather than determining the thermal stabilities of hydrocarbon ad-layers as in FEEM studies, applied imaging voltage was used as the perturbing variable. The field decomposition studies were originally attempted in the microscope design shown in Figure 28 . Vacuums of 10^{-10} torr, however, were not sufficient to prevent contamination of the tip by residual gases over the cumulatively long periods when a FEEM field was used to measure work functions. (as in thermal decomposition studies, one experiment might require 3-5 hours.) As a result, field decomposition studies were conducted in a FEEM tube in a liquid helium cryostat.

A field evaporation end form of a tungsten emitter was prepared by first observing the voltage necessary to produce a field electron emission pattern. A reversed polarity voltage, of approximately ten times the observed FEEM viewing field, was then applied for about 1 minute. After reversing the polarity of the field again, the voltage required for an emission current of 5×10^{-8} amps was noted. The procedure was repeated at increasingly higher field evaporation voltages until the FEEM voltage required for 5×10^{-8} amps emission current did not change appreciably between successive field evaporation intervals. This indicated that tip end-forms were not changing. In essence, the procedure is a single point approach. Field electron emission patterns were observed after each field evaporation operation to check when a field evaporated end form was achieved.

Monolayer coverages of ethylene were then applied to the tip, and the tip was heated to about 200°K to drive off physisorbed gas. Field decomposition of the adsorbed layer was monitored by applying a negative voltage to the screen for one minute intervals, followed by a F-N work function measurement. Average field strengths were estimated by assuming the voltage needed to prepare a field evaporated end form corresponded to 5.0 volts per angstrom.

The results for ethylene are shown in Figure 39 which shows a plot of work function versus applied voltage (and

field). A relatively uniform work function, below that of the clean surface work function value, was observed up to a field strength of about two-thirds that needed for helium ion imaging. At higher voltages, the work function values increased, reaching a value nearly that of the clean surface work function at 4.5 volts per angstrom. Field electron emission micrographs at a field desorption voltage setting slightly higher than the original field evaporation field indicated a substantially clean tungsten pattern. The implications of the experiment just described are that adsorbed hydrocarbon layers are not stable in the high fields required for helium ion imaging. The bright emission centers observed in ion micrographs do not represent intact hydrocarbon species.

Several mechanism may be operating to decompose adsorbed hydrocarbons. Field ionization of atoms dangling far enough above the emitter surface to reach into the ionization zone (4-5 angstroms) has been previously mentioned, but it does not seem geometrically possible for ethylene hydrogens to extend that far from the metal surface.

Field desorption of electronegative adsorbates has been alluded to in a previous discussion of the effects of high viewing fields. As mentioned, the strength of the substrate-adsorbate bond represents an additional energy term which must be overcome by the applied field in order to cause field

desorption. Actually, applied fields in the FIM might strengthen adsorbate-adsorbent bonds. This is most easily seen if the olefin were pi-bonded to a single metal surface atom. The applied field has been seen to deplete electronic charge in regions between ion cores. At the ion core itself, the charge is held more tightly (13). The degree of occupancy of spatially directed metal orbitals may, however, be affected by the strength of the applied field, the field acting to reduce the charge density in the surface metal orbitals. This would make the metal surface atom a stronger Lewis acid which would interact more strongly with the electron-rich bonding π-molecular orbital of the olefin. Such a picture does not take into account "back bonding" from surface metal d-orbitals to anti-bonding π-molecular olefin orbitals. Nor can it be reconciled with the fact that usually lower metal oxidation states form more stable olefin-metal complexes than higher metal oxidation states (7).

Field desorption would not necessarily become more difficult, however, if surface metal-olefin bonds became stronger. In the process of forming stronger metal-adsorbate bonds, electronic charge may be depleted between adjacent metal atoms. This would lead to field desorption of an adsorbate-metal complex.

A further route for decomposition is based upon the high tensile stresses to which the tip and an adsorbate are

subjected. Field stresses of 10^{11} dynes/cm^2 may be sufficient to mechanically rip apart hydrocarbon molecules. The relevant fields of ~5 V/angstrom are of the same order of magnitude as those holding together an alkali halide crystal.

Figure 39 might possibly be interpreted as indicating a two step decomposition reaction from the shoulder appearing between 3.5 and 4.2 V/angstroms. If this is true, the field decomposition of ethylene could be explained by a set of reactions similar to those applicable to thermal ethylene decomposition on metal surfaces.

1. $\underset{*}{CH_2} - \underset{*}{CH_2} \rightarrow \underset{*}{CH} = \underset{*}{CH} + H^+ + e^-$, F ~3.5 V/A
2. $\underset{*}{CH} = \underset{*}{CH} \rightarrow \underset{*}{2C} + H^+ + e^-$, F ~4 V/A
3. $\underset{*}{C} \rightarrow C^{+n} + ne^-$, F ~5 V/A

Work function values for field decomposition experiments do not exceed the clean surface work function value by nearly so much as in thermal decomposition experiments. This could be due to several factors. First, thermal decomposition of hydrocarbons definitely places hydrogen on the metal surface as demonstrated by self-hydrogenation results to be given in the next chapter. Hydrogen gives rise to a positive $\Delta\Phi$. Carbon, in the form of graphite, gives a uniform emission pattern with a very small positive $\Delta\Phi$ (51). Carbon in graphite form is therefore not present in thermal decomposition

experiments but could be present in field decomposition experiments. In thermal decomposition experiments, carbon migration into the bulk becomes appreciable at temperatures less than 600°K (35). Surface carbide layers may form in thermal decomposition studies but they also would not lead to work functions differing markedly from 4.50 eV.

FLASH FILAMENT SPECTROSCOPY

Introduction

Field electron- and field ion-emission microscopy monitor only reactions occurring on a metal surface. Information obtainable by the two techniques, although highly suggestive, does not provide clear-cut evidence concerning either the stoichiometry or structure of surface species.* An indirect approach to the characterization problem involves indentifying species which appear in the gas phase during surface reactions. For this purpose, the flash filament spectroscopy (FFS) technique is singularly effective.

Experimental

Reaction cell

Figure 40 presents a schematic of the reaction cell and attendant electronic equipment used in this study.** The reaction cell was pumped by two back-to-back mercury diffusion

---

* With respect to this limitation, it can be safely alleged that no experimental technique for studying surface reactions can determine the nature of ad-species at this time. The two most direct approaches to the problem, surface infrared spectroscopy (55), and low-energy electron scattering (110), have not been as useful in characterizating vibrational frequencies of adsorbed species as their gas phase counterparts.

**The equipment, which proved so effective in hydrocarbon decomposition studies was wholly assembled by R. R. Rye, and details of its construction and operation can be found in Rye's dissertation (120).

pumps, the degree of pumping being variable through a magnetically operated ground glass valve. All of the glassware shown in Figure 40 was bakeable to 400°C.

The metal surface in FFS studies was a 20 cm long segment of 5 mil tungsten wire (geometrical area $\cong$ 0.8 cm^2), which was spotted onto a four lead press seal sealed through the bottom of a re-entrant dewar. Wire temperatures for isothermal portions of these studies were determined by the coolant in the dewar assembly. Liquid nitrogen provided an average filament temperature of ~95°K, while for room temperature operation, the dewar was filled with water. Filament temperatures were measured by using the wire as a resistance thermometer using the calibration data of Rye (120).

Total pressures were measured with a Westinghouse 5966 ionization gauge. Generally, residual pressures in the reaction cell, prior to cleaning the filament and adsorbing hydrocarbon, were $\leq 5 \times 10^{-10}$ torr. To ensure that reactions observed in FFS experiments were occurring on the tungsten filament and not on other metal parts of the system, the ion gauge was always turned off before beginning an experiment. As a further check, a monolayer dose of olefin (or alkyne) was admitted to the reaction cell, and the gas phase hydrocarbon was pumped away. The filament was then heated to ~1000°K to deactivate the tungsten wire surface. Hydrocarbon was then readmitted to see if any reaction could be

detected, for example, in the mass spectrometer. Only the cracking pattern of the hydrocarbon admitted was ever observed. Experimental cracking patterns, as well as cracking patterns from API tables were given previously in Table 2.

Mass spectrometer

Description The mass spectrometer used in these studies was a General Electric Partial Pressure Analyzer, Model 22PC110. It was bakeable to 400°C, the electromagnet for the 90° magnetic sector being removed before bakeout. The output of the mass spectrometer (10^{-6} to 10^{-10} amps) was fed into a Keithley Model 415 Micro-micro-ammeter. The output of the electrometer, 0-1 volt full scale, was then examined either on a Tektronix Type 564 Storage Oscilloscope, or by an x-y recorder or oscillographic recorder.

The sensitivity of the mass spectrometer was ~1×10^{-10} torr (using 1 second electrostatic scans) at the beginning of my experiments. With continued exposure to hydrocarbon ambients, the electron multiplier gain deteriorated at a slow but steady rate. To provide an estimate of partial pressures represented by observed ion currents, the mass spectrometer output was periodically calibrated against ion gauge pressures. A gauge factor of 5 was used to convert observed ion gauge pressure to equivalent nitrogen pressures.

As seen in Figure 40, there was no direct line-of-sight between the tungsten filament and the ionizing region of the mass spectrometer. Future flash filament studies should be carried out with a line of sight between filament and mass spectrometer to ensure that all species desorbed from the filament are detected.

Operation The mass spectrometer was operated in three different modes: (1) To obtain cracking patterns of a particular hydrocarbon, the sweep base voltage was set at 1000 volts, and the magnetic field was continuously varied over a 3 minute scan. Ion peaks were recorded on an x-y recorder. (2) Monolayer coverages of hydrocarbon yielded mostly hydrogen when heated slowly to 1000°K. Other gas species, such as methane or ethane, could be detected but only at ion currents 2-3 orders of magnitude lower than hydrogen ion currents. As a result, decomposition processes were conveniently followed by "sitting on" mass 2. This was accomplished by setting the sweep base voltage at 1000 volts, and adjusting the magnetic field to maximize the ion current for a particular mass peak on the electrometer. The rate of change of mass 2 with filament temperature was recorded on a two-pen Moseley Autograf x-y recorder (Model 136A). One pen was used to monitor ion current, the second pen recorded the voltage drop across the filament, both as a function of time. (3) When more than one mass peak was to be followed,

or when isothermal hydrogenation studies were conducted, the magnetic field was set at a value to examine a particular mass range of interest when the sweep voltage was centered at a given value. The values for magnetic field and sweep base voltage are interdependent and were most easily determined by experience. The voltage range scanned and the number of sweeps per second were both variable. The first variation affected the extent of the mass range scanned. Generally, 1 second or 0.1 second scans were used and were recorded on a high speed oscillographic recorder. Two oscillographic recorders were employed in these studies, a modified Sanborn Model 297, and a Brush Recorder Mark 280.

Gas admission

Hydrocarbon gases were admitted through UHV variable leak valves while hydrogen was admitted through an UHV Type-C valve. Hydrocarbon pressures were estimated by observing oscilloscope traces, the mass spectrometer being operated in mode 3 at 1 scan every 0.1 second.

Equipment list for mass spectrometric laboratory

In Table 8 equipment required for flash filament spectroscopy experiments is listed. The mass spectrometer listed is a Quadrupole-type, whereas a magnetic sector instrument was used in these studies. The quadrupole-type, however, is able to scan several hundred mass units in one sweep at much faster sweep rates than the instrument described in

Table 8. Equipment list for mass spectrometric laboratory

Item	Cost
Mass Spectrometer (Quad 150), controller	$9000
Diffusion Pumps (2)	250
Ultra-high Vacuum Valves	1500
Thermistor Gauge Controller	150
Ionization Gauge Controller	500
Oscilloscope	2000
X-Y Recorder	2000
Vacuum Rack	100
Liquid Nitrogen (25 liters/week)	
Fore-pump	250
Spot Welder	500
Glass Cut-off Wheel	100
Picoammeter	800
Filament Power Supply	200
High Speed Oscillographic Recorder	3800
Gas supplies, torque wrenches, metals chemicals, switches, etc.	
	21,000+

this report. The faster sweeping capability is perhaps not as important as the ability of the quadrupole-type mass spectrometer to sweep wider mass ranges. While the instrument employed in these studies could cover only a dozen mass units, the quadrupole-type can, for example, scan masses 2-150.

Cleaning of wire

The filament was first cleaned by flashing momentarily to temperatures of about 3000°K. Whereas in FEEM experiments the emission pattern is a most sensitive indicator of surface cleanliness, in flash filament work more indirect procedures were required to ascertain the cleanliness of the filament. Generally, scope traces of mass 28 were observed during filament flashes. As the filament temperature was increased, mass 28 pressure bursts also increased until, at a particular temperature, the mass 28 peak would begin to decrease. Mass 28 follows, in part, carbon monoxide partial pressures. Part of the pressure rise of CO is due to carbon being desorbed from the filament and striking the walls of the reaction flask, the glass walls providing oxygen for CO formation.

As a further check on reproducibility, if not cleanliness of the filament, hydrogen flash decomposition traces were periodically recorded. On "clean" tungsten wires, 95°K adsorption of hydrogen produced five distinct hydrogen forms in the decomposition spectrum, at reproducible

temperatures. On partially contaminated filaments, the highest temperature (β_2) hydrogen was shifted to higher temperatures.

Decomposition experiments

Previous FEEM experiments by members of this group, in addition to work reported in this presentation, have indicated that hydrocarbons do not undergo surface reactions in the chemisorbed layer below 100°K (2,21,36). As a result, adsorption was always carried out at ~95°K. The desired mass peak was located (usually mass 2) and the filament flashed with a constant known current (usually 1 amp). Filament resistance and mass 2 ion current were recorded using the mass spectrometer in mode 2.

A relatively slow flash rate was employed (~20 seconds required to heat to 1000°K), the heating being terminated at 1000°K by a trigger mechanism described by Rye (120). The slow flash rate was used in these experiments to attain better resolution of multiple desorption peaks. For most of the experiments described in the report, the entire tungsten filament was used as a resistance thermometer. In others, sensing leads tapped off the central 14 cm of the filament. The latter technique will yield more accurate temperatures as the 1 cm portions of the filament nearest the dewar are much colder than the central portions of the filament. In fact, recorded temperatures at equivalent points in identical

flashes were significantly lower when the whole filament voltage drop was measured.

Hydrogenation experiments

The filament was cleaned and allowed to cool to 300°K. Cis-2-butene was admitted through a variable leak valve and masses 39-43 were scanned every second using the Sanborn oscillographic recorder to record spectra. The principal mass peak for cis-2-butene is at mass 41 while the experimentally determined 39 peak was ~50% of mass 41. (see Table 2 for cracking patterns) No peak at mass 43 is observed for cis-2-butene. N-butane's principal peak is at mass 43, with a 38% peak at mass 41 and an 18% peak at mass 39.

The amounts of butene and butane in the reaction cell were therefore computed by noting the ion currents for masses 43 and 41. Mass 43 ion current was made up from butane only, while mass 41 ion current contains ions from both butane and butene. To find the ion current due to butene alone, 38% of the mass 43 ion current was subtracted from the mass 41 ion current. Ion currents were converted to partial pressures from calibration runs using the ion gauge as a pressure.

Results

Self-hydrogenation of cis-2-butene at 300°K

Results for two-self-hydrogenation runs are shown in Figures 41-a and b. Ion currents (left ordinate) for butene and butane are plotted as a function of time. Partial pressures

are given on the right hand ordinate scale. The two examples shown illustrate the effect of varying the rate of admission of cis-2-butene. Figure 41a presents data for a slower butene admission rate than that shown in Figure 41b. The leak rate of cis-2-butene in Figure 41a was constant throughout the run, i.e., the number of molecules of cis-2-butene entering the reaction cell per second was a constant. In Figure 41b, the leak rate of cis-2-butene was cut back and finally terminated in the early part of the run. The total amount of butane produced in both cases was about 3×10^{11} molecules (partial pressure of butane $\sim 1 \times 10^{-8}$ torr in reaction volume of ~1 liter). After the maximum amount of butane was produced, the metal surface was completely dead for further self-hydrogenation. The reaction mixture was pumped away by opening the valve to the pumps; the valve was closed again and the buildup of masses 41 and 43 was observed. No mass 43 was observed.

In both cases, an induction period was noted before butane appeared in the gas phase. The induction period can be interpreted in several ways as will be seen in the discussion section to follow. It is important to realize at this point what factors are involved in observing a gas phase hydrocarbon pressure. The leak rate of hydrocarbon into the cell in room temperature experiments is at least partially counterbalanced by pumping through the shut ground glass valve, as well as by the clean tungsten wire and mass spectrometer

filament. The first effect is observed to be small in the 10^{-7}-10^{-8} torr range from Figures 41,42. In the self-hydrogenation and hydrogenation experiments summarized in those figures, the ultimate pressure of butane produced was nearly constant once achieved.

Pumping by the clean metal wire, on the other hand, can be quite extensive. For example, Jenkins and Rideal, using nickel films and ethylene pressures in the torr range observed that all olefin admitted to their reaction flask was "pumped" by the metal film up to about the equivalent of one-quarter of an ethylene monolayer (48). Only then did ethylene appear in the gas phase. Estimating hydrocarbon surface coverages from gas phase hydrocarbon pressures is thus seen to be a highly tenous proposition.

In this study two tacks were used to eliminate the uncertainty surrounding surface hydrocarbon coverages. First, after deliberately contaminating the filament by heating a monolayer dose of cis-2-butene to 1000°K, the variable leak dial setting required for gas phase hydrocarbon appearance was noted. The setting was found to be highly reproducible with care. This procedure established the time zero when hydrocarbon admission into the reaction cell could have been detected. Secondly, coverage experiments at a given valve setting helped to establish the settings required to obtain a given hydrocarbon ambient pressure. The pressure was then

estimated from the time required for monolayer formation. The definition of what constitutes a monolayer of hydrocarbon is somewhat ambiguous. For the purposes of these studies, dosing intervals at a given pressure were increased until the amount of hydrogen in flash decomposition experiments did not appear to change. This pressure was cross-checked with pressure calibrations via the ion gauge and mass spectrometer. In general, the two agreed within a factor of 2-5.

Hydrogenation of cis-2-butene at 300°K

Hydrogenation experiments were equivalent to self-hydrogenation in all respects except that after cleaning the filament and cooling to room temperature, a hydrogen partial pressure of 1×10^{-6} torr (gauge) was established. Cis-2-butene admission was begun, and butene and butane ion currents were recorded. A typical room temperature hydrogenation result is shown in Figure 42. In this case, there is no induction period before butane is observed in the gas phase. In fact, initial butane partial pressures are slightly higher than butene partial pressures. The log of butane pressures is seen to be nearly constant up to about 50 seconds, where butane production begins to tail off, becoming zero at about 90 seconds. The surface was inactive for further hydrogenation at this point.

The maximum amount of butane produced in hydrogenation experiments was a factor of ten greater than for self-hydrogenation experiments, $\sim 3 \times 10^{12}$ molecules.

Decomposition experiments

Hydrogen Results typical of monolayer hydrogen coverages at 95°K are shown in Figure 43. Five different desorption forms of hydrogen were always obtained from clean tungsten surfaces. The ordinate values in Figure 43 are normalized to facilitate comparison of data by plotting $P(T_i)/P_{max}$.

In Figure 44 a superposition of experimental data shows the effect of coverage on hydrogen desorption spectra. The voltage drop across the filament is shown as a function of time along with mass 2 ion current. Temperatures at various points in the decomposition curve, taken from the voltage drop curve, are shown in the bottom x-axis. (Note that temperature is not linear with time on the plot.) The experimental data presented in the immediately preceding figure are shown in curve A. All 5 forms of hydrogen are present for monolayer coverages. With decreasing adsorption time at a given pressure, the first four forms of hydrogen decrease in amount relative to the highest temperature form. This is shown in curve B. With even lower hydrogen coverages, only the high temperature, β_2, form is detected.

Hydrocarbon decomposition Normalized decomposition plots for mono-layer coverages of the C_1 through C_4 hydrocarbons

studied in the initial decomposition experiments are shown in Figures 45-49.

C_1 and C_2 hydrocarbons Normalized hydrogen decomposition spectra for methane, ethane, ethylene and acetylene are shown in Figure 45. Ethylene yields two well-resolved peaks, with peak maxima at ~300°K and 430°K. The first peak was always smaller than the second. This is due in part to the type of heating rate employed which increased with increasing time (and temperature). As a result, temperatures were increasing at a faster rate throughout the second decomposition region than through the first. Initial production of hydrogen was noted at ~200°K in all experiments.

Acetylene yielded a single hydrogen peak at a reproducibly higher temperature than the second ethylene peak, ~475°K. Hydrogen production became appreciable at ~200°K and thereafter increased at a uniform rate up to the peak maximum. The amount of hydrogen in the acetylene peak, as judged by the peak height, was very nearly equivalent to the second ethylene peak.

The maximum rate of hydrogen production for methane and ethane was observed at ~600°K .* Methane appeared to consist

*In highly pumped systems, Redhead has shown that the peak maximum in a flash desorption spectrum corresponds to the maximum rate of desorption (113).

of a single decomposition peak, while ethane reproducibly yielded three hydrogen forms. The lower temperature hydrogen peaks, observed as shoulders on the major 600°K peak, match up well with the two olefin hydrogen peaks from ethylene.

C_3 hydrocarbons Normalized hydrogen decomposition spectra for the C_3 hydrocarbons studied are shown in Figure 46. Propylene yielded a multiple peak, with peak maximum at ~430°K. A shoulder on the propylene spectra indicated a non-resolved hydrogen peak at ~300°K. The amounts of hydrogen in the first and second peak were not determinable, but it appeared that the second peak contained much more hydrogen than the first.

Methyl acetylene yielded a single peak, the maximum rate of hydrogen desorption being at ~500°K.

Propane decomposition spectra were characterized by a poorly defined peak maximum extending over about 100 degrees from 400-500°K. A reproducible shoulder on the low temperature side of the central peak indicated a small hydrogen peak at about 300°K.

Allene (1,2-propadiene) yielded a single hydrogen peak at ~450°K.

Hydrogen production for all four C_3 hydrocarbons became appreciable at about 200°K.

C_4 hydrocarbons

Straight chain olefins Hydrogen decomposition spectra for the three straight chain olefins containing four carbon atoms are shown in Figure 47. Peak maxima for cis- and trans-2-butene and 1-butene occured at ~430°K. All three olefins yielded peak shoulders indicative of a lower temperature hydrogen peak superimposed on the much larger major peak.

All three olefins yielded low temperature hydrogen peaks between 100-150°K. 1-butene reproducibly gave two low temperature hydrogen peaks, one centered at ~120°K, the second at ~130°K.

Branch chain C_4 hydrocarbons Results for the two branch chain C_4 hydrocarbons, isobutylene and isobutane, are shown in normalized hydrogen decomposition spectra in Figure 48. Isobutylene gave similar results to the straight chain C_4 olefins seen in the immediately preceding figure, a low temperature peak and two higher temperature forms. The "300°K" peak for isobutylene appeared better resolved than for the straight chain olefins while the major peak again appeared at 430°K.

Isobutane spectra were much sharper than propane spectra. In fact, isobutane spectra almost duplicate the two higher temperature peaks observed for isobutylene. No low temperature hydrogen was observed for isobutane, but a high

temperature shoulder was detectable indicating a hydrogen peak at ~600°K.

Remaining C_4 hydrocarbons The remaining C_4 hydrocarbons initially studied were ethyl acetylene, n-butane and 1,3-butadiene. Their hydrogen decomposition spectra along with that of trans-2-butene for reference are shown in Figure 49. Ethyl acetylene yielded a low temperature peak at ~130°K and a single spread-out peak with maximum at ~500°K.

N-butane results paralleled those for propane in that a rather broad peak was observed that appeared to contain a 300°K peak, a 430°K peak and a higher temperature hydrogen peak.

1,3-butadiene gave a low temperature peak at about 125°K with peak maximum at ~475°K and a third high temperature peak.

Nature of the low temperature hydrogen peak

The extremely low temperature at which hydrogen was detected (120-140°K) for many of the hydrocarbons studied suggested that the material being desorbed was physically bonded to the metal surface (or on top of a chemisorbed hydrocarbon layer). The absence of low temperature peaks for materials with higher vapor pressures at 95°K (such as methane, ethane, and propane) also supported this notion. To check this point, the principle peak for the hydrocarbon in question was isolated rather than mass 2 and flash decomposition spectra run. For all but 1-butene, the results were rather conclusive that the low temperature hydrogen peak results from desorption

of physically adsorbed hydrocarbon, the hydrogen coming from the cracking of the hydrocarbon in the mass spectrometer. In the case of 1-butene, however, only the second low temperature peak (at 130°K) matched up with the principal peak in the cracking pattern of 1-butene. Both mass 41 (principal peak) and mass 56 flash decomposition spectra displayed a large peak at 130°K with a very small spike at 120°K. When hydrogen was pre-adsorbed and then 1-butene adsorption allowed to take place, the 120°K peak was gone. Only the 130°K peak remained which was clearly separable from the physisorbed hydrogen peak at slightly higher temperature. The cracking pattern of 1-butene contained only peaks expected from examination of the API cracking patterns given in Table 2.

Comparison of FFS decomposition results for similar hydrocarbons

The expected similarities within groups of hydrocarbons of similar chemical nature was observed. Thus ethylene, propylene and the straight chain C_4 olefins all appeared to yield two different forms of hydrogen, indicating surface species of these olefins were thermally stable to the same degree as the more extensively studied ethylene on tungsten (36,120). Two surface species appeared to be present, associatively adsorbed olefin below 200°K and a hydrogen deficient surface species in the temperature range $200 \leq T \leq 350$°K. No high temperature hydrogen peak was observed. Isobutylene has an isopropyl

group bonded to a methylene carbon atom, and was expected to yield a different hydrogen deficient species in the 200-350°K range. Instead, results with isobutylene and even more surprisingly, isobutane, indicated the hydrogen deficient surface species were thermally stable to the same degree as those obtained from ethylene.

Alkynes, as a group, displayed similar decomposition spectra. The maximum rate of decomposition of the associatively adsorbed alkynes were at higher temperatures than the second olefin decomposition peak. This implies that the associatively adsorbed olefin is more stable than the hydrogen deficient species from associatively adsorbed olefin decomposition. Only one type of alkyne surface species was detected. The fact that surface alkynes containing ethyl or methyl groups attached to the acetylenic carbon atoms acted similarly to acetylene again was surprising. It is probably worthwhile to reiterate that no hydrocarbon species were detected in the gas phase during decomposition experiments for any of the chemisorbed hydrocarbons.

The two diolefins studied, allene and 1,3-butadiene both yielded a single major peak (at the same temperature) indicating the associatively adsorbed surface species for the two compounds were equivalent in thermal stability. Here again, the simplicity of the decomposition spectra was surprising. Allene and 1,3-butadiene would seem likely candidates for allylic bonding. Both could also form a 1,3-di-adsorbed sigma bonded surface species. The thermal stabilities of the

di-olefins, associatively adsorbed on tungsten, were intermediate between the hydrogen deficient olefinic species and the associatively adsorbed alkyne.

Paraffins studied, as a group, behaved in similar fashion. All gave two recognizable peaks which could be attributed to olefinic type bonding to the surface with a third higher temperature peak that suggested alkyl radical type of bonding similar to that which methane must employ.

Effect of surface coverage on paraffin decomposition spectra

The effect of decreasing surface coverage on hydrogen desorption spectra for ethane, n-butane and iso-butane was investigated by decreasing the adsorption time at 95°K at a given dosing pressure. The results for n-butane are shown in Figure 50. Experimentally obtained tracings are shown with the relative dosing times indicated for each tracing. To separate the six tracings, each has been displaced vertically from its neighbor by an equal amount. The results are similar to those shown for hydrogen. Whereas for monolayer coverages (top curve), a structureless desorption peak is obtained, upon decreasing the adsorption interval the low temperature side of the peak diminishes, exposing a high temperature peak at about 595°K. This is the temperature range where the methane and ethane high temperature peaks were

obtained. The paraffin decomposition spectra appear to be broadened relative to olefin decomposition spectra due to the inclusion of a high temperature "cracking" peak. Similar results were obtained for ethane and isobutane.

DISCUSSION OF RESULTS

Field Ion Microscopy: Adsorption Occurs on All Planes

In the preceding three chapters experimental studies with a variety of C_1-C_4 hydrocarbons have been presented. Of the results previously discussed, those for field ion microscopy are perhaps the most straightforward. Ethylene and acetylene were found to adsorb on all planes exposed on field evaporated tungsten tips. Spacings exposed on the four prominent low index faces are:

{100}	-	3.16Å	4.5Å
{110}	2.7Å	3.16Å	-
{111}	-	-	4.5Å
{211}	2.7Å	-	4.5Å

Extensive adsorption of acetylene was observed on all but {100}.

Gardner has calculated the minimum strain-free tungsten-tungsten metal atom spacings for σ-diadsorbed-ethylene and acetylene using a hard sphere geometric model (36). Minimum spacings were found to be 3.39Å for acetylene and 2.94Å for ethylene. On the basis of these calculations and FEEM migration studies, Gardner proposed that acetylene adsorption would be preferred on 3.16Å spacings. In the current FIM study {100} planes, with a high site density of 3.16Å spacings, appeared to be less favorable for acetylene adsorption than

planes exposing no 3.16Å spacings such as {110} and {211}. Gardner's arguments concerning what constitutes suitable metal atom spacings pre-supposed 1,2-σ-diadsorbed species. π-bonding to an individual metal surface atom, however, would not depend upon specific metal-metal distances. Rather, the presence or absence of suitably oriented metal orbitals would be required. Since a great many investigators in catalysis have begun to invoke π-bonded surface moieties, a short look at π-bonding versus σ-bonding as a means to explain experimental observations will be presented.

Nature of Hydrocarbon-Metal Bond

The impetus for invoking π-bonded surface species on metal surfaces has been supplied by the existence of a large number of stable transition metal-hydrocarbon complexes with a variety of hydrocarbons. Olefin complexes have been extensively documented while some examples of alkyne complexes are known (7). Di-olefin chelating agents have been known for some time. Homogeneous catalysis of various hydrocarbon conversion processes by transition metal complexes, such as isomerization (106), exchange (37), and hydrogenation have been catalogued.

To investigate the feasibility of extending results for homogeneous systems to heterogeneous gas-solid processes, the FIM and FEEM observations already presented were compared with predictions based on a model for the spatial orientation

of metal orbitals. The particular model chosen involved generating the hybrid d-orbitals for a bulk phase b.c.c. atom. O_h symmetry is applicable which yields two sets of hybrid d-orbitals, a triply-degenerate t_{2g}, and a doubly degenerate, higher energy, e_g. These orbitals were then taken to be the orbitals emerging from surface metal atoms.

Such an approach is open to legitimate criticism. Orbitals generated for an octahedral environment in the bulk metal are alleged to exist at a metal surface where the highest symmetry possible is C_4. To avoid this criticism, only the symmetry of the surface plane in question could have been considered. An even better choice, symmetry-wise, might have been the choice of the local symmetry of the hydrocarbon-metal environment. As a justification of the approach used, it can be mentioned that such a tack has been utilized by other catalytic investigators with mixed success (7). In addition, variations in image intensity for hydrogen-promoted helium ion image have been rationalized with good results assuming directed-metal orbitals of the kind presented in this discussion (53).*

The e_g band at a {100} face is assumed to be sufficiently electron deficient for σ-bonding (Type 1); the t_{2g} band is assumed to be sufficiently filled for π-bonding (Type 2) (7).

---

* The e_g and t_{2g} orbitals were incorrectly located. See page 274 for correct assignment.

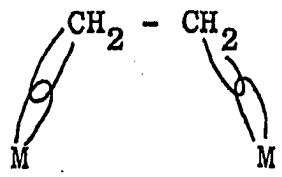

Type 1

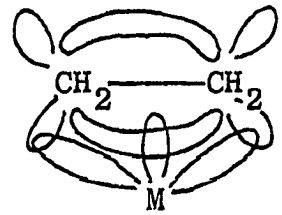

Type 2

Type 1 bonding involves overlap of SP^2-olefin orbitals with suitably directed metal e_g orbitals. Type 2 bonding to an individual metal surface atom involves overlap of a metal e_g orbital with the ethylene bonding p-π-molecular orbital with back bonding from metal t_{2g} orbitals to ethylene anti-bonding p-π-molecular orbitals.

No account will be taken in the present discussion of the change in symmetry at metal atoms on different crystal planes. The effect of considering this factor would be to remove the degeneracies within the e_g and t_{2g} subsets.

Bond, among others, has presented scaled-schematics of the e_g and t_{2g} orbitals emanating from f.c.c. surface atoms using this approach (7). Results for b.c.c. tungsten are equivalent in that, for a given surface atom on a particular plane with indices {hkl}, the spatial orientation of the metal orbitals will be the same. The spatial extension of b.c.c. tungsten orbitals will, of course, be different from that for f.c.c. nickel which Bond treated. Since atom arrangements are not equivalent for a given {hkl} plane in b.c.c. and f.c.c. systems, the relative orientation of metal

orbitals between metal surface atoms will also be different. Results for three low index faces on tungsten are given in Table 9.

Table 9. Orientation of e_g, and t_{2g} orbitals emerging from tungsten surface atoms on three low index faces

Plane	e_g	t_{2g}
{100}	one orbital perpendicular to the metal surface	four lobes of two of the three t_{2g} orbitals in dihedral planes at 45° to the metal surface
{110}	two lobes at 45° from the metal surface	one orbital perpendicular to plane of metal surface, five lobes of the three orbitals in dihedral planes at 30° to the metal surface
{111}	3 lobes at 36° to plane of metal surface	3 lobes in dihedral planes at 30° to the metal surface

Dihedral, in Table 9, refers to planes at 45° to the x, y, z axis which was arbitrarily chosen to be the axis along which the e_g orbitals were directed.

On {100} planes, coplanar metal orbitals in the sequence t_{2g}-e_g-t_{2g} are present to bond ethylene with the plane of the 4 hydrogens and 2 carbons parallel to the surface (Type 2). Type 1 bonding across 3.16Å spacings would not lead to good

overlap on {100} planes as the metal e_g orbitals emerge perpendicular to the metal surface.

On {110} planes, the arrangement of e_g and t_{2g} orbitals is reversed from that observed on {100} planes. Type 2 bonding would require the plane of the co-ordinate bond to be inclined at 45° to the metal surface. Type 1 bonding across 3.16Å spacings could lead to good overlap with ethylene SP^2 orbitals since the e_g orbitals emerge at 45° to the metal surface.

Type 2 bonding to a single metal atom does not appear possible on {111} planes. The required metal orbital combinations do not exist. Coplanar e_g-t_{2g}-e_g orbitals are available as noted by Bond (7). If the relative electron density in the e_g and t_{2g} metal orbitals were reversed on {111} planes versus {100} or {110}, Type 2 bonding could occur. Type 1 bonding. on the other hand, across the 4.5Å spacings should be possible, particularly if ethylene adsorbs in the trans-configuration predicted by Gardner (36).

Type 2 bonding or π-bonding as ordinarily invoked by workers in catalysis, cannot explain the FIM observations reported in this dissertation. Adsorption of acetylene and ethylene was observed on all low index planes whereas the simple model of π-bonding just presented would predict almost the reverse of the adsorption trends observed. 1,2-σ-diadsorbed species are, however, possible on all low index faces. The simplified model for metal surface orbitals in fact is

able to explain the relative lack of acetylene adsorption on {100} planes.

In general, simple models based on results for single metal atoms, as exist in transition metal complexes, should not be extended without reservation to structures of hydrocarbons on plane metal surfaces. For example, these studies have indicated that paraffins adsorb on tungsten surfaces to yield surface alkyl groups. The surface alkyl groups possessed the highest thermal stability of any of the surface species detected. Yet, the metal-carbon sigma-bond in gas phase compounds is known to be very weak as judged both by the lack of extensive examples of such species, and also on the basis of the stability of the few examples known (106). Generally, such compounds are stable only with co-ordinated unsaturated ligands able to donate electrons to the metal atom.

Metal surfaces, on the other hand, present a totally different situation. For one thing, the bulk metal may very well act as an electron source to stabilize surface alkyl radicals. The opportunity for the formation of surface species quite different from those in either bulk compounds or gas phase species should therefore be expected. Ehrlich has developed this concept in some detail and concludes that none of the currently used theories of bonding is applicable to metal surfaces (26). As is oftentimes the case for science in general, and almost always the case in surface

chemistry, experimental techniques provide data which demand extensions of previously held concepts, or development of new theories altogether. Since σ-bonding appears to better represent the data presented in this study, it will be most often used.

Comparison of FEEM and FFS Results

In Figure 51 normalized plots of FFS hydrogen decomposition spectra and FEEM work functions for cis-2-butene are compared. The FEEM drop in work function between 100-225°K is clearly due to evolution of physisorbed 2-butene as shown by the mass 41 peak (principal peak) of cis-2-butene. The maximum rate of desorption of physisorbed material is centered in the 100-225°K temperature interval. Physisorbed gas yields a positive $\Delta\Phi$ which, on its desorption, would result in a work function decrease.

The work function increase beginning at ~225°K is due to decomposition of associatively adsorbed olefin, putting hydrogen on the metal surface. Hydrogen has been noted as increasing the work function of tungsten emitters. Hydrogen evolution in FFS studies begins at ~200°K. This implies that hydrogen going to the surface in the decomposition step can find only a fraction of the sites necessary for bonding at temperatures above 200°K. This is readily explained by reference to Figure 44 which showed the dependence of hydrogen flash desorption traces from clean tungsten as a

function of hydrogen coverage. The implication of Figure 44 is that there are at least four different groups of metal sites suitable for chemisorption of hydrogen. The strongest, as judged by the temperature at which desorption occurs, is the so-called β_2-hydrogen site. β_2-sites fill preferentially until they are depleted, at which time β_1 sites are filled. The γ-states are filled only at near monolayer coverages.

Hydrocarbons also preferentially occupy the "stronger" sites at low coverages. This was demonstrated in unreported experiments in which ~0.1 monolayer of olefin was pre-adsorbed followed by hydrogen dosing. The β_2-hydrogen peak was completely missing while the two olefin hydrogen peaks and β_1-hydrogen peak were resolved in flash decomposition spectra. As a result, in hydrocarbon flash decomposition experiments hydrogen evolution occurs at essentially the same temperature at which decomposition occurs. This does not imply that hydrogen is liberated directly to the gas phase. On the contrary, FEEM Φ vs. T plots and self-hydrogenation experiments both indicate hydrogen is present on the metal surface.

FEEM evidence indicates a second surface reaction starting about 350°K (work function measurements and emission patterns). This second olefin decomposition reaction also involves hydrogen addition to the surface. A shoulder on the hydrogen flash desorption spectra announced the tailing-off of the first decomposition reaction and the onset of the second

reaction. The amount of hydrogen in the first peak was found to be substantially less than in the second desorption peak.

Cis-(and trans-)2-butene decomposition can be formulated then as;associative adsorption below 200°K.

$CH_3CH = CHCH_3(g)$ 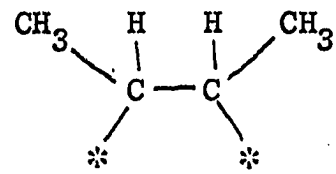

First decomposition reaction, 200-350°K

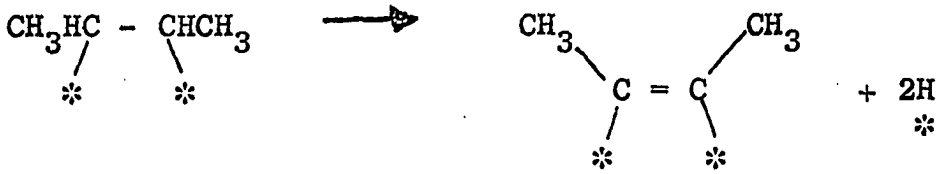

Second decompostion reaction, 350-500°K

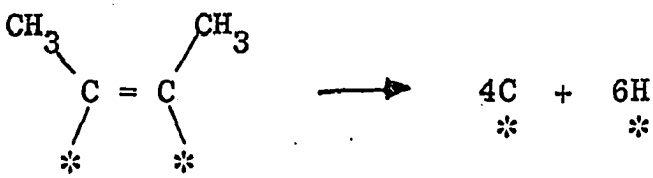

Hydrogen adsorption-desorption pseudo-equilibrium

$$2H^{*} \rightleftharpoons H_2(g)$$

The product of the first decomposition reaction has been written as an associatively adsorbed alkyne. This formulation clearly indicates the stoichiometry of the surface species. It will also be seen to agree with surface structures of catalytically active intermediates predicted by many experimenters.

Results for 1,3-butadiene can be treated in more straightforward fashion after a short discussion of hydrocarbon surface species postulated by other experimenters.

Classical Surface Species

Unsaturated hydrocarbons

The hydrocarbon surface species indicated by FEEM and FFS results are seemingly equivalent to those postulated by workers employing the kinetic approach (deuteration, exchange). This is highly interesting, since my studies were conducted on a clean tungsten surface, and much of the previous work to be described was carried out on supported metal catalysts. Thus it would appear that surface species occupying "strong" sites, as in my studies, are equivalent to the catalytic intermediates observed on contaminated surfaces. Reference has previously been made to the fact that many observors feel that such is not the case.

Burwell has given a scheme for interconversion of the C_4-hydrocarbons, indicating the surface species active in catalytic processes (20). This is shown in the following cycle of reactions for several unsaturated C_4 hydrocarbons.

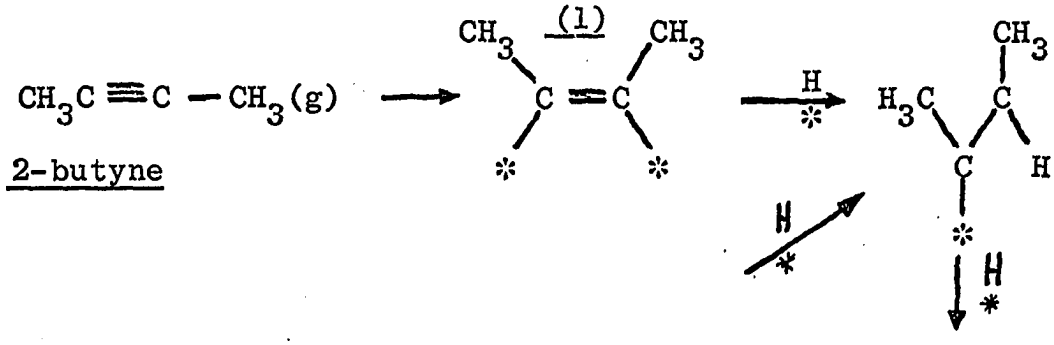

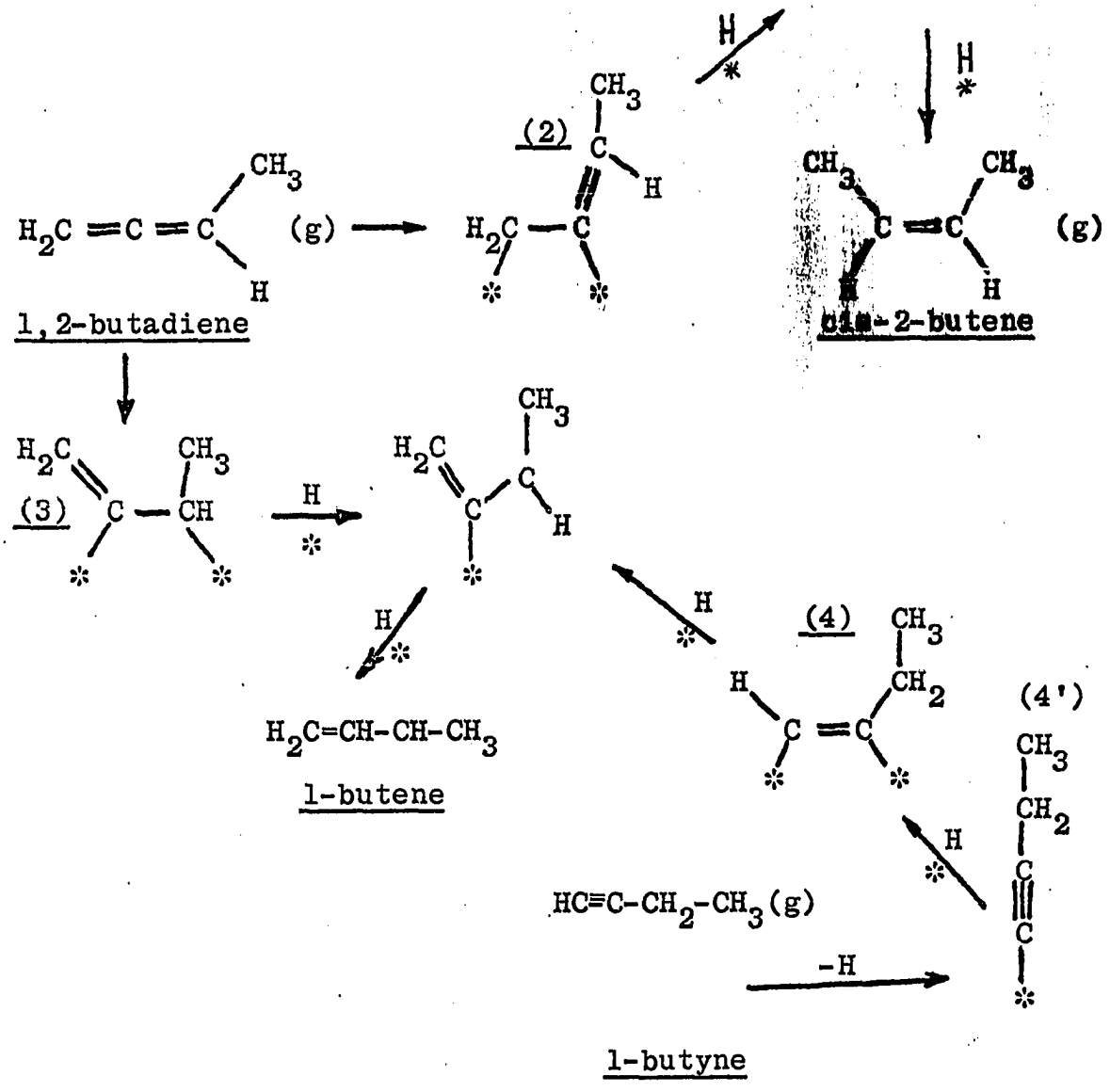

Other surface species judged possible by Burwell include (5) and (6).

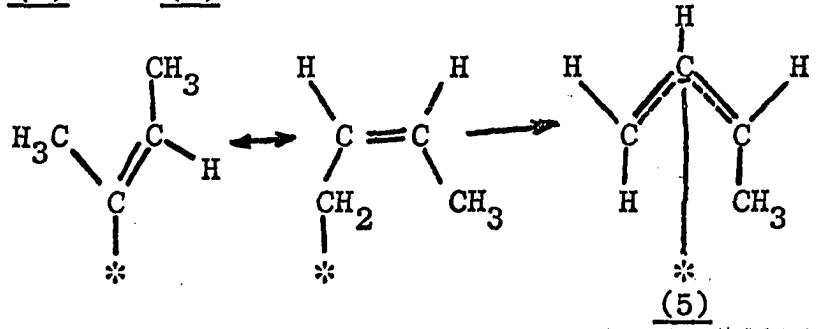

(5)

cis-π-allylic species

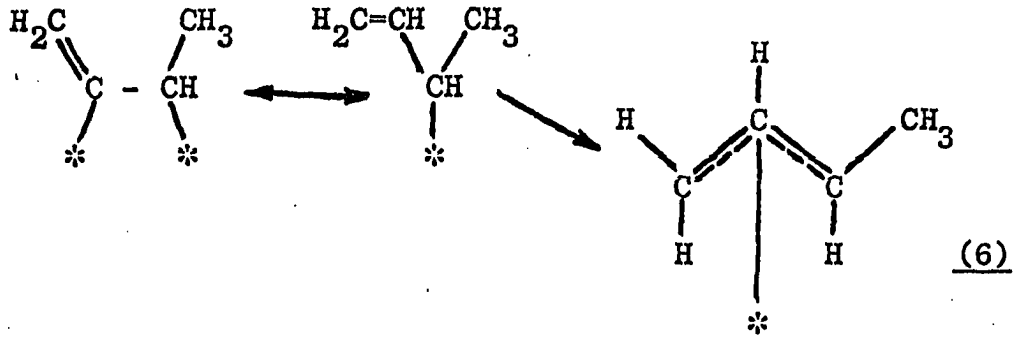

(6)

trans-π-allylic species

Whereas deuteration of 1-butyne and 1,2-butadiene form nearly exclusively 1-butene and cis-2-butene, 1,3-butadiene deuteration yielded 1-butene and trans-2-butene. Burwell concludes that structures such as:

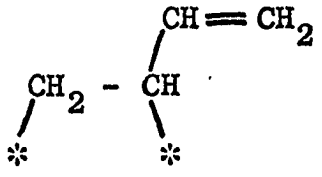

cannot represent the catalytically active adsorbed state of 1,3-butadiene. Formation of 4-σ bonds was also ruled unlikely. Instead, structure (7) was proposed.

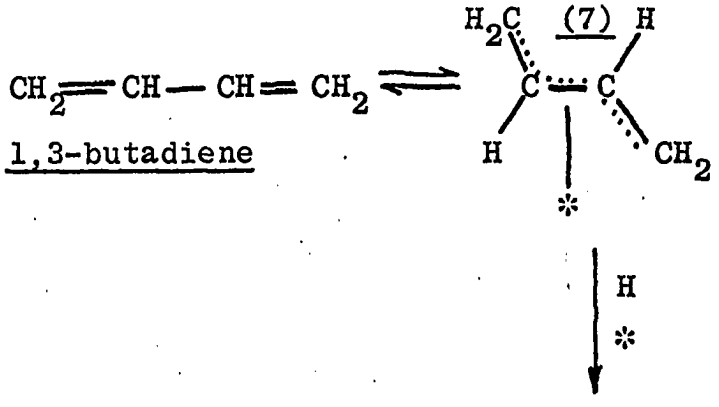

1,3-butadiene

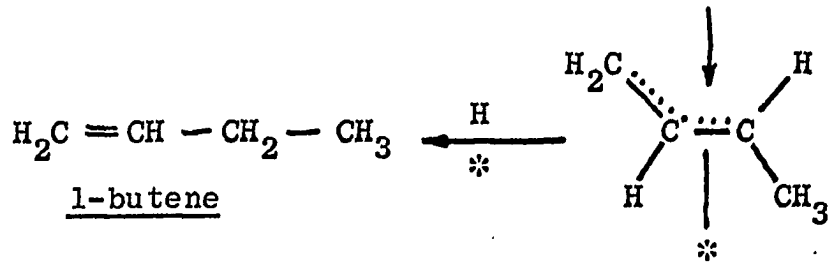

The plane of the 4 carbons in structure (7) is parallel to the metal surface.

The other di-olefin investigated in these studies, allene, has not been extensively studied. Burwell has suggested (8) and (9) to explain his deuteration experiments.

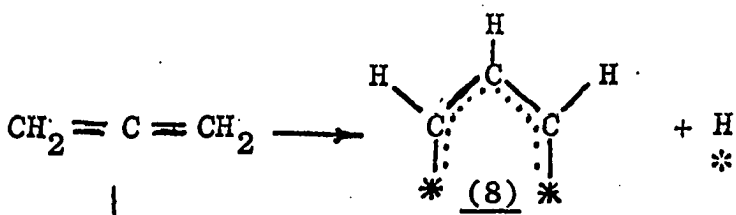

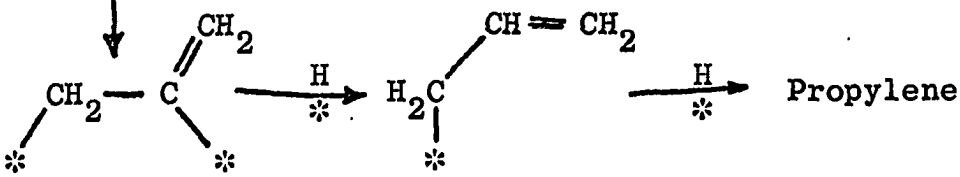

(9)

Mann agrees that structure (9) is likely and also notes the possibility of radical formation (structure 10) (57).

(10)

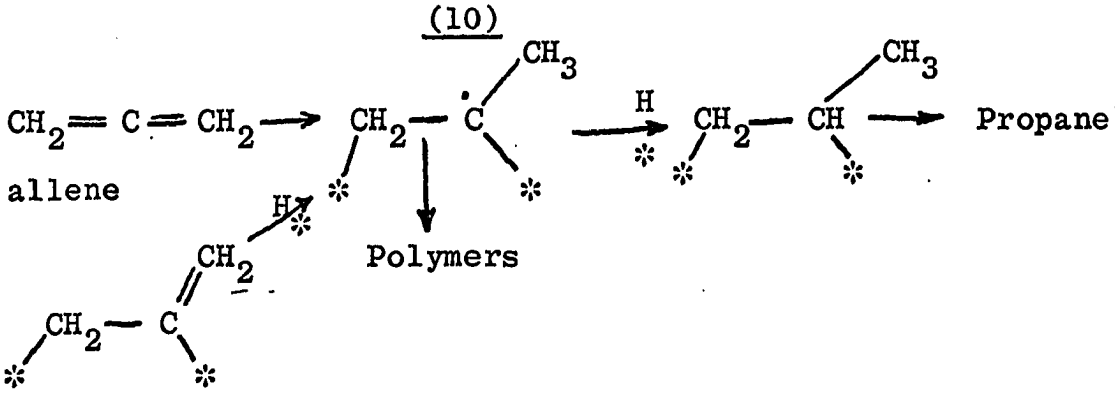

The same author notes that allene and methyl acetylene behave quite similarly which was interpreted as (99):

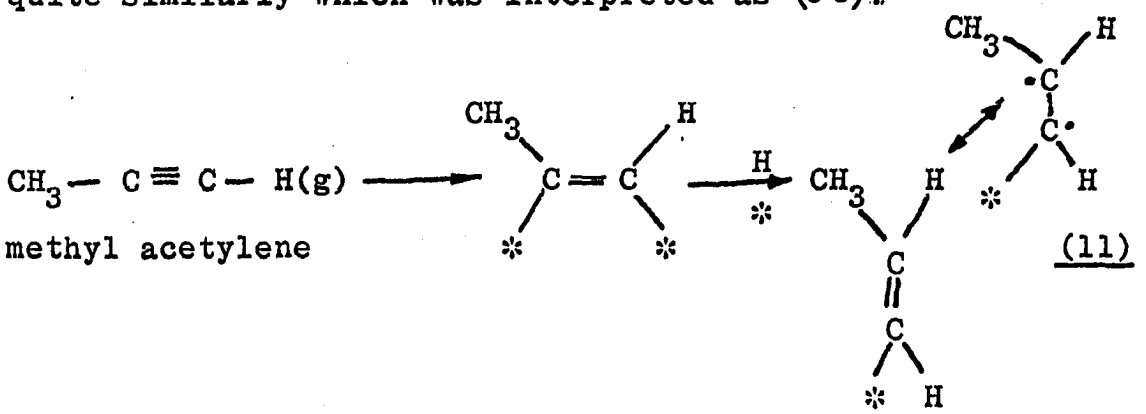

methyl acetylene (11)

Other C_2 and C_3 olefins and alkynes are observed to form surface structures similar to (1) through (11).

In Table 10, the olefins, di-olefins and alkynes studied by FFS and FEEM are listed along with the classically predicted surface structures.

Nearly all the observations made in my FEEM and FFS studies can be rationalized in terms of the catalytically active surface intermediates listed in Table 10. The similar thermal stabilities observed for similar groups of compounds is seen to be due to identical bonding to the surface. Four different metal-carbon bond geometries can be seen:

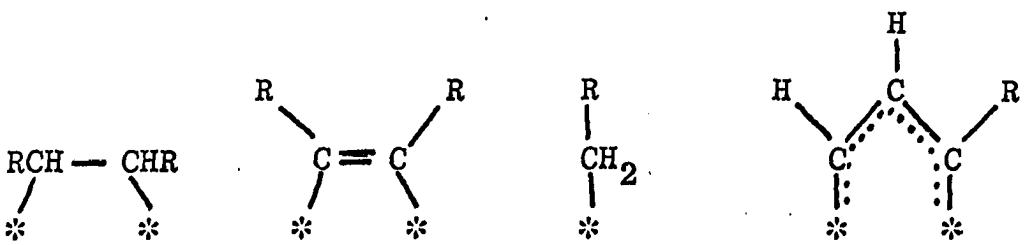

Olefins Alkynes Paraffins Allene, 1,3-butadiene

Table 10. Classical surface structures for selected C_2- C_4 hydrocarbons

Carbon #	Surface Species
C_2	Ethylene 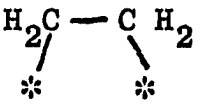 Acetylene 
C_3	Propylene 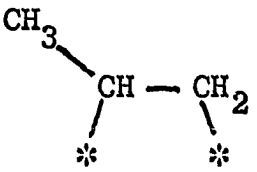 Methyl Acetylene 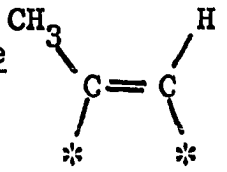
	Allene 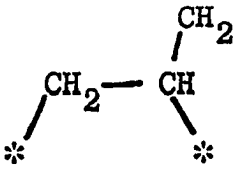 or 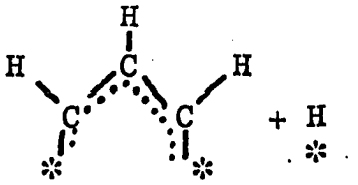
C_4	1-butene 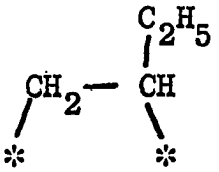 1-butyne 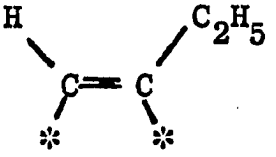
	cis-2-butene 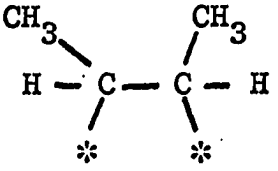 trans-2-butene 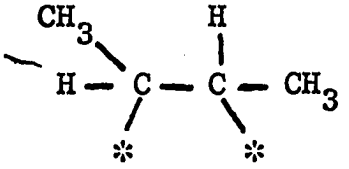
	1,3-butadiene 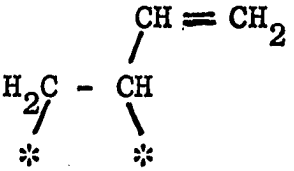 or 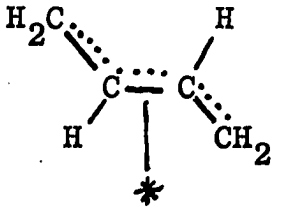

Table 10. (Continued)

Carbon #	Surface Species
	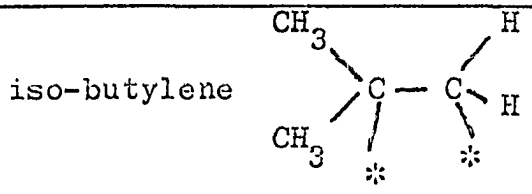
iso-butylene	

Within any one of the four groups similar thermal stabilities should be expected. Substituent groups attached to the carbons bonded to the metal surface should have only secondary effects so long as the rate limiting step in the decomposition process does not directly involve the side chain groups. Such does not appear to be the case for the sixteen hydrocarbons studied in this dissertation. This observation may be significant for formulating decomposition mechanisms, for example, of the 2-butenes. The hydrogen deficient species after the first decomposition reaction is alleged to be a sym-dimethyl acetylene surface species. The rate limiting step in the alkyne decomposition may very well be rupture of the C-C bond for the two carbons bonded to the metal surface.

The two di-olefins studied, allene and 1,3-butadiene, are particularly interesting. Their thermal stabilities were nearly quivalent. Moreover, a surface reaction was observed in FEEM studies between 100-200°K for 1,3-butadiene while no gas phase products were detected by FFS experiments. The maximum in the φ vs. T plot at ~150°K for 1,3-butadiene

results from two surface processes occurring at the same time. Desorption of physisorbed gas would result in a work function lowering as observed for cis- and trans-2-butene. Occurring along with desorption of physisorbed 1,3-butadiene is a surface reaction which leads to a work function rise. Reference to structures proposed for allene and 1,3-butadiene in Table 10 yields a clue as to the nature of this second surface reaction. One of the structures proposed for allene is:

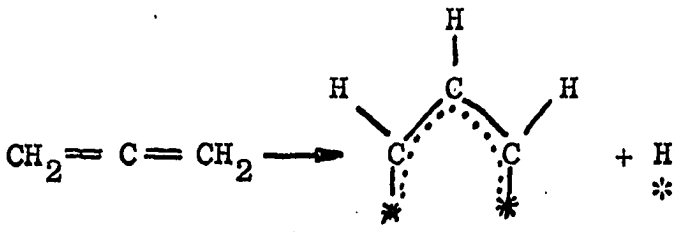

The presence of hydrogen on the metal surface would lead to a work function rise. The analogous structure for 1,3-butadiene would be:

(12)

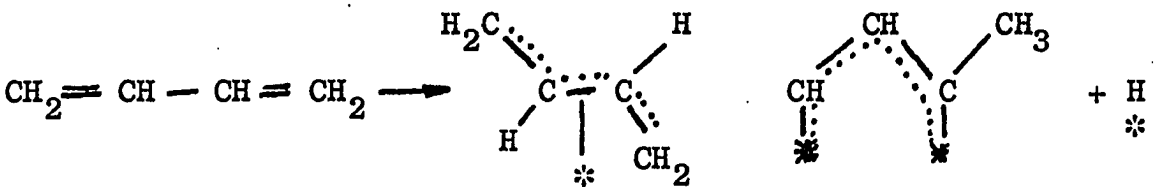

The surface intermediates (9) and (10), which could form polymers were observed indirectly in my FFS experiments. When conducting experiments on allene and methyl acetylene some difficulty was encountered in cleaning the tungsten wire. The initial explanation for this phenomenon assumed the difficulty was due to impurities in the technical grade gases

used. It is possible, however, that surface polymers were formed which were more refractory than the carbon residues produced with most other hydrocarbons studied.

Paraffins Paraffin adsorption and reactions have been extensively studied relative to studies with unsaturated hydrocarbons. This is due principally to the relative inactivity of paraffins and resulting simplicity in paraffin reactions. Two general types of studies of interest to the present discussion are commonly conducted to investigate paraffin reactions with metal surfaces. By studying gas phase methane and ethane compositions over metal films as a function of time, Ashmore et al. concluded that the surface species for methane was a $\overset{*}{C}H_3$ moiety (3). Ethane, however, was postulated to form both surface ethyl groups and associatively adsorbed ethylene on tungsten, iron and nickel films. The rate of paraffin adsorption was greatest on tungsten as was the total amount adsorbable.

The conclusions of Ashmore are clearly substantiated in the present FFS work. Methane decomposition yielded only a single hydrogen peak at higher temperatures than for any other class of hydrocarbons. The single peak was also quite narrow, again relative to other types of hydrocarbons. Ethane decomposition yielded all three hydrogen peaks required for the presence of associatively adsorbed ethylene and surface

alkyl groups. From the hydrogen peak shapes, the amount of associatively adsorbed ethylene was an order of magnitude less than the amount of surface alkyl groups.

Ashmore, et al., concluded that methane decomposition proceeded by stages from CH_3* to CH_2* to CH* and finally to C*. From the narrow peak width observed in the present studies, it would appear that the rate limiting step in the decomposition of methyl radicals, and by analogy for other paraffin radicals, was the removal of the first hydrogen to form $\overset{*}{C}H_2$. The methylene-like surface group is apparently unstable and breaks down rapidly to carbon and hydrogen. If the intermediate CH* species is formed, it is only a transient species.

The observations of Engel et al., for the same two hydrocarbons on UHV deposited chromium films gives further clues to the nature of paraffin surface reactions (31). For both methane and ethane, only ~0.14 paraffin molecules adsorbed for every chromium surface atom. Thus only about 1/4-1/2 of the total number of surface sites available to ethylene are able to break C-H bonds to permit paraffin adsorption. The same authors make the interesting observation that the gas phase decomposition products for methane and ethane depend on the carbide-forming capabilities of the metal film employed. Body-centered-cubic Cr, W, Mo, V and Fe, which form carbides, yield hydrogen as the major decomposition

product. F.c.c. metals Rh and Ir yield mostly methane. The f.c.c. metals form only solid solutions of carbon. This observation clearly indicates that the strength of the metal-carbon bond plays an important part in the reaction of paraffins and also for all hydrocarbon reactions.

Examination of the deuterium distribution in exchanged-paraffins is the second general method applicable to paraffin surface reaction studies. Kemball notes that the ease of exchange for a series of selected paraffins goes (50)

$$\text{cyclo-}C_6 \simeq C_2H_6 \simeq C_4H_{10} > C_3H_8 > C_2H_8 \geq CH_4.$$

The number of deuteriums substituted, and their location, also provides information about the interconversion process just described. Kemball notes that the strongest bond formers (i.e., the b.c.c. metals) yield mostly di-substituted products in the initial stages of the reaction. The other major initial product is d-max. Weak bond forming-metals, on the other hand usually give the whole spectrum of deuterated products, d_1- through d_{max}.

d_1-substituted paraffins in initial reaction stages on tungsten apparently result from interaction of two alkyl surface groups.

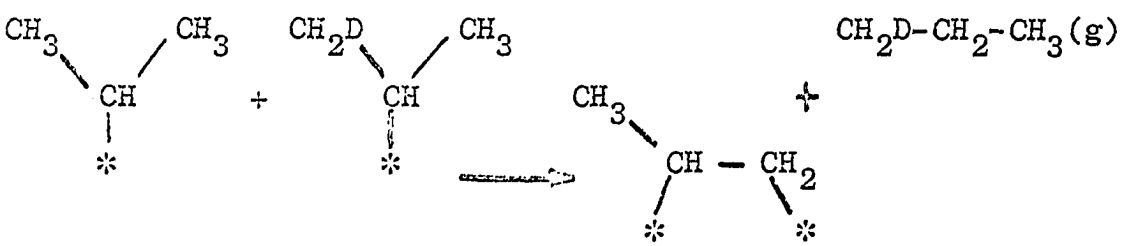

This type of reaction is clearly indicated in my coverage experiments with ethane, iso-butane and n-butane. At low surface coverages only the hydrogen decomposition peak indicative of surface alkyl groups is observed. At higher coverages, the lower temperature hydrogen forms from associatively adsorbed olefin begin to appear.

The low surface coverages indicated for paraffin adsorption, coupled with the near absence for ethylene of olefin hydrogen decomposition peaks, could indicate that the reaction of ethyl radicals to form associatively adsorbed ethylene is slow compared to the reverse step. For propane and n-butane, however, the amount of surface olefine relative to surface alkyl group was higher. It is possible that the experimental findings reported in this study cannot be used to estimate relative rates of surface reactions applicable to hydrogenation. The simple dehydrogenation reaction of surface ethyl groups converting to associatively adsorbed ethylene is complicated by the alkyl disproportionation reaction. The latter reaction, in turn, is dependent on the coverage and chemical identity of the alkyl groups.

My FFS results for iso-butane differ markedly from the normal-paraffins studied. The hydrogen decomposition spectra for iso-butane was nearly equivalent to that for iso-butylene. Only a small high temperature shoulder on the two olefin hydrogen peaks was observed for iso-butane. This indicates

mostly a surface olefin species for iso-butane. This is readily explained by the interaction of two surface iso-butyl groups to form gaseous iso-butane and adsorbed olefin. The impetus for a more extensive disproportionation in the case of iso-butane lies in the presence of a tertiary carbon atom. The activation energy for adsorption of iso-butane should be lower than, for example, for n-butane due to the labile hydrogen present on the iso-butane gas molecule. More extensive iso-butane adsorption relative to other paraffins studied should be the result, which would enhance the surface alkyl disproportionation reaction. Numerous references to the relatively higher reactivity of hydrogens attached to tertiary carbon atoms can be found. For example, in exchange studies, Kemball found that the relative exchange rate at tertiary carbon atoms was ninety times that at primary carbon atoms (50).

Nature of "Weak", "Strong" Sites

The implications of similar studies on supported metal catalysts versus clean metal surfaces are that metal sites on the two types of surfaces are different. Experimenters employing supported metal surfaces often suggest that catalytic processes occur on only a fraction of the available metal sites. Only "weak" sites are alleged to be involved in production of products. Clean metal surfaces, on the other hand, are supposed to possess largely "strong" sites. An operational definition of what constitutes weak versus strong sites is

difficult to formulate. Perhaps most useful is the concept of the relative temperature required to affect the same conversion process. A metal surface possessing large numbers of strong sites will be active at lower temperatures than another surface with weak sites.

The nature of weak and strong sites, however, seems more clear from the present studies. The presence of an adsorbed species has been noted, from FIM observations previously discussed, to affect markedly the strength of metal-metal bonds. This was reflected, for example, in hydrogen-promoted field evaporation and field induced corrosion of emitter surfaces by water, nitrogen and hydrocarbon. Chemisorption of a single molecule leads to substantial rearrangement of charge in the metal substrate around the ad-species. This leads to potentially weaker adsorption sites in the vicinity of an adsorbed species such as a hydrocarbon surface species. Weak and strong sites are thus functions of the number, and chemical nature, of adsorbed species.

The allegation has been made in this report that surface species indicated by FEEM and FFS studies on strong sites are equivalent to those postulated from studies on supported catalysts. In large measure, higher temperatures are required for supported metal surfaces than for clean metal surfaces to cause the same reaction because of adsorbed contaminant species. Such surface species as alkyne-like residues, carbon, carbides

or oxygen not only reduce the available surface for a given reaction, they also reduce the density of higher activity sites. Higher temperature operation serves several purposes. Contaminant species may be desorbed, or, alternatively, reactant molecules may be able to compete more effectively for surface metal sites. Secondly, the weaker sites may become able to cause adsorption of reactants and conversion of adsorbed reactants to products. The two effects are interrelated in that higher temperatures may weaken metal-contaminant bonding making desorption or displacement more likely; or, weakened metal-contaminant bonds may regenerate strong metal sites in the vicinity of a contaminant atom.

A certain amount of contamination by degradation products of the hydrocarbon conversion process under consideration is probably required on a commercial catalyst. Results on clean tungsten surfaces clearly indicate that chemisorbed species are not desorbed before decomposing. The result of this effect for olefin hydrogenation at room temperature is that the surface is rapidly poisoned.

Hydrogenation and Self-Hydrogenation of Cis-2-butene

Cis-2-butene self-hydrogenation on a clean tungsten wire at 300°K yielded ~1×10^{11} molecules of butane. Using a value of 4 metal sites per adsorbed butene, this amount of butane corresponds to about .001 monolayer equivalents of cis-2-butene. Hydrogenation in a 10^{-6} torr hydrogen ambient

yielded a factor of ten more butane or about 1/100 of a monolayer equivalent of cis-2-butene.

2-butene hydrogenation is much slower than ethylene hydrogenation. Using the same experimental system, Rye observed about a factor of ten more ethane produced in both hydrogenation and self-hydrogenation than was found for comparable experiments with cis-2-butene (120). The difference is clearly due to overall rates of hydrogenation of the two olefins from equivalent hydrogenation experiments. Rye observed only ethane in the gas phase in the initial portions of his experiments. Only after about 1×10^{12} molecules of ethane had been produced was ethylene observed in the gas phase. Cis-2-butene was observed in the gas phase at the initial stages of my hydrogenation experiments in amounts comparable to butane. This indicates that both adsorption and hydrogenation of cis-2-butene are much slower than comparable reactions for ethylene. This is not surprising since the presence of the two methyl groups on the butene can easily be envisaged to hinder adsorption sterically.

The decomposition of associatively adsorbed 2-butene is seen to markedly affect the total amount of butane produced. Many monolayer-equivalents of cis-2-butene struck the metal surface, yet only 1/100 of a monolayer equivalent of butane was produced in hydrogenation studies. After the maximum amount of butane was produced, the tungsten surface

was completely dead for further hydrogenation. Alkyne-like degradation products completely cover the surface and cannot be re-hydrogenated under the conditions available in the FFS reaction cell ($\sim 10^{-6}$ torr hydrogen).

The purpose of my research was not to study olefin hydrogenation. About one-half dozen experiments with cis-2-butene were run to check ideas about surface species indicated by flash decomposition experiments. I will therefore not attempt a lengthy discussion of hydrogenation results. Rye has extensively developed a model for olefin hydrogenation based upon reaction of chemisorbed olefin with mobile hydrogen adatoms (120). The resulting Langmiur-Hinshelwood type model can equally well be used to explain cis-2-butene hydrogenation.

Suggestions for Future Extensions of Results Obtained

FIM:

1) The use of imaging gases other than helium may be able to overcome the field decomposition reaction observed with helium ion microscopy. Neon appears marginal and would require the use of an image intensifier. Use of hydrogen would preclude subsequent work function measurements but might possibly be able to image intact hydrocarbon layers. Hydrogen-promoted-helium ion microscopy appears to have the best chance of performing the same function.

FEEM:

1) Single crystal face studies of hydrocarbon adsorption and reaction would provide the first valid test of the geometrical factor in hydrocarbon conversion reactions.

2) Migration studies of simple olefins across tungsten tips from different directions may support the tentative conclusions drawn in this report from comparison of ethylene and cis-2-butene migration data. Different migration directions may encounter different potential barriers to migration. The implications of such studies would lead to indirect evidence concerning the nature of hydrocarbon bonding to metal surfaces.

3) Allene decomposition studies would be interesting to see if a surface reaction occurred between 100-200°K as predicted for 1,3-butadiene.

FFS:

1) Decomposition mechanisms have not been considered in the present treatment. Three compounds would provide test cases for possible decomposition modes. If cyclopropane is to bond by a two point attachment, the resulting surface structure would of necessity be a 1,3-diadsorbed species. The flash decomposition spectra of cyclopropane would then yield a "fingerprint" of a 1,3-diadsorbed species. To guard against the possibility of carbene liberation, dimethyl cyclopropane should also be run. The gas phase methylcarbene which might form rearranges rapidly to ethylene.

Tetramethyl ethylene (2,3-dimethyl-2-butene) provides a surface olefin species with no hydrogen attached to the carbons bonded to the metal surface. Likewise, neo-pentane is a paraffin with only methyl groups exposed. These compounds would test the ability of the flash decomposition technique in differentiating different surface species. If significantly different, or if characterizable, results are obtained, decomposition mechanisms can be formulated. Suitably deuterated hydrocarbons may also be useful. For example, iso-butylene-1,1-d_2 or 1,3-butadiene-1,1-d_2 could be tested to check currently held concepts on surface structures.

2) Single crystal FFS experiments, perhaps coupled with contact potential difference measurements, would provide another means of evaluating geometric factors in catalysis.

3) No explanation of the multiple low temperature desorption at ~130°K for 1-butene has been offered. 1-pentene and 1-hexene decomposition spectra would indicate whether the phenomenon is related to the olefin double bond location.

Other experiments

Experiments with tungsten should be continued, but should be supplemented with similar studies on different metals. Metals suitable for both FEEM and FFS experiments which have not yet been utilized in studies by our research group include ruthenium and rhenium. Both are h.c.p. metals with boiling points above 2500°K. Ruthenium forms only a solid

solution of carbon in a fashion similar to iridium. Rhenium carbide forms, but decomposes to carbon and a saturated solution of carbon-rhenium at ~1900°K.

BIBLIOGRAPHY

1. Arthur, J. R. J. Phys. Chem. Solids 25: 583. 1964.

2. Arthur, J. R., Hansen, R. S. Ann. N.Y. Acad. Sci. 101: 756. 1963.

3. Ashmore, P. G., Kemball, C., Wright, P. G. Trans. Faraday Soc. 54: 1692. 1958.

4. Attardo, M. J., Galligan, J. M. J. Sci. Instr. 43: 607. 1966.

5. Bassett, D. W. Brit. J. Appl. Phys. 18: 1753. 1967.

6. Bassett, D. W. Nature 198: 568. 1963.

7. Bond, G. C. Disc. Faraday Soc. 41: 200. 1966.

8. Bowkett, K. M., Ralph, B. J. Sci. Instr. 43: 703. 1966.

9. Boyes, E. D., Elvin, C. D. J. Sci. Instr. 44:233. 1967.

10. Brandon, D. G. Brit. J. Appl. Phys. 14: 474. 1963.

11. Brandon, D. G. J. Sci. Instr. 41: 373. 1964.

12. Brandon, D. G. J. Sci. Instr. 43: 708. 1966.

13. Brandon, D. G. Phil. Mag. 7: 1003. 1962.

14. Brandon, D. G. Surface Sci. 3: 6. 1964.

15. Brandon, D. G., Perry, A. J. Phil. Mag. 16: 131. 1967.

16. Brandon, D. G., Ranganathan, S., Whitmell, D. S. Brit. J. Appl. Phys. 15: 56. 1964.

17. Brennan, D. Rec. Progr. Surface Sci. 2: 57. 1964.

18. Brenner, S. Surface Sci. 2: 496. 1964.

19. Burwell, R. L., Meyer, E. F. Ann. Rev. Phys. Chem. 15: 131. 1964.

20. Burwell, R. L., Meyer, E. F. J. Am. Chem. Soc. 85: 2881. 1963.

21. Condon, J. B. Field emission and flash filament studies of hydrogenation and dehydrogenation of cyclohexane and benzene on a tungsten surface. Unpublished Ph.D. thesis. Ames, Iowa. Library, Iowa State University of Science and Technology. 1968.

22. Cottrell, A. H. J. Inst. Metals 90: 450. 1962.

23. Drechsler, M. Z. angew. Phys. 13: 445. 1961.

24. Drechsler, M., Wolf, P. Int. Congr. Electron Microsc., 4th, Berlin, 1: 836. 1960.

25. Ehrlich, G. Adv. Catalysis 14: 255. 1963.

26. Ehrlich, G. Brit. J. Appl. Phys. 15: 349. 1964.

27. Ehrlich, G. Disc. Faraday Soc. 41: 7. 1966.

28. Ehrlich, G. J. Chem. Phys. 34: 29. 1961.

29. Ehrlich, G. Hudda, F. G. J. Chem. Phys. 36: 3233. 1962.

30. Ehrlich, G., Hudda, F. G. J. Chem. Phys. 44: 1039. 1966.

31. Engel, T. W., McElligott, P. E., Roberts, R. W. J. Chem. Phys. 47: 1537. 1967.

32. Farkas, A., Farkas, L. J. Am. Chem. Soc. 60: 22. 1938.

33. Feldman, U., Gomer, R. J. Appl. Phys. 37: 2380. 1966.

34. Fowler, R. H., Nordheim, L. Proc. Roy. Soc.(London) A119: 173. 1928.

35. French, R. D., Richman, M. H. U.S. At. Ener. Comm. AD-637, 743 [Defense Documentation Center, Arlington, Va.]. 1966.

36. Gardner, N. C. A study of the surface reactions of hydrocarbons on tungsten by field electron emission microscophy. Unpublished Ph.D. thesis. Ames, Iowa, Library, Iowa State University of Science and Technology. 1966.

37. Garnett, J. T., Sollich-Baumgartner, W. A. Adv. Catalysis 16: 95. 1966.

38. Gavriliuk, V. M., Medvedev, V. K. Soviet Phys.-Tech. Phys. 11: 1282. 1967.

39. George, T. H., Stier, P. M. J. Chem. Phys. 37: 1937. 1962.

40. Gomer, R. Australian J. Phys. 13: 391. 1959.

41. Gomer, R. Field emission and field ionization. Cambridge, Massachusetts, Harvard University Press. 1961.

42. Gretz, R. D. Rev. Sci. Instr. 38: 112. 1967.

43. Hanle, W., Rau, K. H. Z. Physik 133: 297. 1952.

44. Hiske, J. R. Phys. Rev. 122: 1207. 1961.

45. Holscher, A. A., Sachtler, W. M. H. Disc. Faraday Soc. 41: 29. 1966.

46. Horiuti, J., Ogden, G., Polanyi, M. Trans. Faraday Soc. 30: 663. 1934.

47. Hren, J. J., Newman, R. W. Rev. Sci. Instr. 38: 869. 1967.

48. Jenkins, G. I., Rideal, E. K. J. Chem. Soc. A1955: 2496. 1955.

49. Johari, O., Buchanan, W. Trans. Met. Soc. AIME 236: 1760. 1966.

50. Kemball, C. Adv. Catalysis 11: 228. 1959.

51. Klein, R. J. Chem. Phys. 22: 1406. 1954.

52. Klipping, G., Vanselow, R. Z. physik. Chem.(Frankfurt) 52: 195. 1967.

53. Knor, Z., Mueller, E. W. Surface Sci. 10: 21. 1968.

54. Lanczos, C. Z. Physkik 68: 204. 1963.

55. Little, L. H. Infrared spectra of adsorbed species. New York, New York, Academic Press, Inc. 1966.

56. Machlin, E. S. Am. Soc. Testing Mat. Quart. 60: 260. 1967.

57. Mann, R. S., To, D. E. Can. J. Chem. 46: 161. 1968.

58. McGee, J. D. Rept. Progr. Phys. 24: 167. 1963.

59. McLane, S. B., Mueller, E. W. U.S. Off. Naval Res.-Phys. Branch NP-12, 485. 1962.

60. McLane, S. B., Mueller, E. W., Nishikawa, O. Rev. Sci. Instr. 35: 1297. 1964.

61. Melmed, A. J. J. Appl. Phys. 38: 1885. 1967.

62. Melmed, A. J. Surface Sci. 7: 478. 1967.

63. Melmed, A. J. Surface Sci. 8: 191. 1967.

64. Melmed, A. J., Klein, R. J. Less Common Metals 10: 225. 1966.

65. Montagu-Pollack, H. M., Rhodin, T. N. J. Sci. Instr. 43: 667. 1966.

66. Moore, A. J. W. J. Phys. Chem. Solids 23: 907. 1962.

67. Moore, A. J. W. Phil. Mag. 16: 739. 1967.

68. Moore, A. J. W., Ranganathan, S. Phil. Mag. 16: 723. 1967.

69. Moore, C. E. Atomic energy levels as derived from analysis of optical spectra. U.S. Govt. Print. Off. Circ. 467, 3: 34. 1958.

70. Mueller, E. W. Adv. Electron. Electron Phys. 13:83. 1960.

71. Mueller, E. W. Am. Soc. Testing Mat., Spec. Tech. Publ. 340: 80. 1962.

72. Mueller, E. W. Ann. N.Y. Acad. Sci. 101: 585. 1963.

73. Mueller, E. W. AFOSR-1910 [Air Force Office of Scientific Research, Washington, D.C.]. 1961.

74. Mueller, E. W. Defense Documentation Center WADD-TR-60-535 [Wright Air Development Division Materials Laboratory, Wright-Patterson Air Force Base, Ohio]. 1960.

75. Mueller, E. W. Direction observation of crystal imperfections by field ion microscopy. In Newkirk, V. B., Vernick, J. B. eds. Direct observations of imperfections in crystals. P. 77. New York, New York, Interscience Publishers, Inc. 1962.

76. Mueller, E. W. J. Appl. Phys. 28: 1. 1957.

77. Mueller, E. W. J. Appl. Phys. 37- 5001. 1966.

78. Mueller, E. W. J. Phys. Soc. Japan 18, Suppl. 2: 1. 1963.

79. Mueller, E. W. Met. Soc. Conf. 27: 435. 1965.

80. Mueller, E. W. Naturwissenschaften 29: 533. 1941.

81. Mueller, E. W. Phys. Meth. Chem. Anal. 3: 145. 1956.

82. Mueller, E. W. Phys. Rev. 102: 618. 1956.

83. Mueller, E. W. Sci. American 197: 113. 1957.

84. Mueller, E. W. Science 149: 591. 1965.

85. Mueller, E. W. Surface Sci. 2: 484. 1964.

86. Mueller, E. W. Surface Sci. 8: 462. 1967.

87. Mueller, E. W. U.S. Dept. Comm. AFCR-L-62-473 [Air Force Cambridge Research Labs, Washington, D.C.]. 1962.

88. Mueller, E. W. U.S. Dept. Comm. PB-171, 598 [Office of Technical Service, Washington, D.C.]. 1960.

89. Mueller, E. W. Z. Physik 37: 838. 1951.

90. Mueller, E. W. Z. physik. Chem. [Frankfurt] 53:204. 1967.

91. Mueller, E. W., Nakamura, S. J. Appl. Phys. 36: 2535. 1965.

92. Mueller, E. W., Nakamura, S., McLane, S. G., Nishikawa, O. Int. Vac. Congr., 3rd, 2: 431. 1966.

93. Mueller, E. W., Nakamura, S., Nishikawa, O., McLane, S. B. J. Appl. Phys. 36: 2496. 1965.

94. Mueller, E. W., Nishikawa, O. National Aiernautics and Space Administration N63-17, 893. 1963.

95. Mueller, E. W., Nishikawa, O. Rev. Sci. Instr. 36: 556. 1965.

96. Mueller, E. W., Panitz, J. A., McLane, S. B. Rev. Sci. Instr. 39: 83. 1968.

97. Mueller, E. W., Young, R. D. J. Appl. Phys. 32: 2425. 1961.

98. Mulson, J. F., Mueller, E. W. J. Chem. Phys. 38: 2615. 1963.

99. Naik, S. C., Mann, R. S. Can. J. Chem. 45: 1023. 1967.

100. Nakamura, S., Adachi, T. Jap. J. Appl. Phys. 6: 780. 1967.

101. Newman, R. W., Hren, J. J. Surface Sci. 8: 373. 1967.

102. Newman, R. W., Sanwald, R. C., Hren, J. J. J. Sci. Instr. 44: 828. 1967.

103. Nicholas, J. F. An atlas of models of crystal structures. New York, New York, Gordon and Breach Science Publishers. 1965.

104. Nishikawa, O., Mueller, E. W. J. Appl. Phys. 35: 2806. 1964.

105. Nishikawa, O., Mueller, E. W. J. Appl. Phys. 38: 3159. 1967.

106. Orchin, M. Adv. Catalysis 16: 1. 1966.

107. Perry, A. J., Brandon, D. G. Phil. Mag. 16: 119. 1967.

108. Perry, A. J., Brandon, D. G. Surface Sci. 7: 422. 1967.

109. Pimbley, W. T., Ball, R. M. Rev. Sci. Instr. 36: 225. 1967.

110. Propst, F. M., Piper, T. C. Vacuum Sci. Tech. 4: 53. 1967.

111. Ralph, B., Brandon, D. G. J. Roy. Microscop. Soc. 82: 179. 1964.

112. Ranganathan, S., Lyon, H. B., Thomas, G. J. Appl. Phys. 38: 4957. 1967.

113. Redhead, P. Vacuum 12: 203. 1962.

114. Rendulic, K. D. J. Less Common Metals 12: 441. 1967.

115. Rendulic, K. D., Mueller, E. W. J. Appl. Phys. 38: 2070. 1967.

116. Rendulic, K. D., Mueller, E. W. J. Appl. Phys. 37: 2593. 1966.

117. Rice, M. H., Good, R. H. J. Opt. Soc. Am. 52: 239. 1962.

118. Roberts, R. W. Ann. N.Y. Acad. Sci. 101: 766. 1963.

119. Ryan, H. F., Suiter, J. J. Sci. Instr. 42: 645. 1965.

120. Rye, R. R. Decomposition and hydrogenation studies of simple hydrocarbons on tungsten. Unpublished Ph.D. thesis. Ames, Iowa, Library. Iowa State University of Science and Technology. 1968.

121. Sanwald, R. C., Hren, J. J. Surface Sci. 7: 197. 1967.

122. Sanwald, R. C., Hren, J. J. Surface Sci. 9: 257. 1968.

123. Sanwald, R. C., Ranganathan, S., Hren, J. J. Appl. Phys. Letters 9: 393. 1966.

124. Schagen, P., Woodhead, A. W. Phillips Tech. Reports 28: 161. 1967.

125. Schulz, G. H., Phelps, A. V. Rev. Sci. Instr. 28: 1051. 1957.

126. Schmidt, L. D., Gomer, R. J. Chem. Phys. 42: 3573. 1965.

127. Selwood, P. W. Int. Congr. Catalysis, 2nd, Paris, 2: 1795. 1960.

128. Southon, M. J., Brandon, D. G. Phil. Mag. 8: 582. 1963.

129. Speicher, C. A., Wolff, C. W., Pimbley, W. T. J. Sci. Instr. 44: 167. 1967.

130. Strassma, H., Stark, D. Z. angew. Phys. 23: 40. 1967.

131. Swenson, C. A., Stahl, R. H. Rev. Sci. Instr. 24: 608. 1954.

132. Thomas, L. B. Int. Symp. Rarefield Gas Dynamics 1: 155. 1967.

133. Tsong, T. T. Surface Sci. 10: 102. 1968.

134. Tsong, T. T., Mueller, E. W. Appl. Phys. Letters 9: 7. 1966.

135. Tsong, T. T., Mueller, E. W. J. Appl. Phys. 37: 3065. 1965.

136. Tsong, T. T., Mueller, E. W. J. Chem. Phys. 41: 3279. 1964.

137. Twigg, G. H., Rideal, E. K. Proc. Roy. Soc.(London) A171: 55. 1939.

138. van Oostrom, A. G. J. Phillips Research Reports Suppl. 1. 1966.

139. van Oostrom, A. G. J. Phys. Letters 22: 137. 1966.

140. Vanselow, R. Phys. Stat. Sol. 21: 69. 1967.

141. Vanselow, R., Schmidt, W. A. Z. Naturforsch. A21: 1690. 1966.

142. Waclawski, B. J., Mueller, E. W. J. Appl. Phys. 32: 1472. 1961.

143. Weizer, V. G. J. Appl. Phys. 38: 4535. 1967.

144. Young, R. D., Mueller, E. W. J. Appl. Phys. 33: 91. 1962.

ACKNOWLEDGMENTS

The author wishes to acknowledge, first and foremost, the assistance of Dr. Robert S. Hansen. Professor Hansen's efficacy in constructing concise models to rationalize seemingly inexplicable data has been most helpful. Equally appreciated was his ability to explain involved theoretical concepts in simple yet most instructive terminology.

The author also wishes to acknowledge:

Robert R. Rye for many thoughtful hours of often-times fruitful discussion on a variety of topics, some pertaining to surface chemistry,

Robert R. Frost for many enjoyable hours of discussion at the Veenker Memorial Laboratory,

P. T. Dawson and N. C. Gardner for permission to use figures and data in this thesis,

Dr. C. Swenson for suggesting the use of a continuous helium transfer in FIM experiments and assisting in its design,

The many individuals and shops which have constructed equipment or performed needed services as typlified by Thomas Kelley and the Graphic Arts Department, Everett McKenna and the Glass Blowing Shop, Wayne Reinhardt and the Instrumentation Group, Garry Wells and the Research Shop,

Last but not least in importance, the author wishes to thank Wendy, Jay, Bryan and his wife, Gaye, for making nearly five years in Ames both rewarding and enjoyable. I

particularly hope that W., J., and B., as native-Iowans, have enjoyed their stay in Iowa as much as I have mine.

APPENDIX

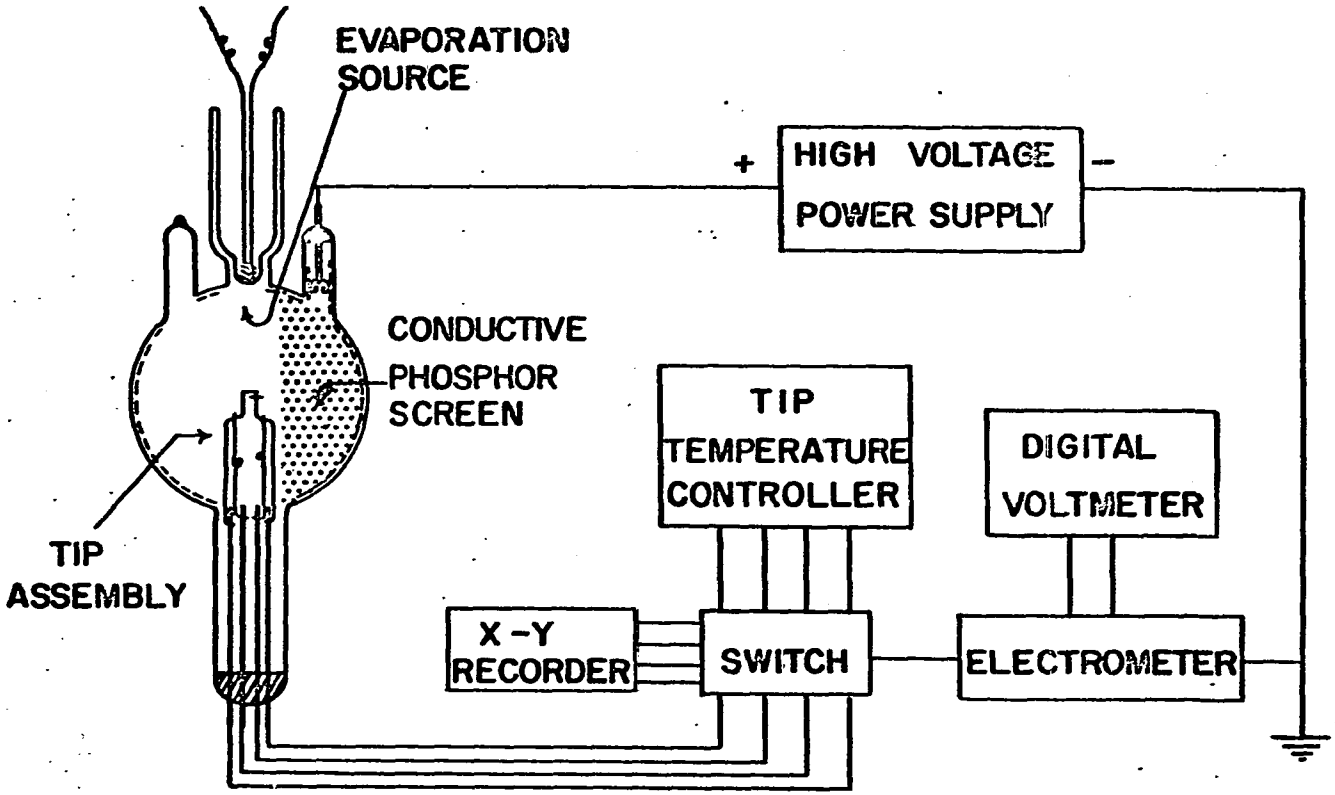

THE FIELD EMISSION MICROSCOPE

Figure 1. Schematic of a field electron emission microscope with attendant electronic equipment

Figure 2. Indexed field electron emission micrograph of clean tungsten

The location of crystal planes is shown in the upper portion of the micrograph. Corresponding work function values (eV) are shown in their mirror images in the bottom portion of the micrograph


311
611
310
611
210
320
4·2
4·3
4·2
4·2

Figure 3. Orthographic projection of [110]-oriented cubic crystal showing planes which form for b.c.c. tungsten. Zone lines are indicated by: [100], ----- , [111], ... , [110], _____

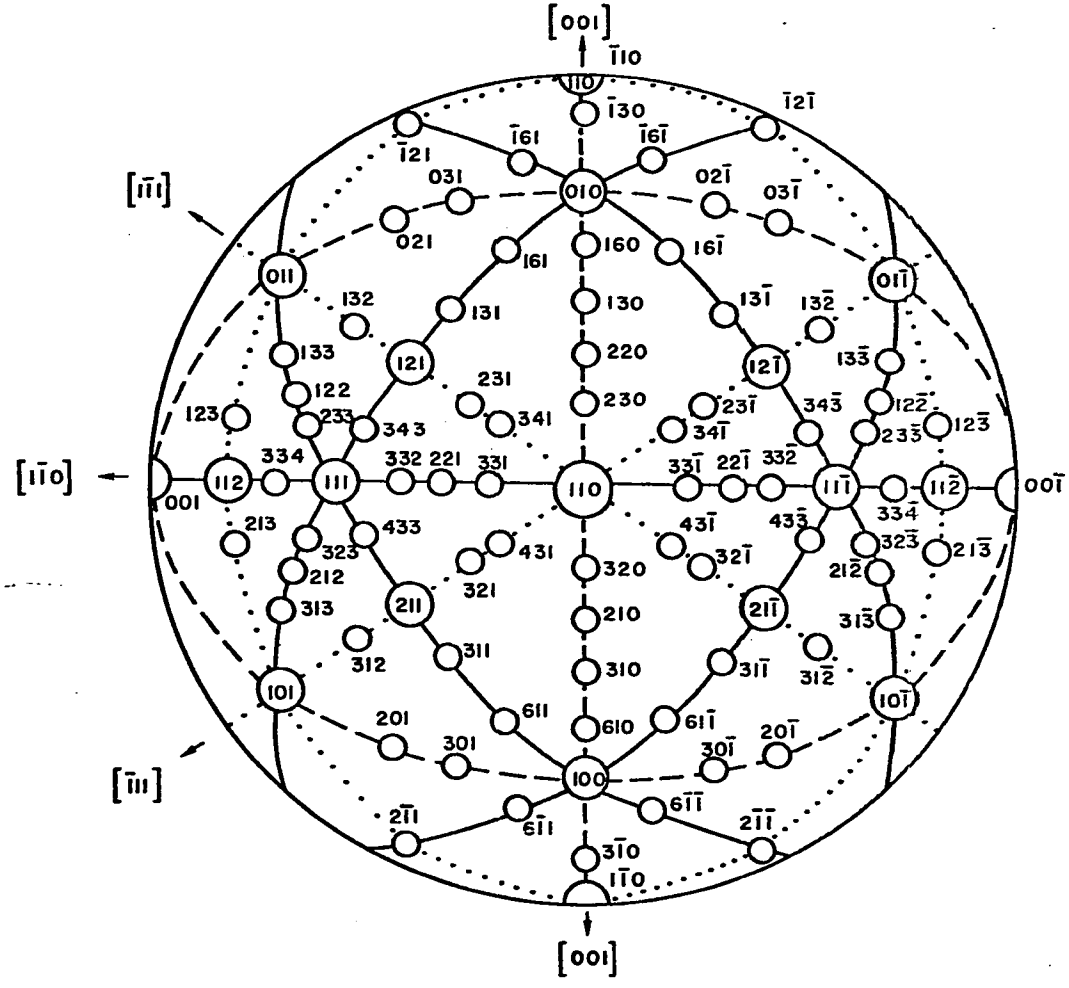
[001]
[1̄11]
[1̄10]
[1̄1̄1]
[001]
001
001̄
110
1̄10
1̄30
1̄21
1̄61
1̄6̄1
1̄2̄1
031
02̄1
03̄1
021
160
16̄1
011
011̄
132
131
130
13̄1
13̄2
133
121
220
12̄1
13̄3̄
122
231
230
23̄1
34̄3
12̄2̄
123
233
343
341
34̄1
23̄3̄
12̄3̄
334
332
221
331
33̄1
22̄1
33̄2
112
111
110
11̄1
11̄2̄
334̄
213
433
431
43̄1
43̄3̄
32̄3̄
21̄3̄
323
320
32̄1
212
21̄2̄
321
211
21̄1
313
31̄3̄
312
311
31̄1
31̄2̄
101
101̄
201
611
610
61̄1
20̄1
301
30̄1
100
2̄11
6̄11
6̄1̄1
2̄1̄1
3̄10
1̄10

Figure 4. Physical model for electron emission from metal surface in high electric fields

The barrier to electron emission in vacuum is lowered by an image force (top figure). In a high electric field of ~0.3 V/Å, the barrier is thinned and lowered still further (bottom figure). This permits electron tunnelling through the deformed barrier from the highest occupied metal levels.

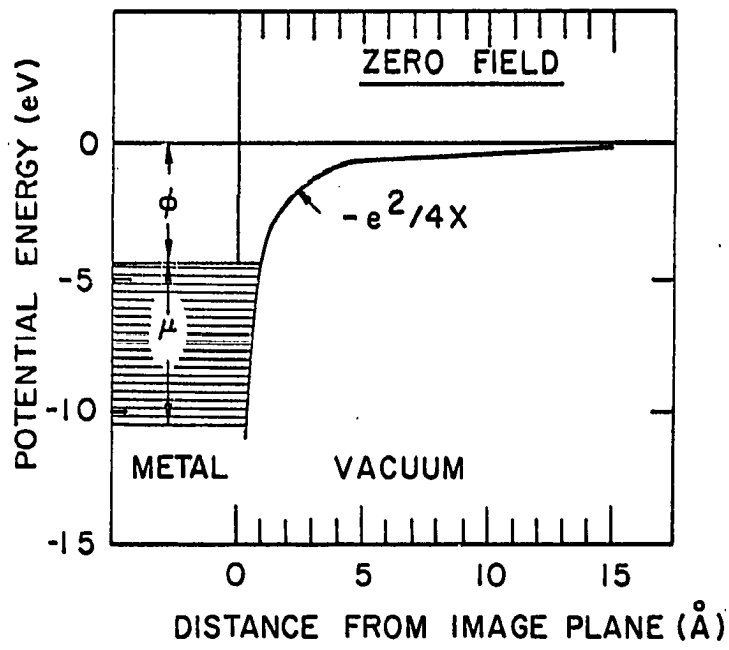
ZERO FIELD
POTENTIAL ENERGY (eV)
0
-5
-10
-15
ϕ
μ
$-e^2/4X$
METAL
VACUUM
0
5
10
15
DISTANCE FROM IMAGE PLANE (Å)

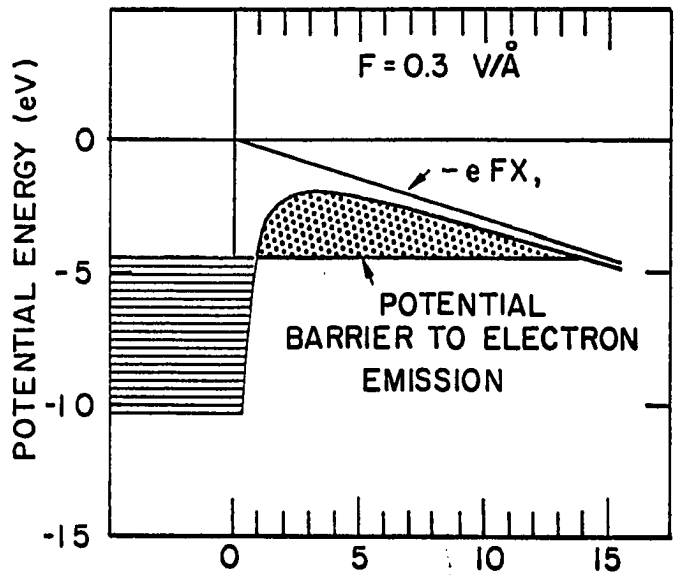
F = 0.3 V/Å
POTENTIAL ENERGY (eV)
0
-5
-10
-15
$-eFX$,
POTENTIAL
BARRIER TO ELECTRON
EMISSION
0
5
10
15

Figure 5. Conductive coating deposition apparatus

The $SnCl_4$-N_2 stream is mixed with an oxygen stream inside the microscope tube. The oxygen stream is the more powerful of the two streams and blows the $SnCl_4$ into all corners of the tube

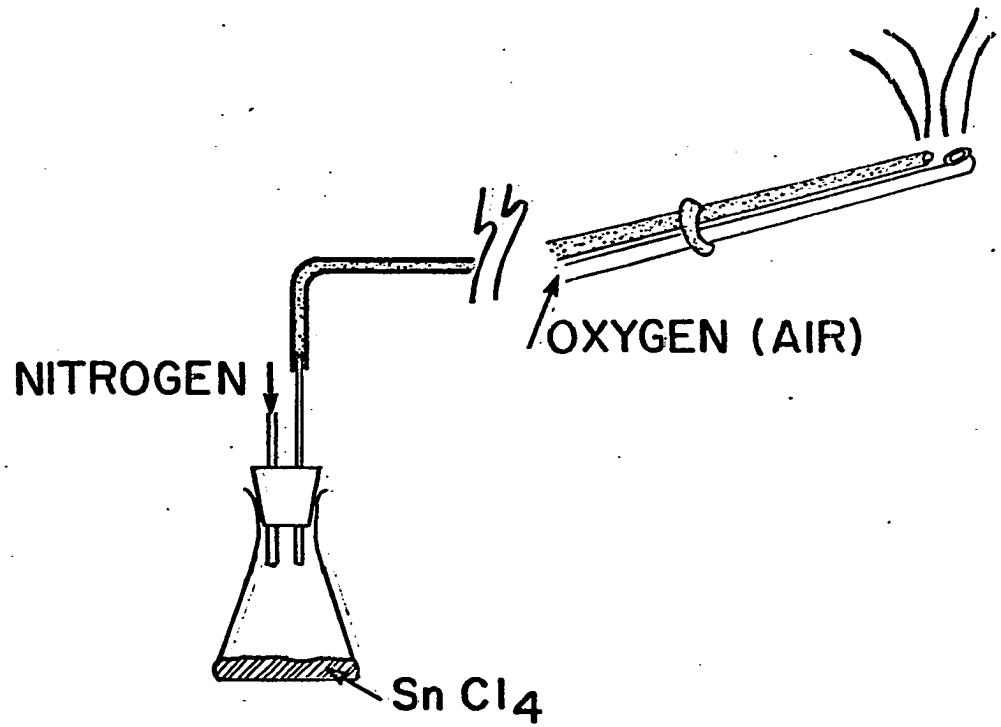
NITROGEN
OXYGEN (AIR)
Sn Cl4

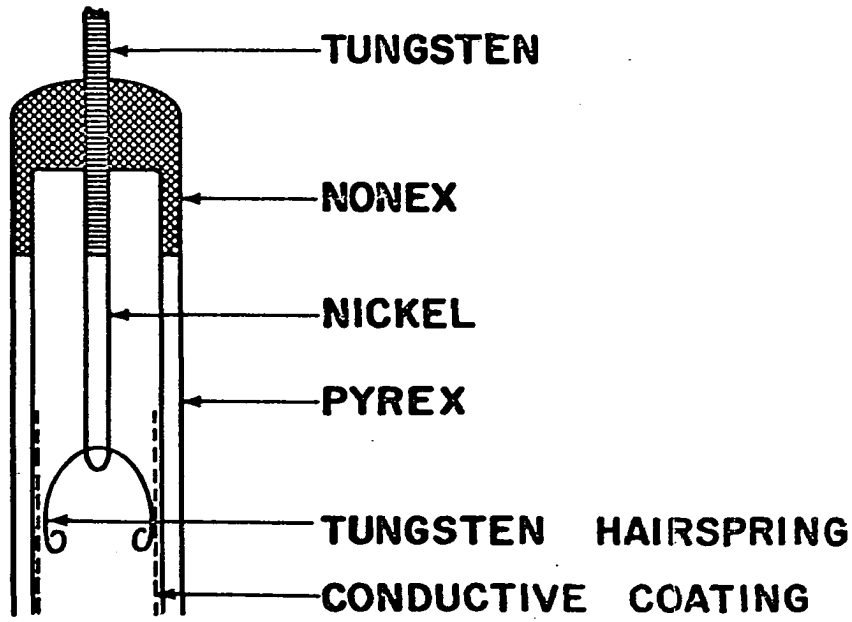

Figure 6. Tungsten hair spring electrical connections to an ultra-high vacuum system

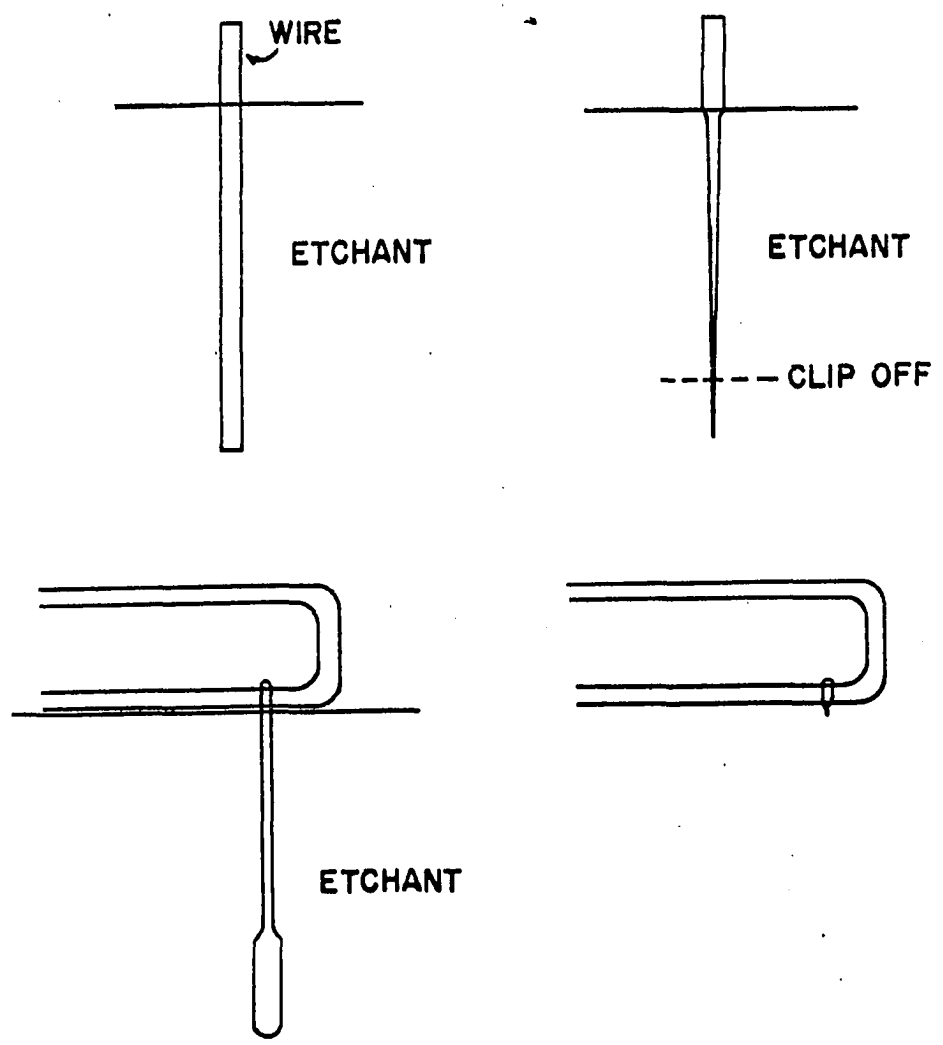

Figure 7. Schematic of tip etching operations

Figure 8. Liquid helium cryostat

A. Inlet port for liquid helium transfer
B. Shielded high voltage lead
C. Port for pumping out inner dewar. Not shown is a flutter-valve for venting helium boil-off
D. Valve through which jacket around inner dewar could be pumped
E. Grounding pin for inner dewar jacket
F. Rubber sleeving making gas tight connections to high voltage lead-in, inner- and outer-dewar
G. Unsilvered portions of inner- and outer-dewar
H. Inlet port for liquid nitrogen transfer
I. Electrical leads through a rubber stopper
J. Mounting blocks supporting dewar assemblies to movable rack
K. Flange with O-ring seal connecting "head" of dewar to inner-dewar

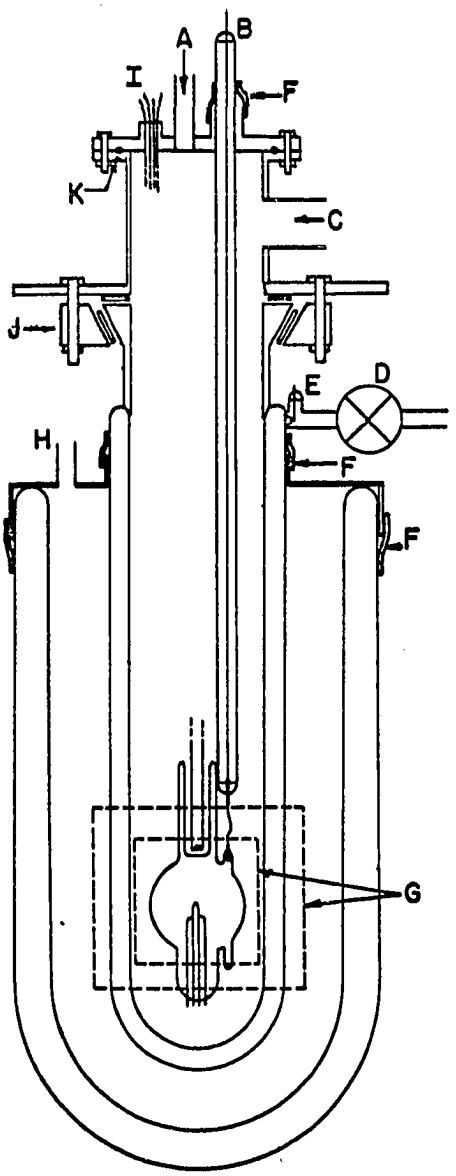
A
B
I
F
K
C
J
D
E
H
F
F
G

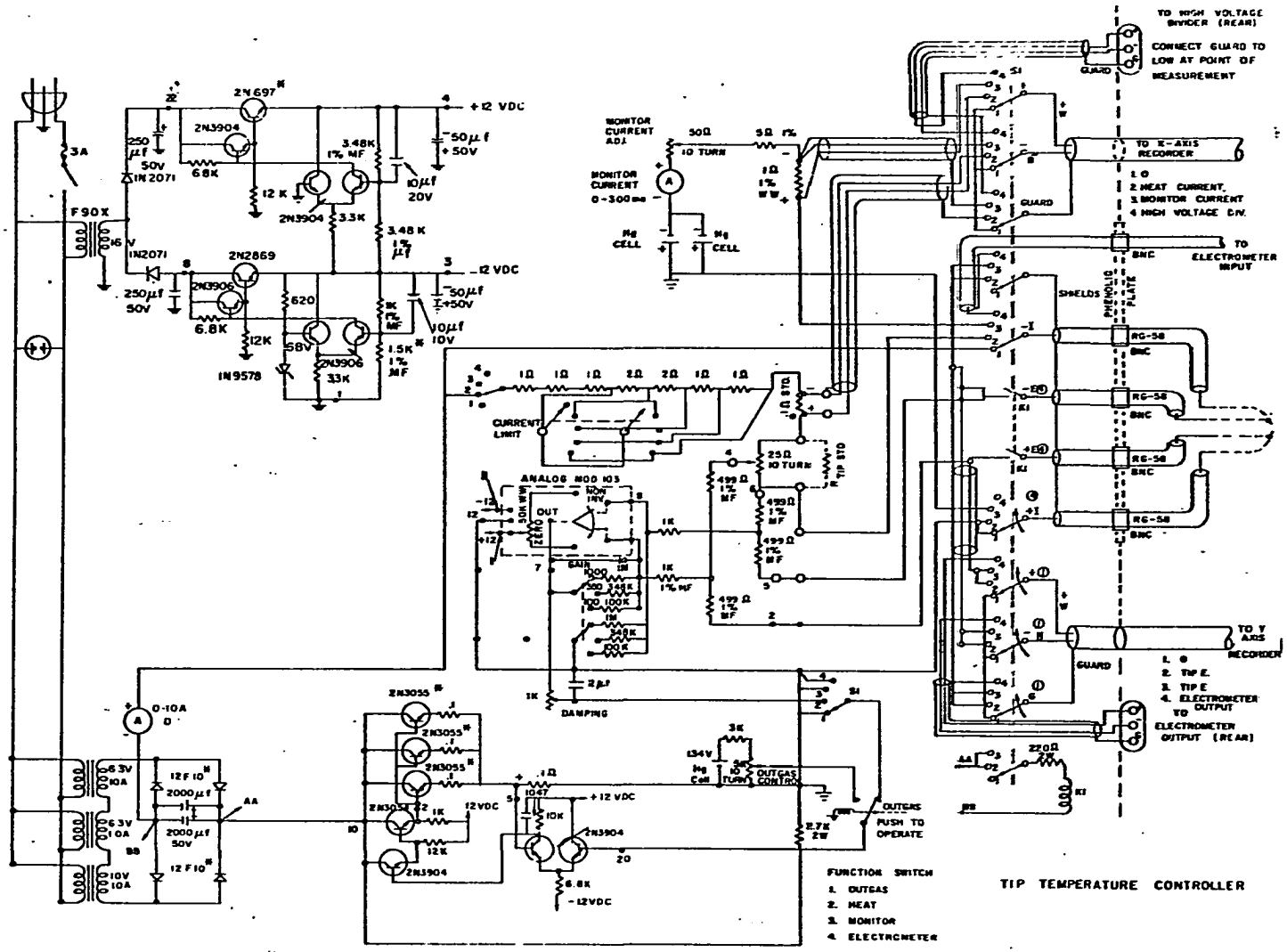

Figure 9. Schematic diagram of tip temperature controller.

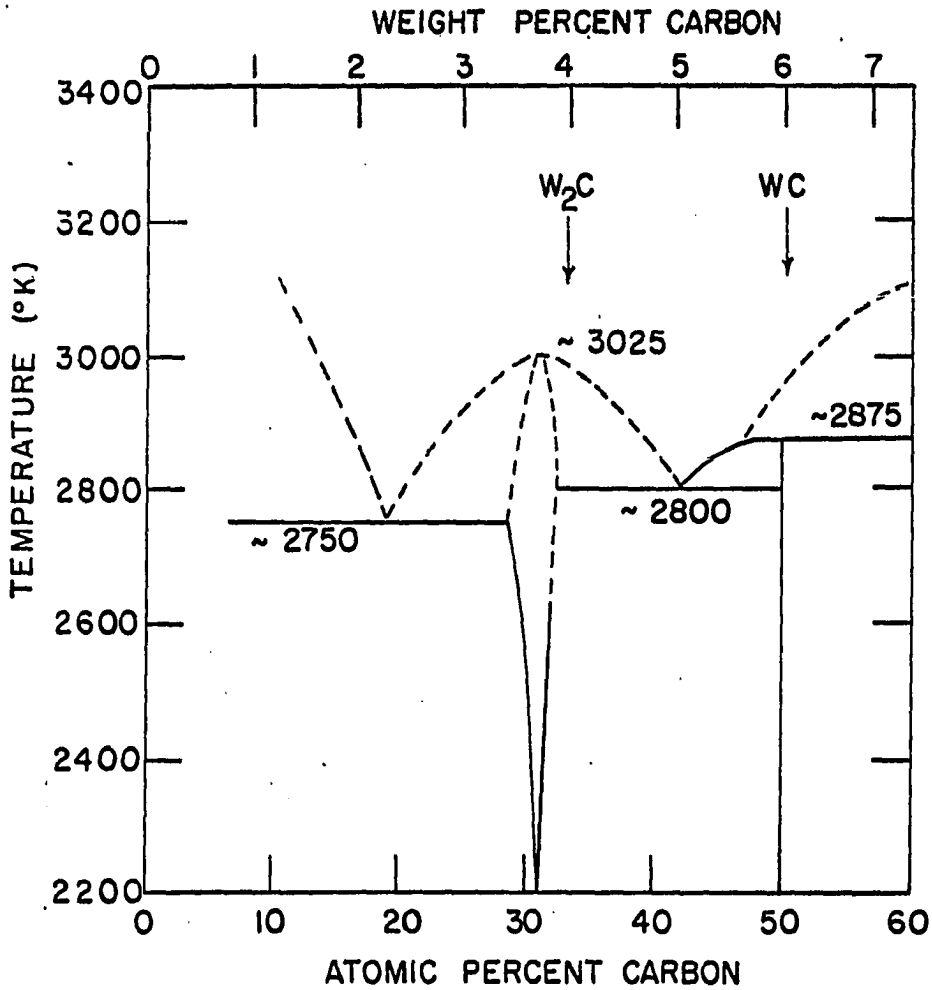

Figure 10. Tungsten-carbon phase diagram.

Two stoichiometric carbides, W_2C, WC are known. WC decomposes above 2875°K but W_2C decomposition requires temperatures above 3000°K.

Figure 11. Ethylene molecular images on tungsten emitters

Top: left - clean, field evaporated tungsten pattern

right - monolayer ethylene dose heated to ~180°K

Middle: left - single ethylene molecular image on a lightly dosed tip

right - the same surface at reduced voltage. Almost all emission is from the molecular image

Bottom: Another ethylene molecular image on a shadowed tip. The clean tungsten surface is at the bottom of the pattern while the molecular image emanates from a tip region covered by multi-layers of ethylene

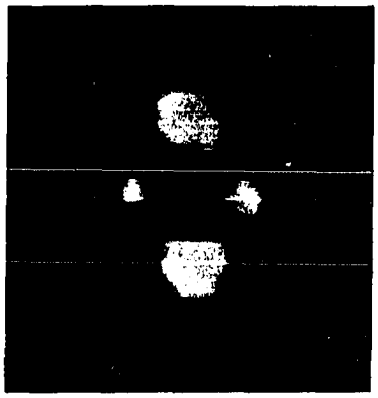

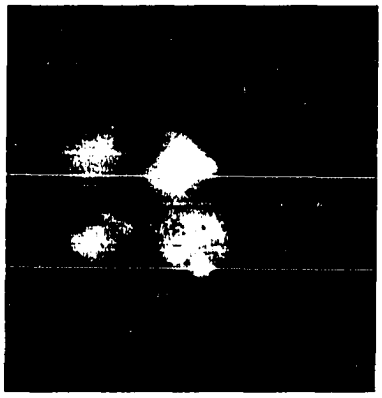

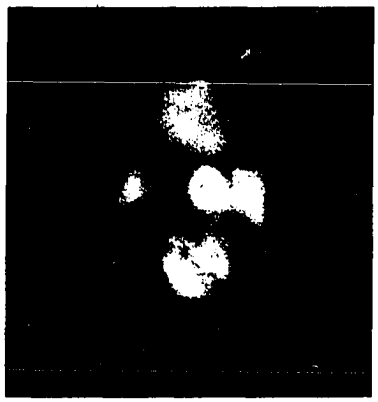

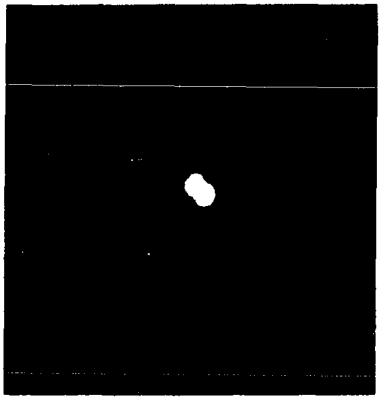

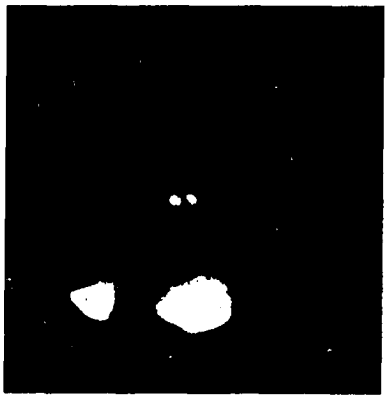

Figure 12. Changing FEEM patterns of a single ethylene molecular image on a multi-layer-covered tungsten tip

The voltage applied to the tip was constant throughout the sequence and the patterns pictured were photographed over a period of 15 minutes

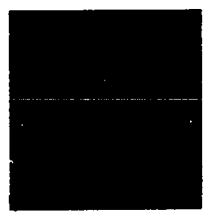

(a)

(b)

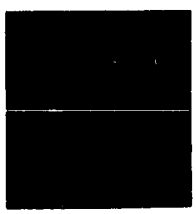

(c)

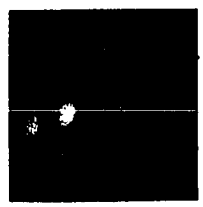

(d)

(e)

(f)

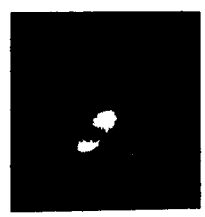

(g)

(h)

(i)

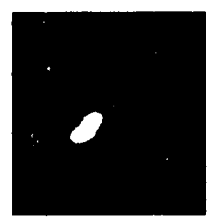

(j)

Figure 13. Photograph of field electron emission microscopy laboratory

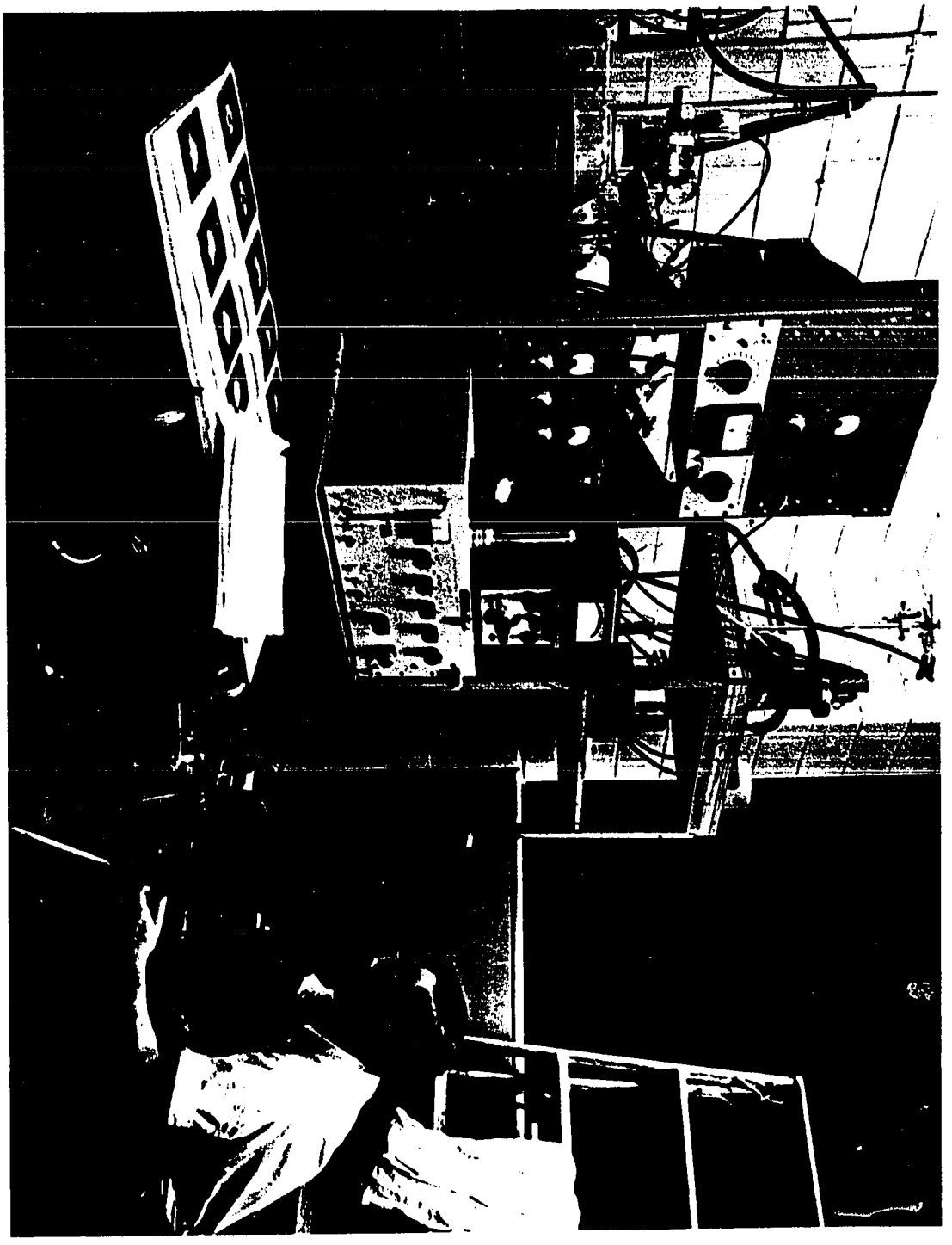

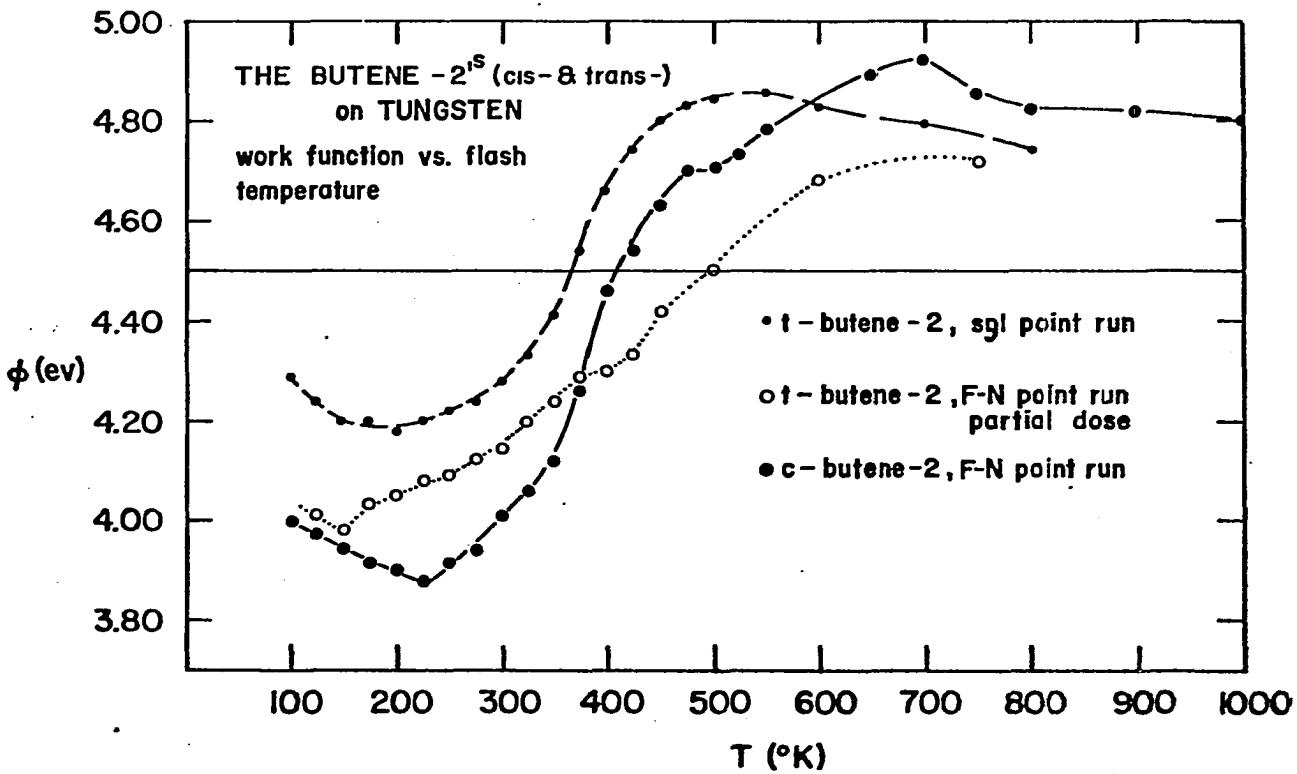

Figure 14. Work function versus temperature plots for cis-2-butene and trans-2-butene.

- monolayer dose of trans-2-butene, work functions computed by single point method.

O incomplete monolayer dose of trans-2-butene, work functions computed from F-N plots.

● monolayer dose of cis-2-butene, work function computed from F-N plots.

Figure 15. Chemisorbed trans-2-butene and its degradation products are immobile to at least 500°K as demonstrated from FEEM patterns of a shadowed tungsten tip

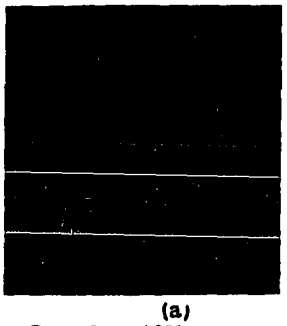

(a)
Dosed at 4°K

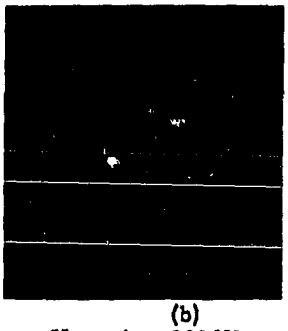

(b)
Heated to 300°K

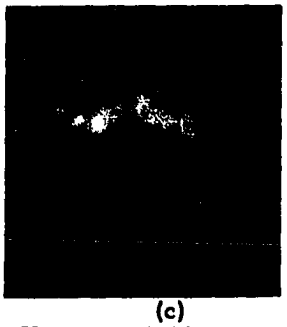

(c)
Heated to 400°K

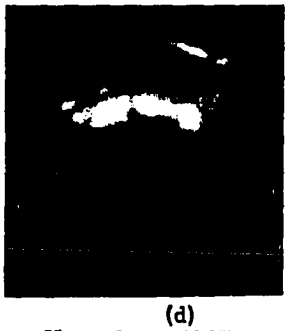

(d)
Heated to 450°K

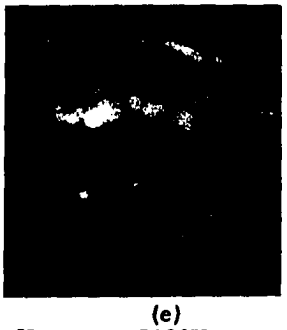

(e)
Heated to 500°K

(f)
Heated to 600°K

Figure 16. FEEM patterns of a tungsten tip, covered with a monolayer of cis-2-butene and trans-2-butene, heated to temperatures from 100°K-700°K (pages 215, 216, 217, and 218)

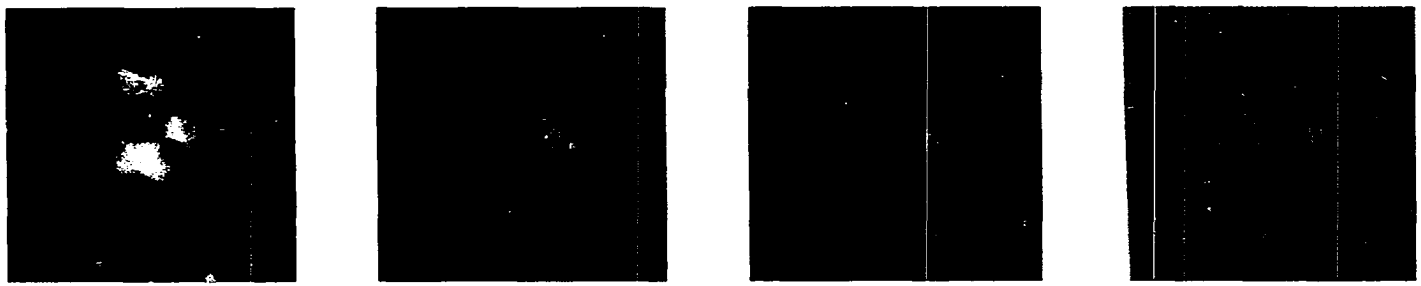

trans-butene-2

---------CLEAN----------HEATED TO 100°K----------HEATED TO 125°K----------HEATED TO 150°K------

cis-butene-2

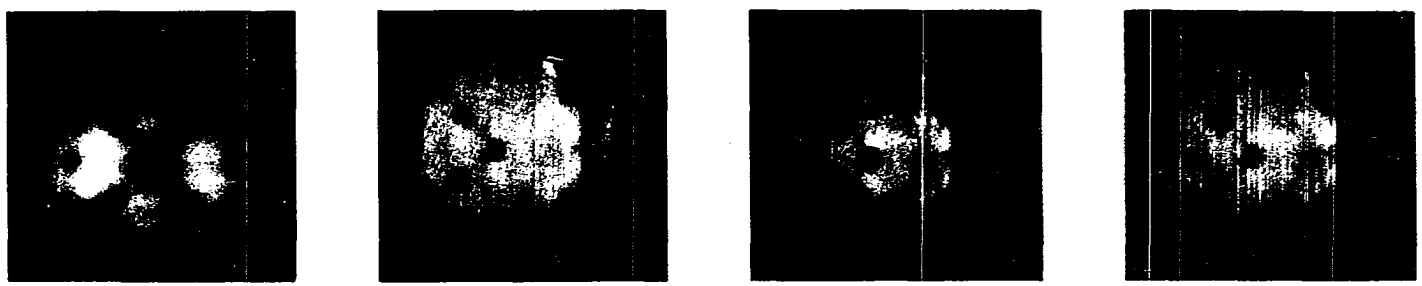

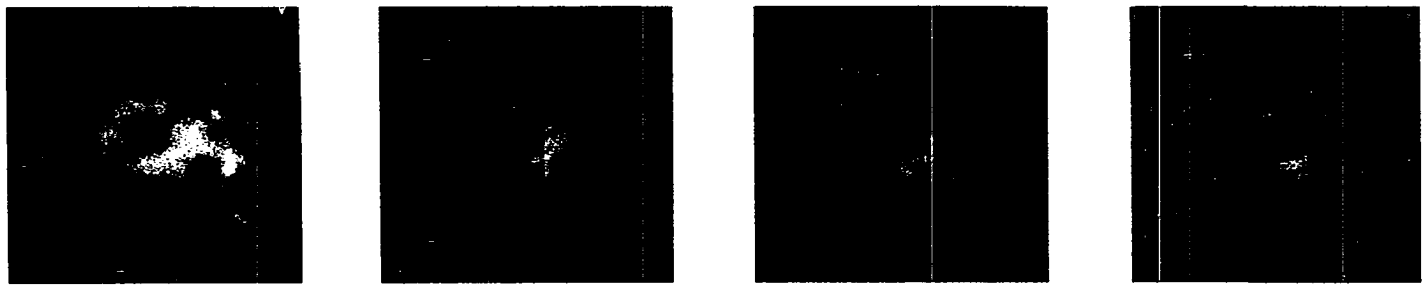

trans-butene-2

-------HEATED TO 200°K-------- HEATED TO 250°K----------HEATED TO 300°K----------HEATED TO 350°K-----

cis-butene-2

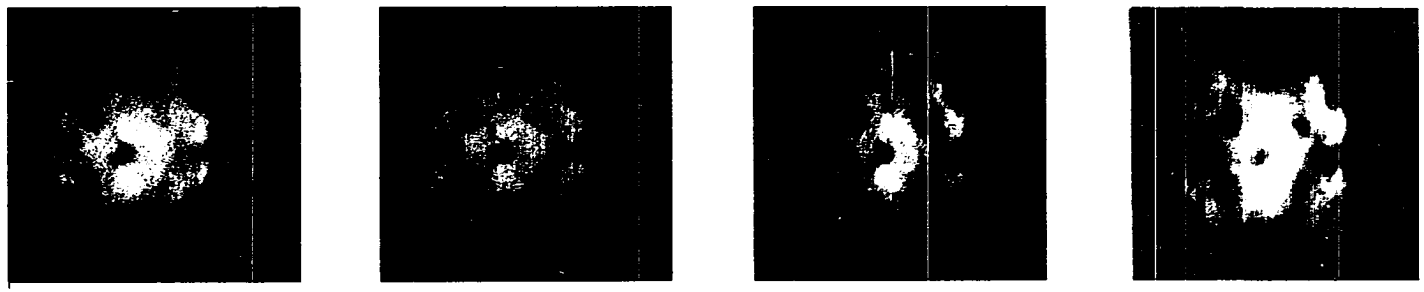

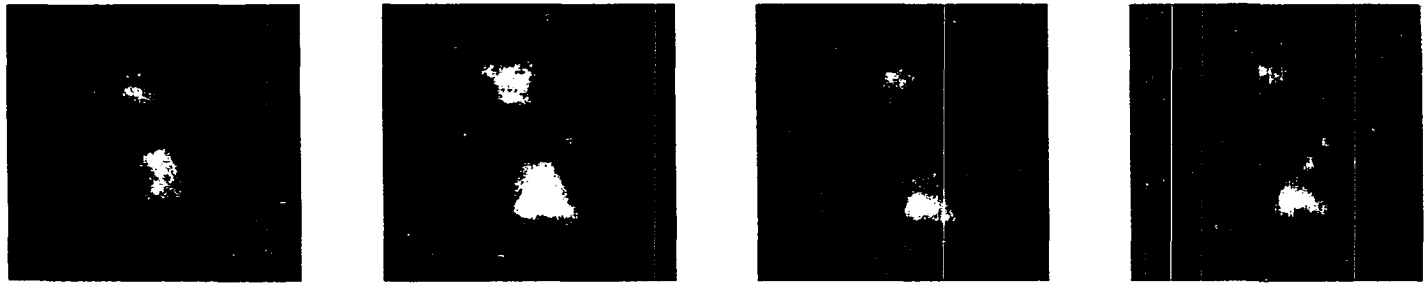

trans-butene-2

--------HEATED TO 400°K -------- HEATED TO 450°K ---------- HEATED TO 500°K---------- HEATED TO 550°K-------

cis-butene-2

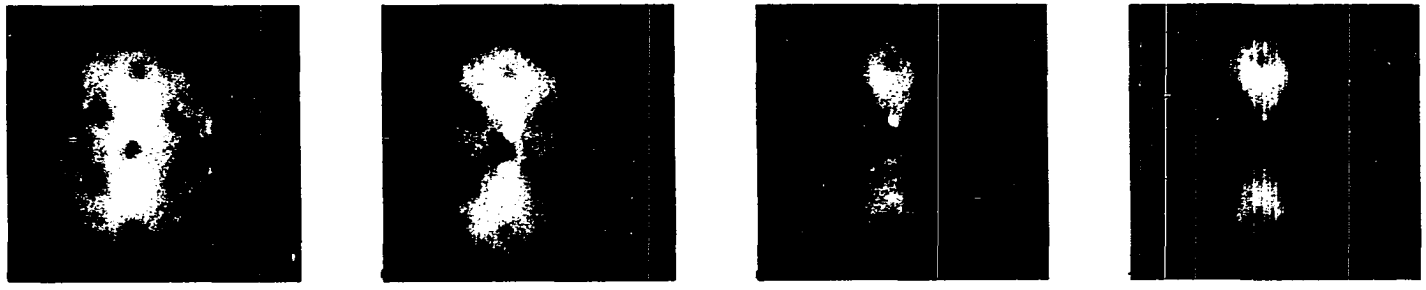

trans-butene-2

----------HEATED TO 600°K---------HEATED TO 700°K----------

cis-butene-2

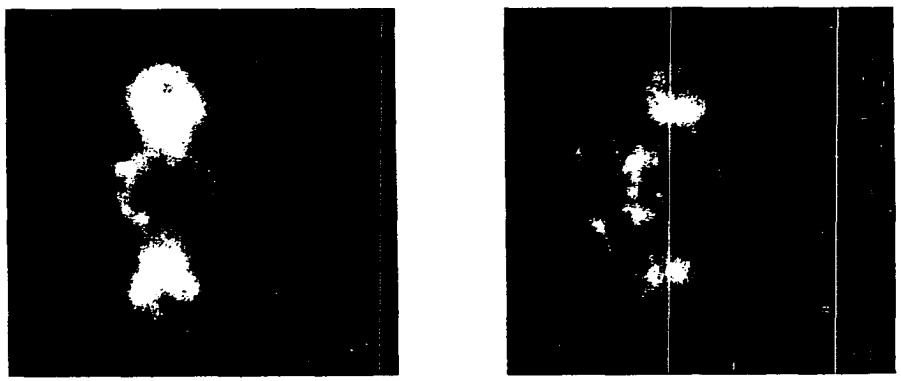

Figure 17. Second layer migration of cis-2-butene on a clean tungsten surface

Top: Clean tungsten surface

Bottom: left - cis-2-butene dosed with field off at 4°K
right - short heating interval at ~90°K

The remaining six pictures (pages 221 and 222) illustrate the effects of longer heating intervals at the same temperature. The boundary between clean metal surface and chemisorbed cis-2-butene is seen in the bright band running horizontally across the micographs

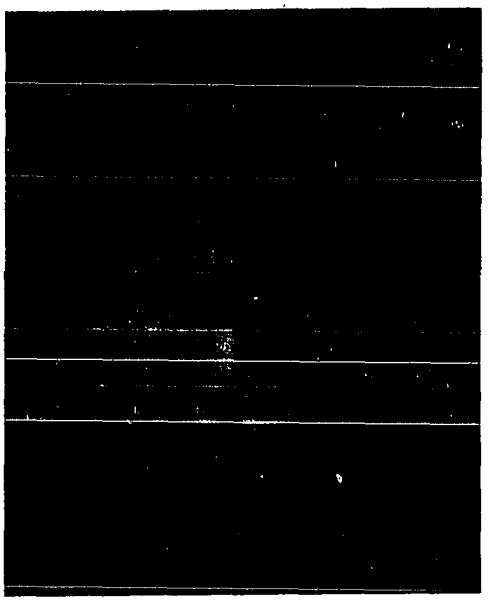

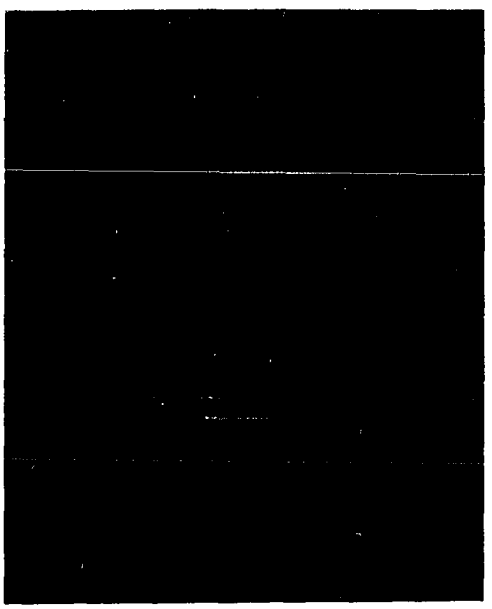

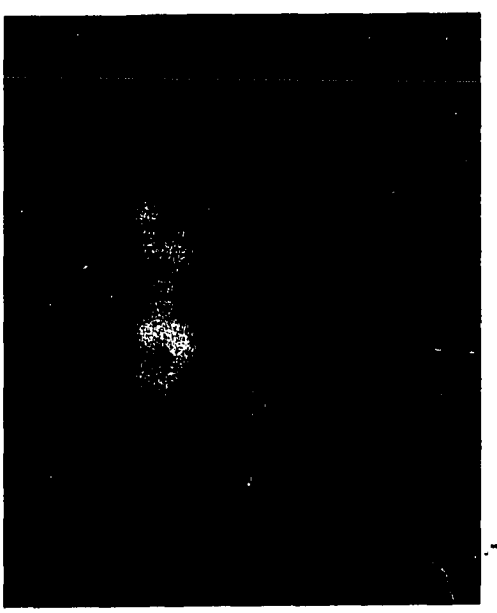

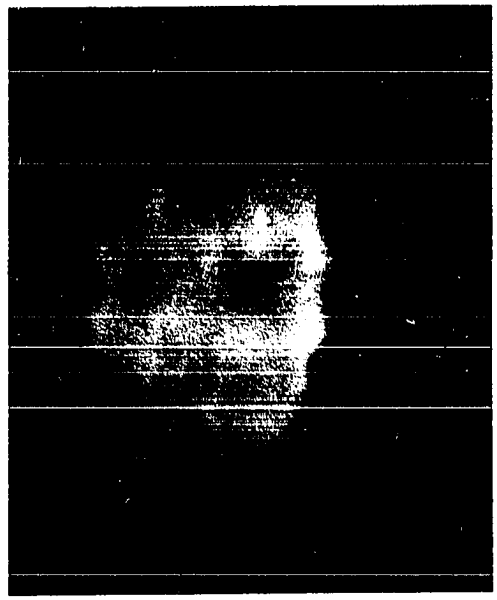

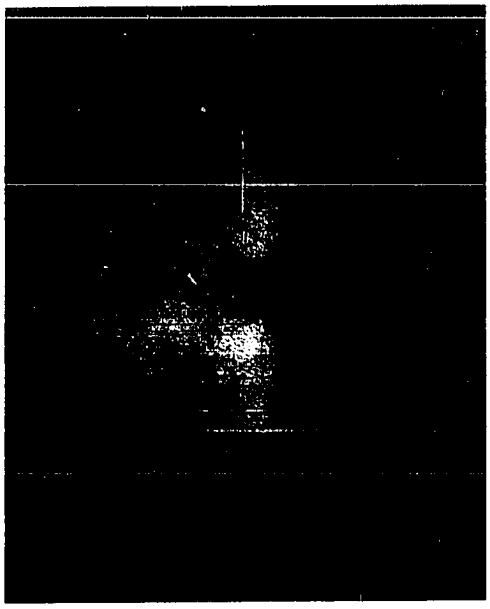

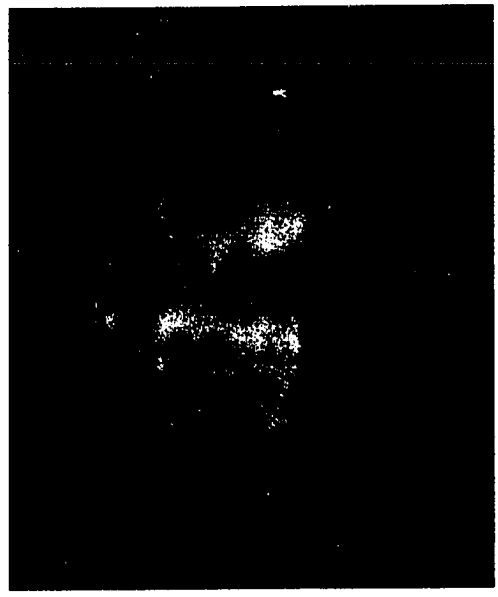

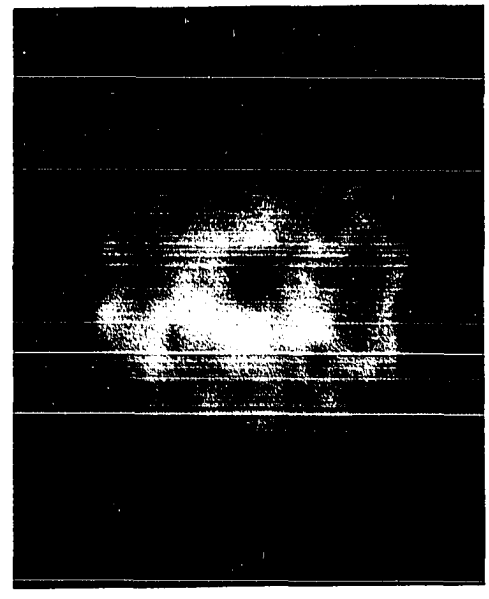

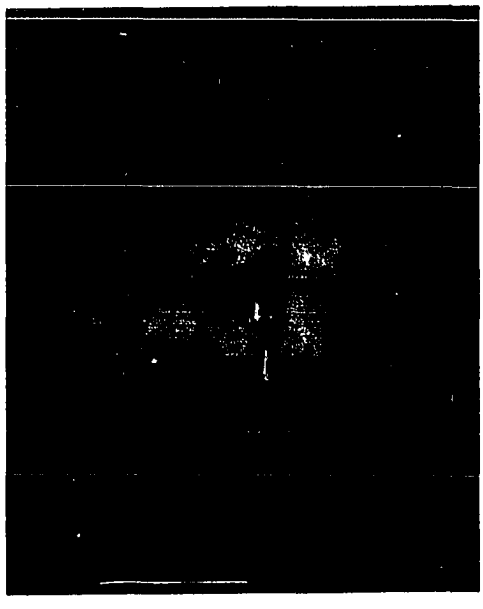

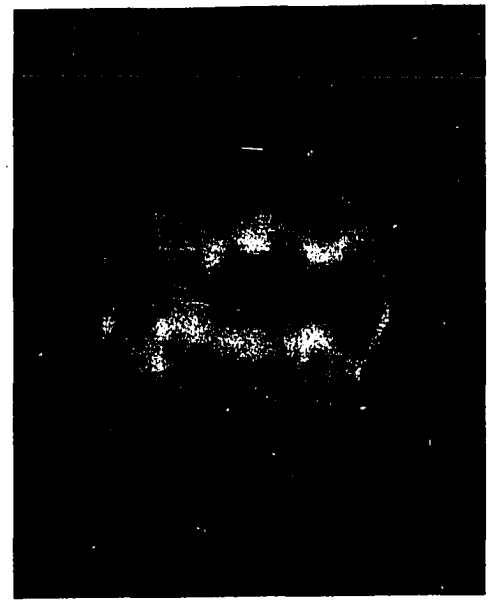

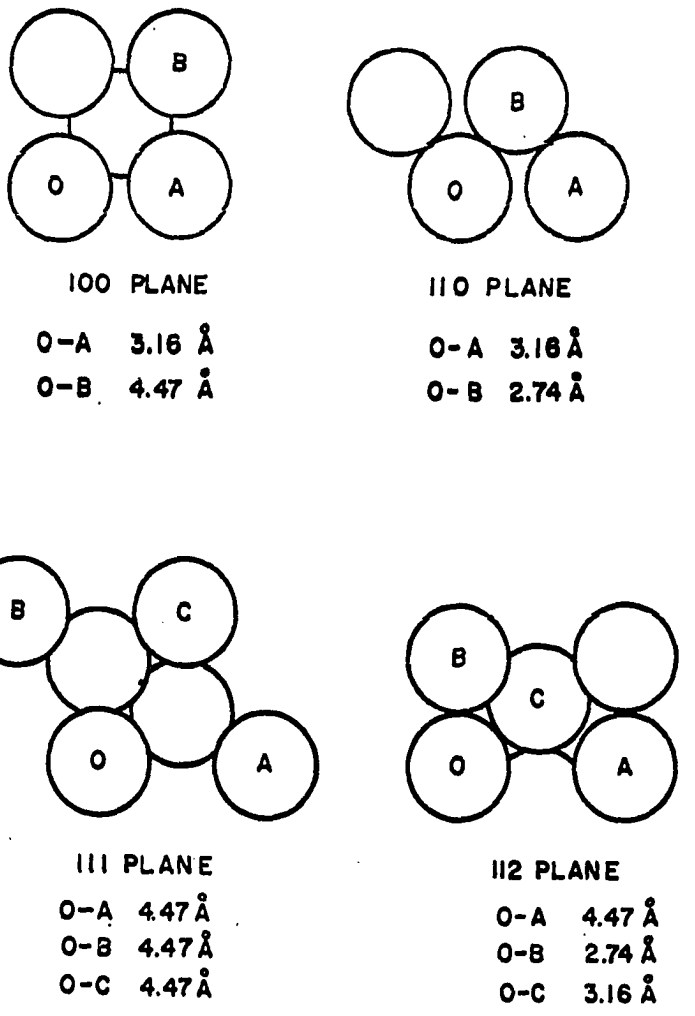

Figure 18. Atom geometries and spacings on four low index planes exposed on tungsten emitters

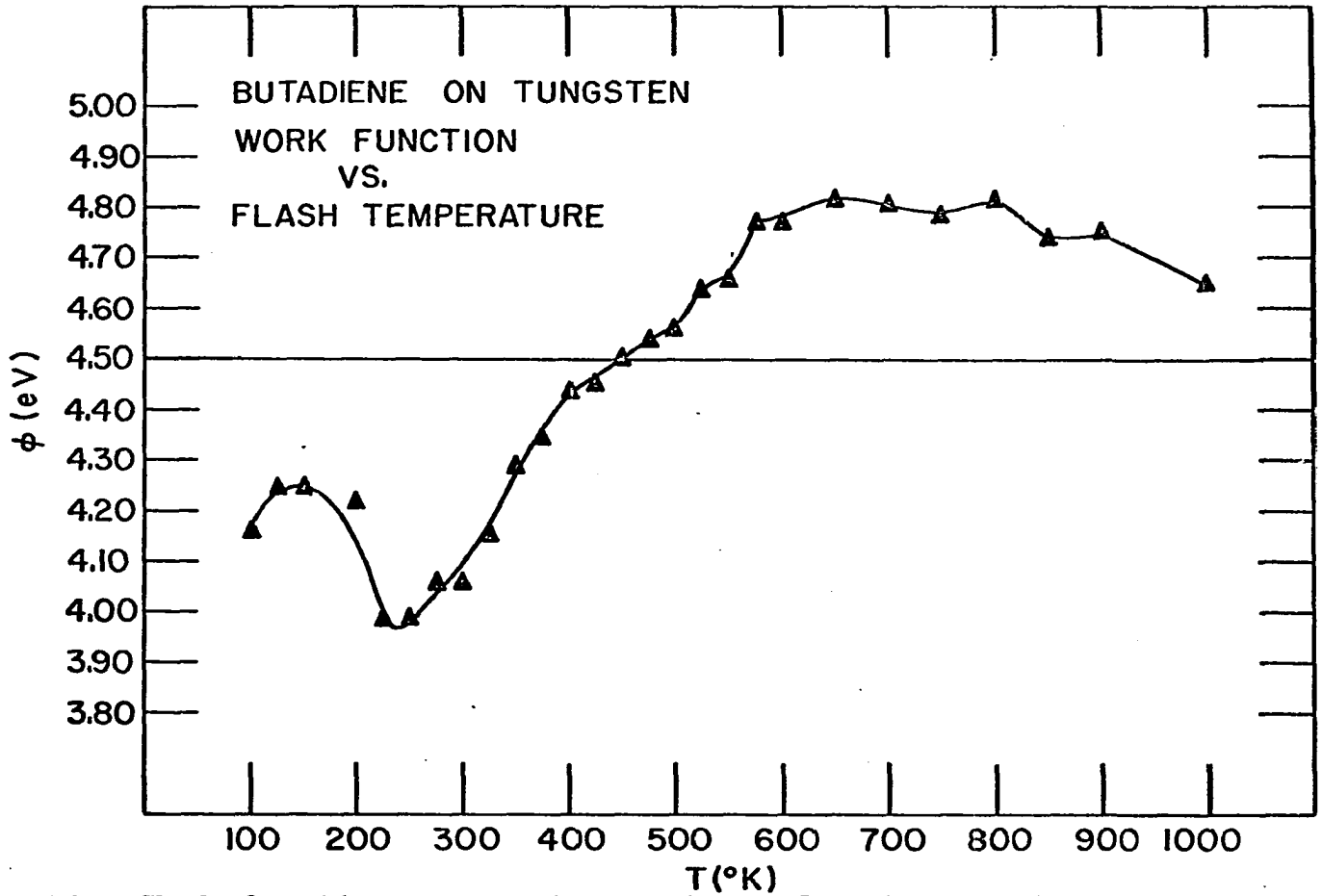

Figure 19. Work function versus temperature plot for monolayer dose of 1,3-butadiene.

Figure 20. FEEM patterns of a tungsten tip, covered with a monolayer of 1,3-butadiene, heated to temperatures between 100°K-900°K (pages 226 and 227)

DECOMPOSITION OF BUTADIENE ON TUNGSTEN

clean surface

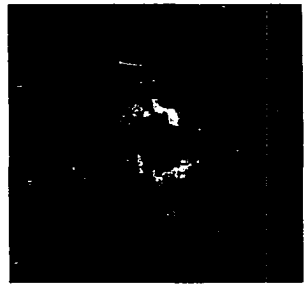

heated to 100°K

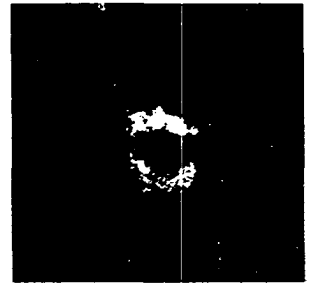

heated to 130°K

heated to 170°K

---

heated to 210°K

heated to 240°K

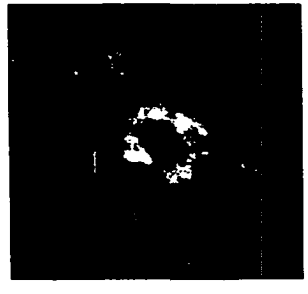

heated to 270°K

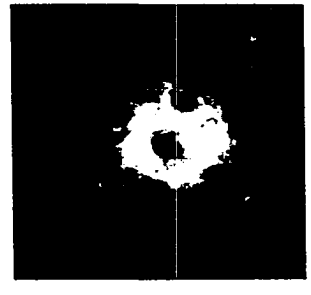

heated to 300°K

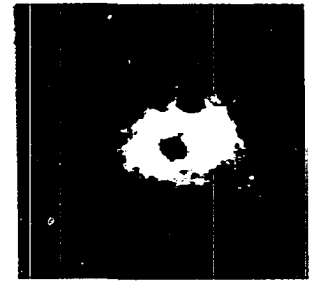

heated to 350°K

heated to 400°K

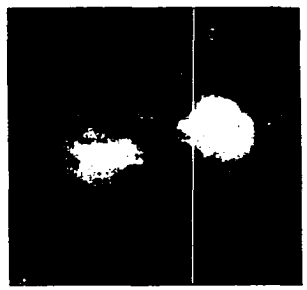

heated to 425°K

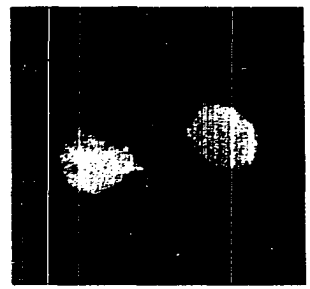

heated to 450°K

---

heated to 500°K

heated to 600°K

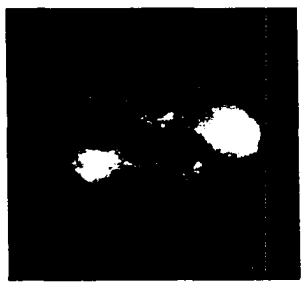

heated to 750°K

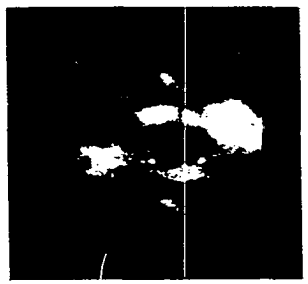

heated to 900°K

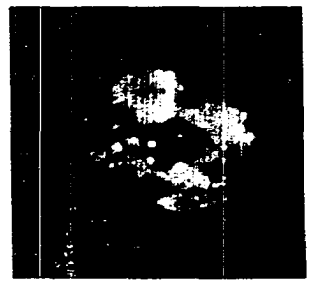

Figure 21. Comparison of helium ion microscopy image (top) of a field evaporated tungsten emitter with a field electron microscopy image of a similar emitter (bottom).

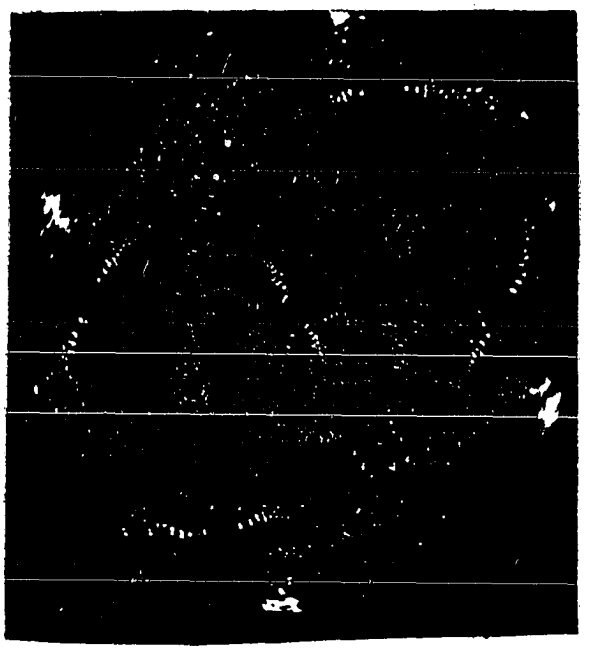

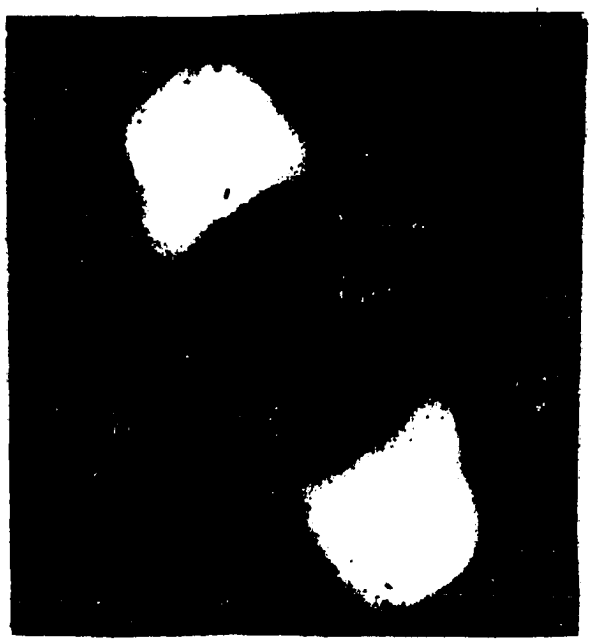

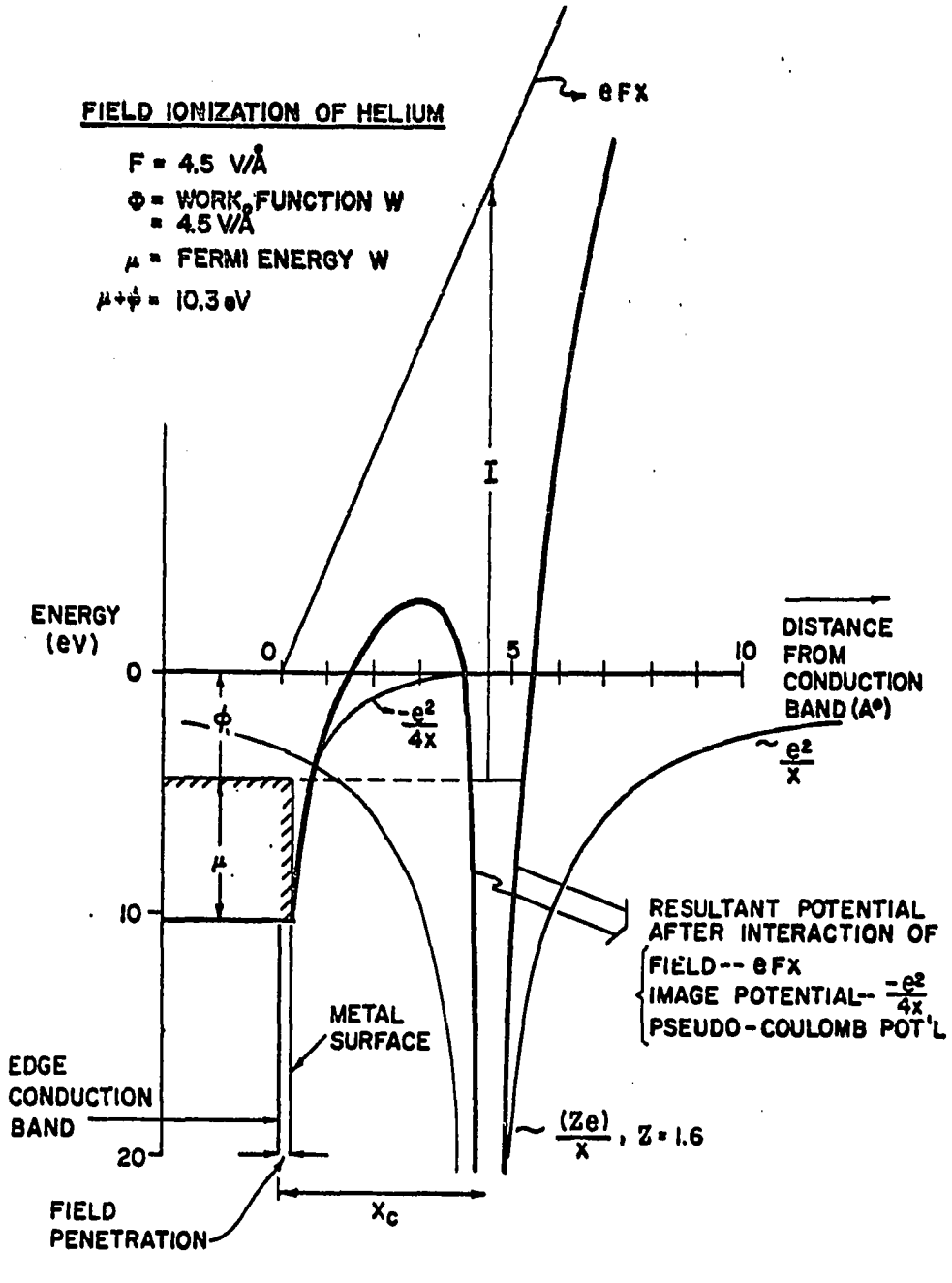

Figure 22. Field ionization of helium at a tungsten surface in the presence of an electric field of ~ 4.5 V/A

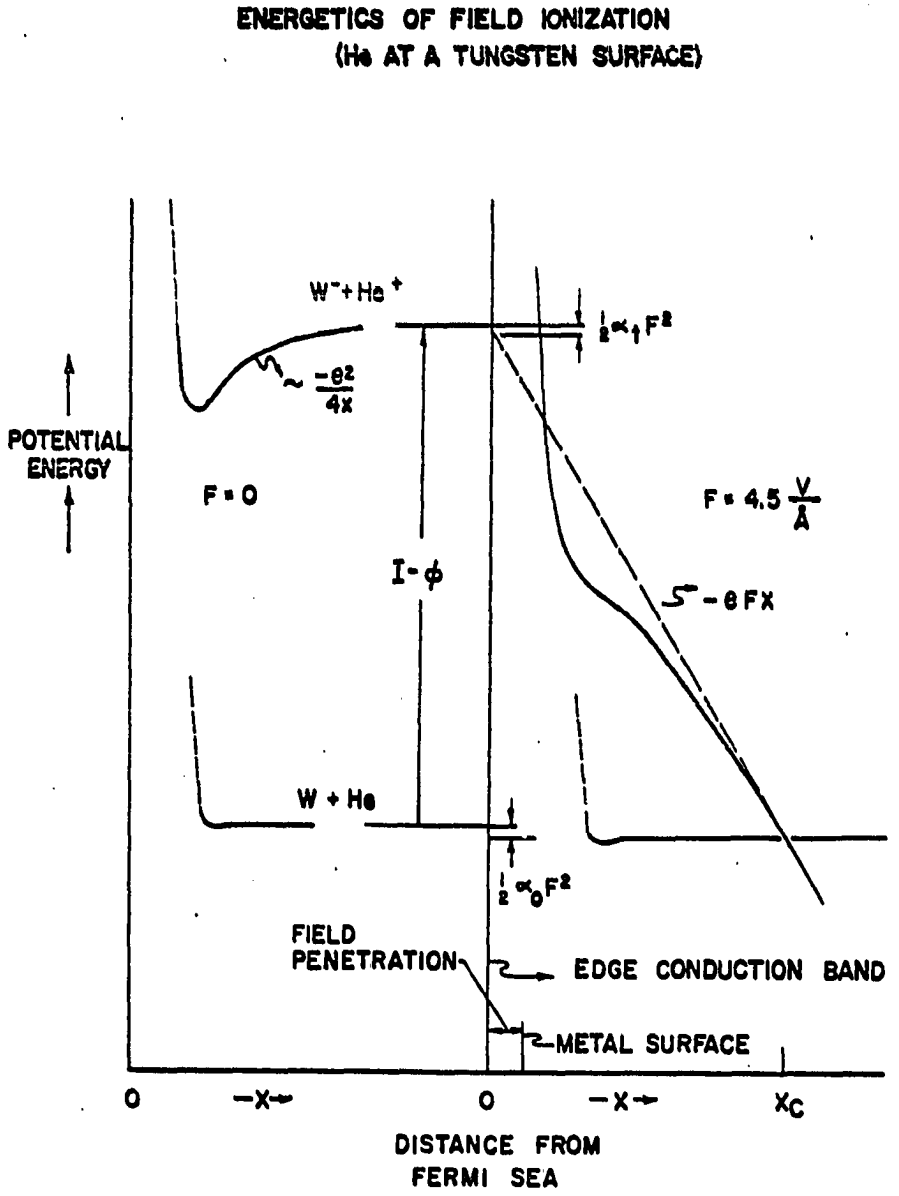

Figure 23. Energetics of field ionization of helium at a tunsten surface in the presence, and absence, of an applied electric field

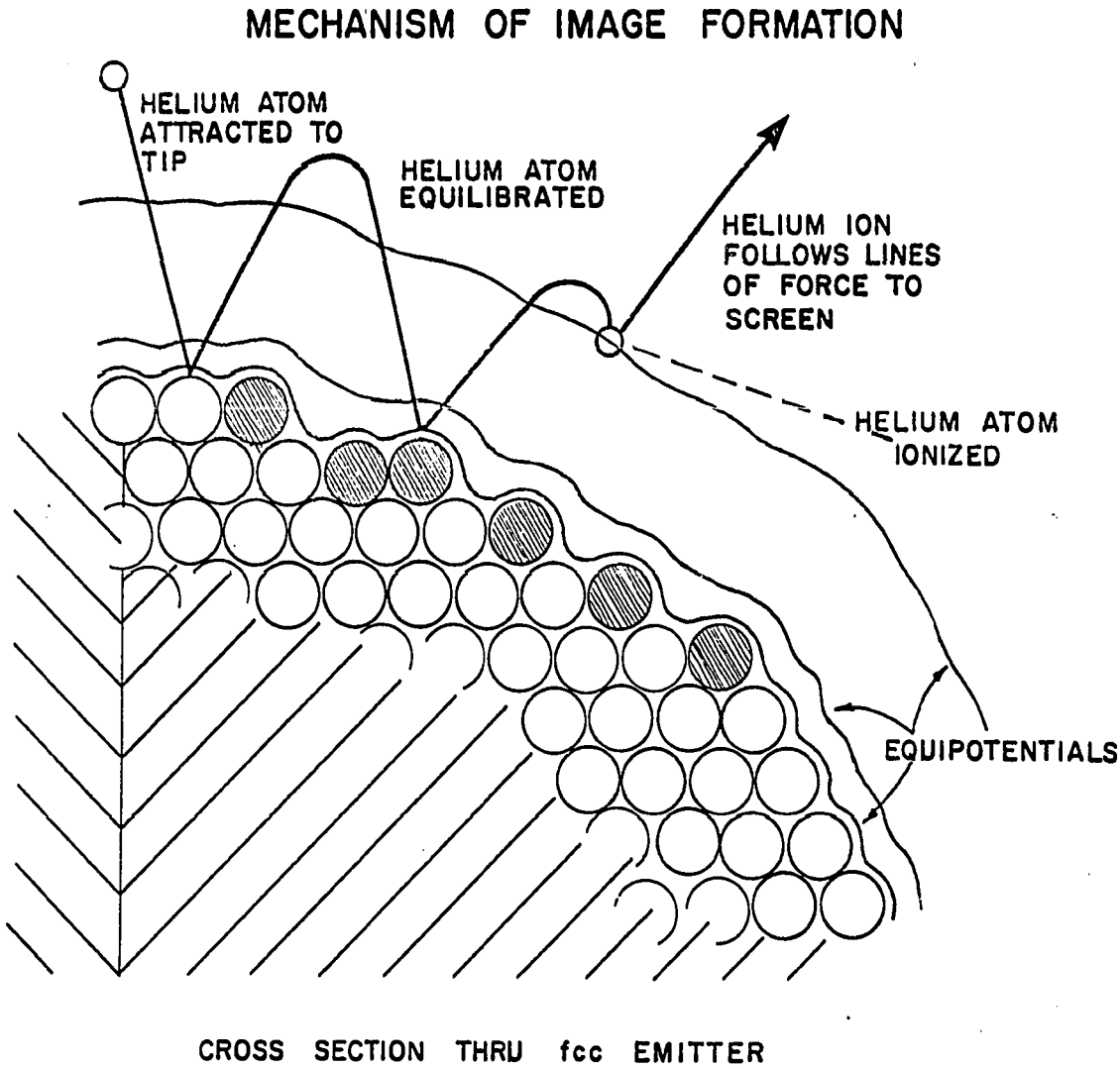

Figure 24. Field profiles at a metal surface

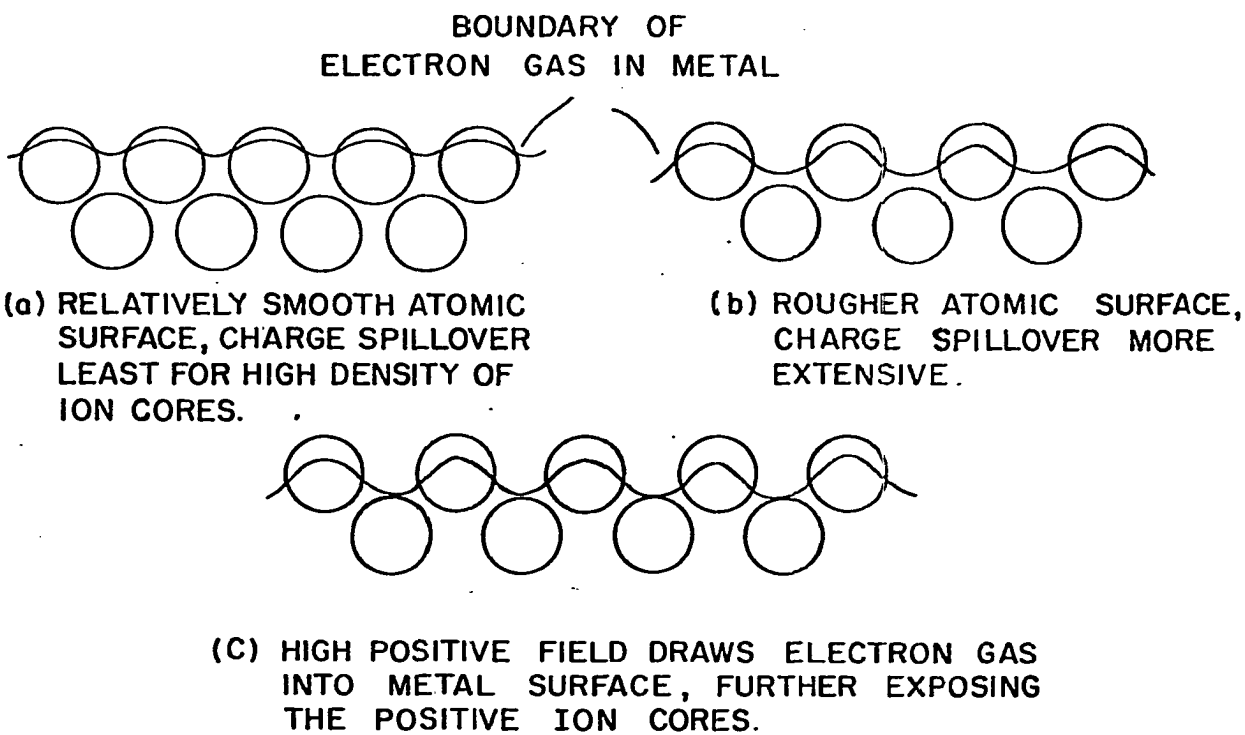

Figure 25. Contours of charge distribution at a metal surface

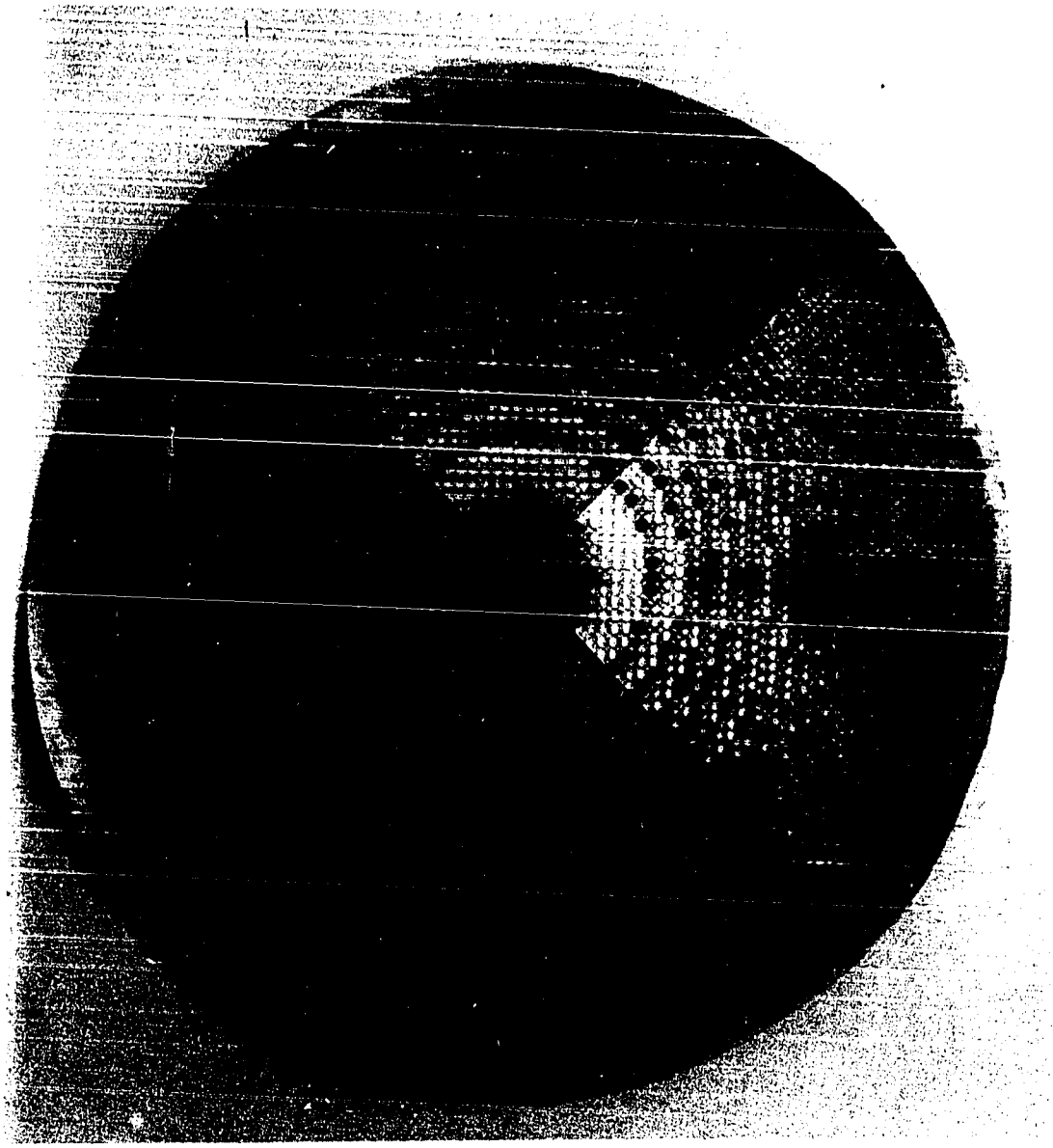

Figure 26. Ball model of a [100]-oriented face-centered-cubic emitter

A quarter section of a model displaying four-fold symmetry has been photographically made into a hemispherical tip cap.

Figure 27. Decoration atoms in a low temperature helium ion micrograph of tungsten

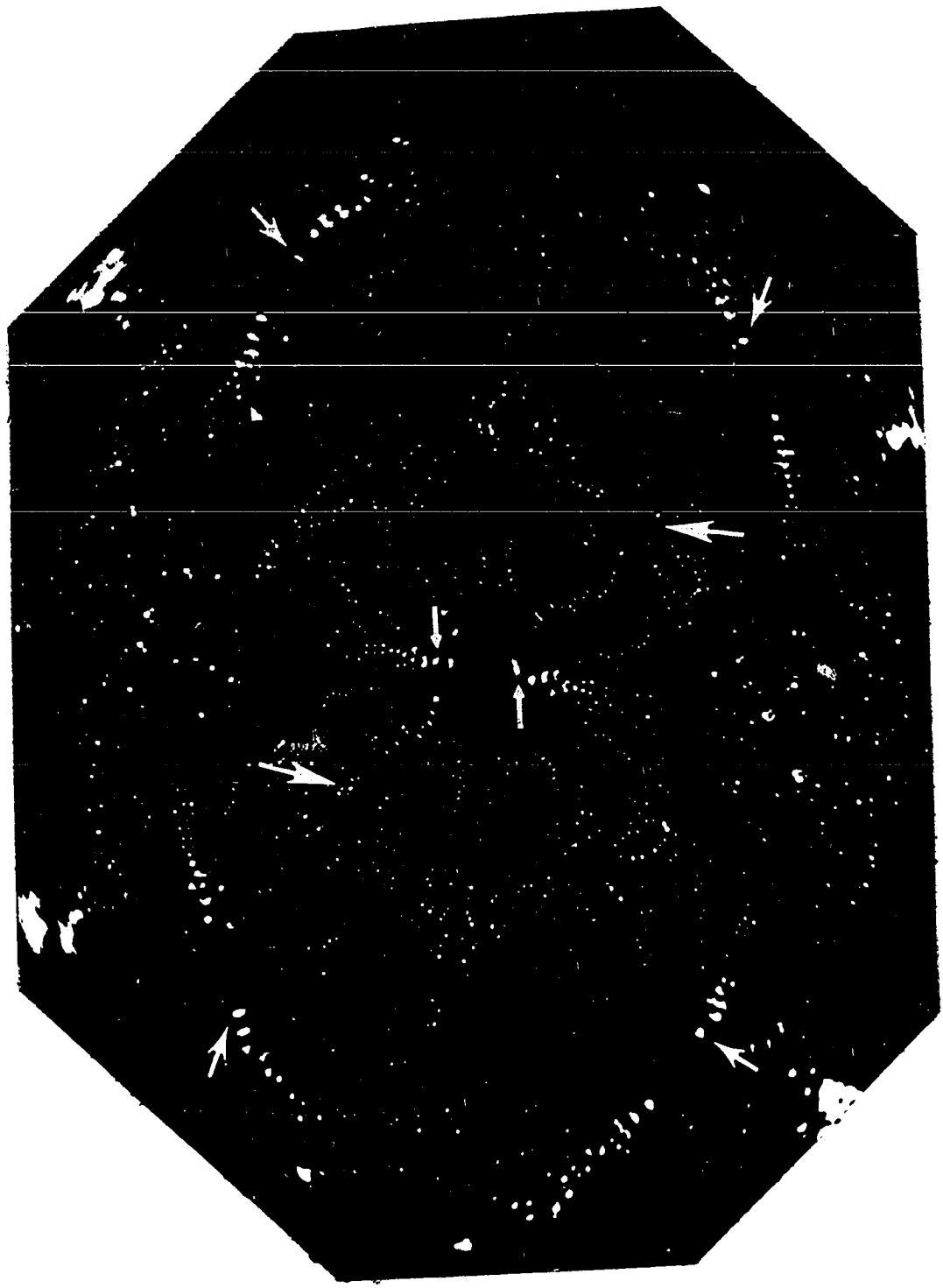

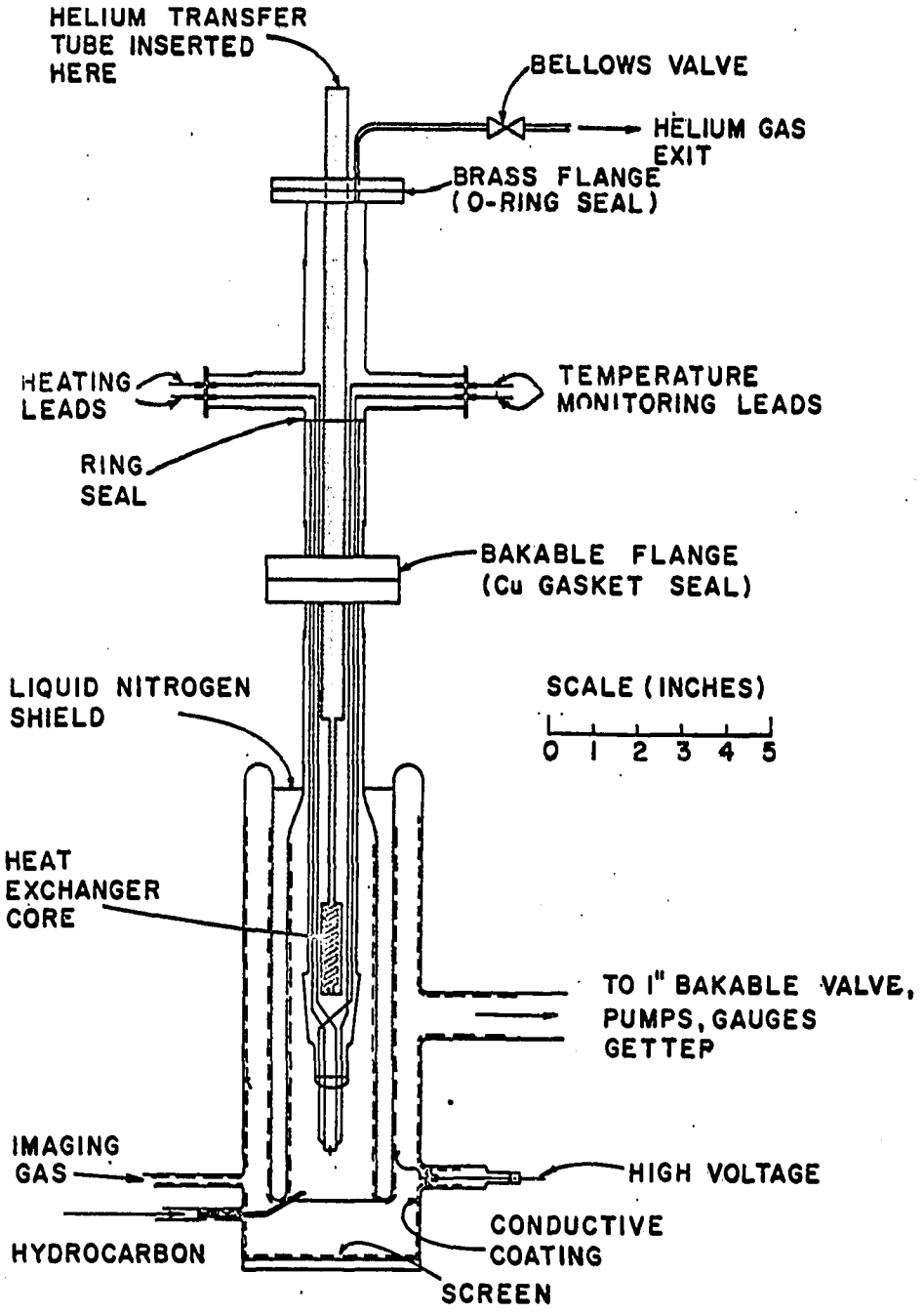

Figure 28. Schematic of field ion microscope used in present studies

Figure 29. Photograph of field ion microscopy laboratory

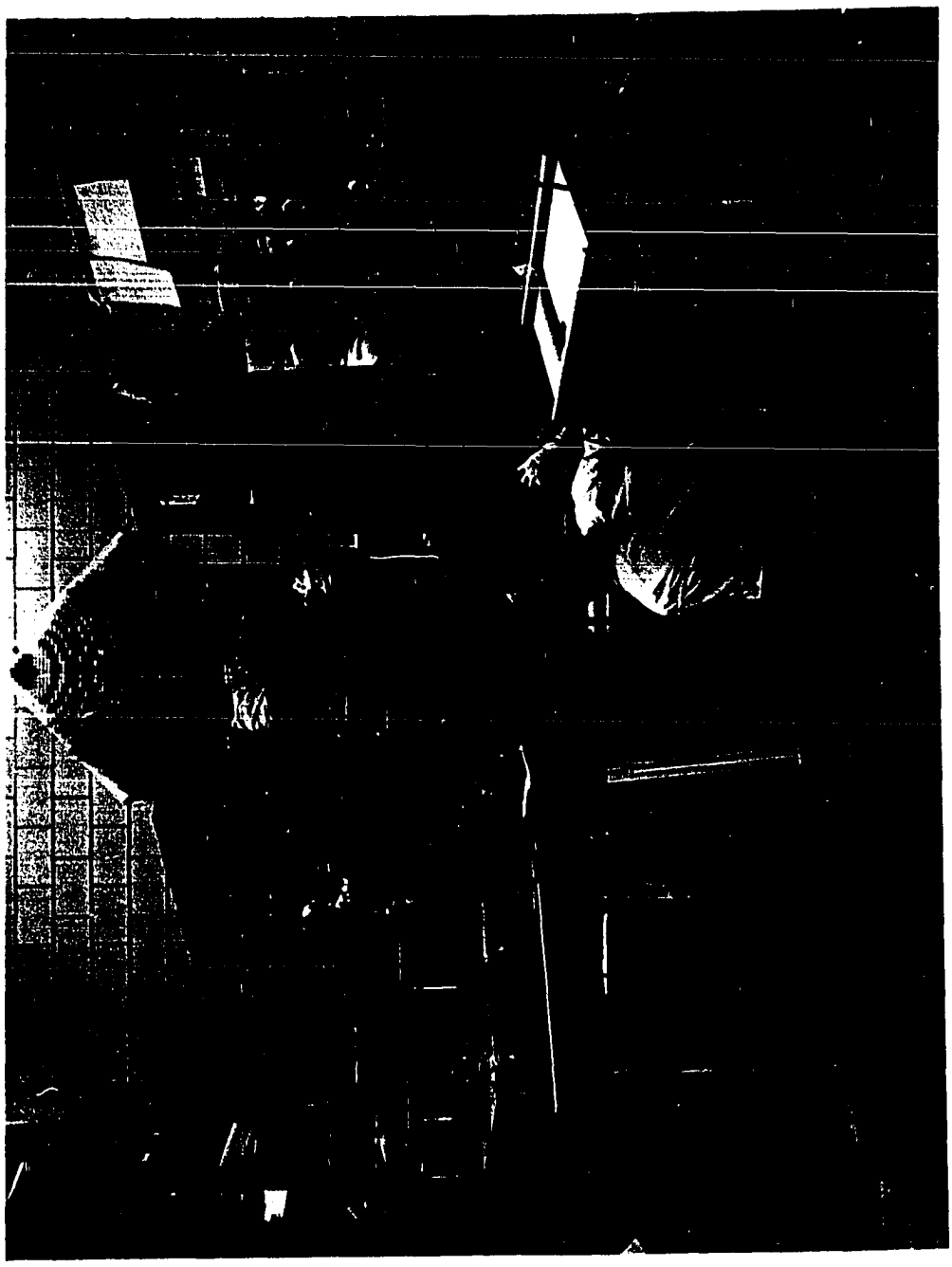

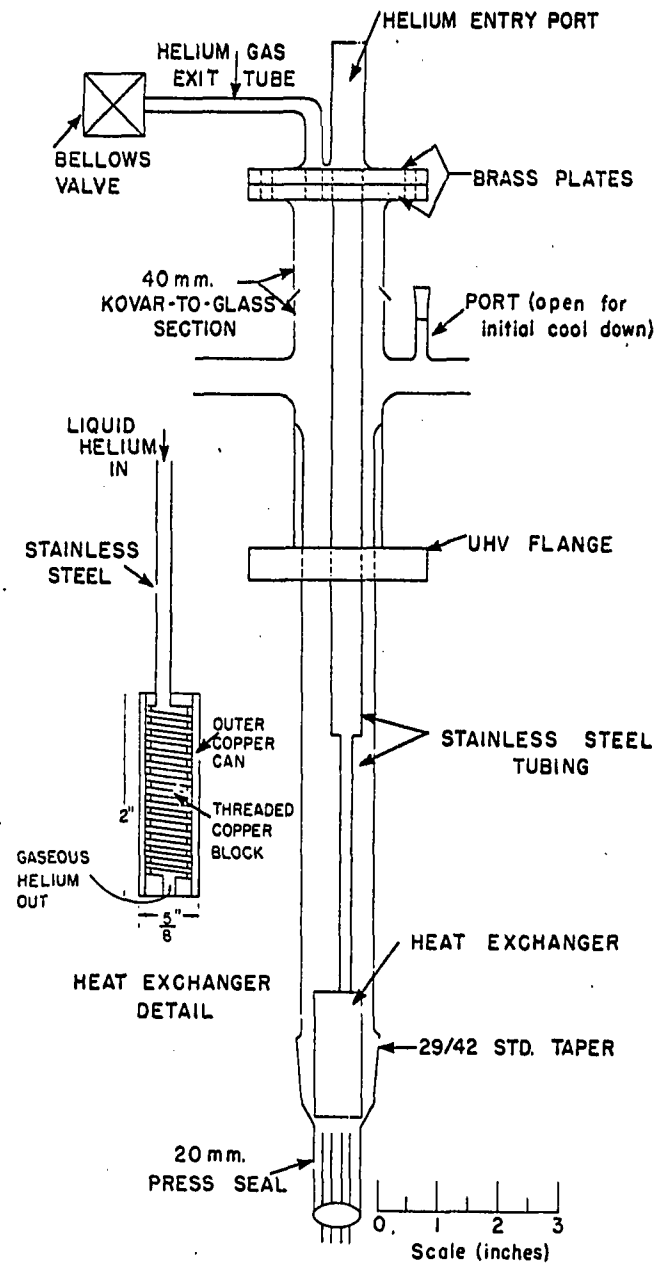

Figure 30. Heat exchanger for continuous transfer of liquid helium

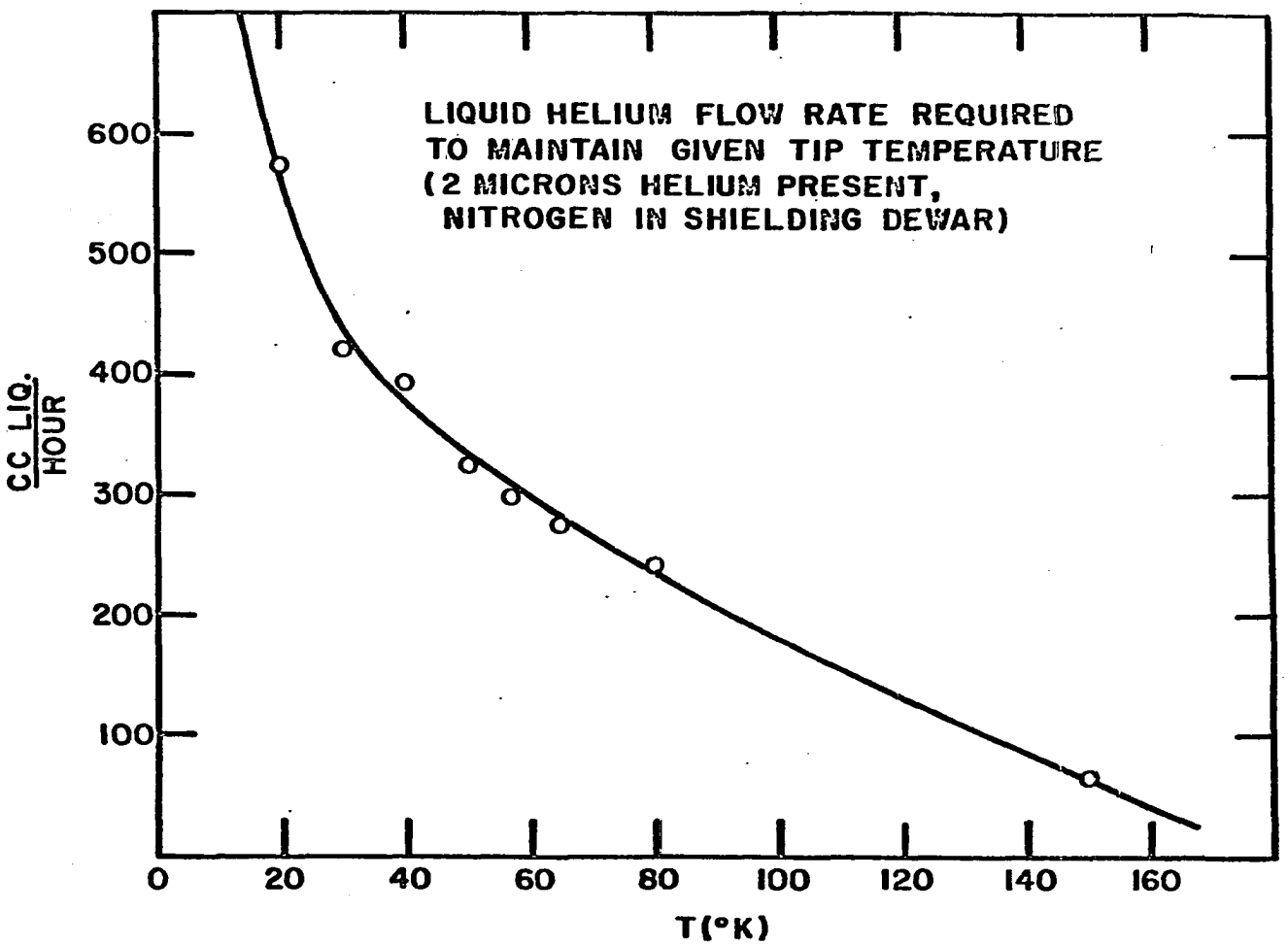

Figure 31. Liquid helium consumption required to maintain a given tip temperature

Figure 32. Helium ion micrographs of a partially field evaporated tungsten surface at temperatures between 150°K and 20°K

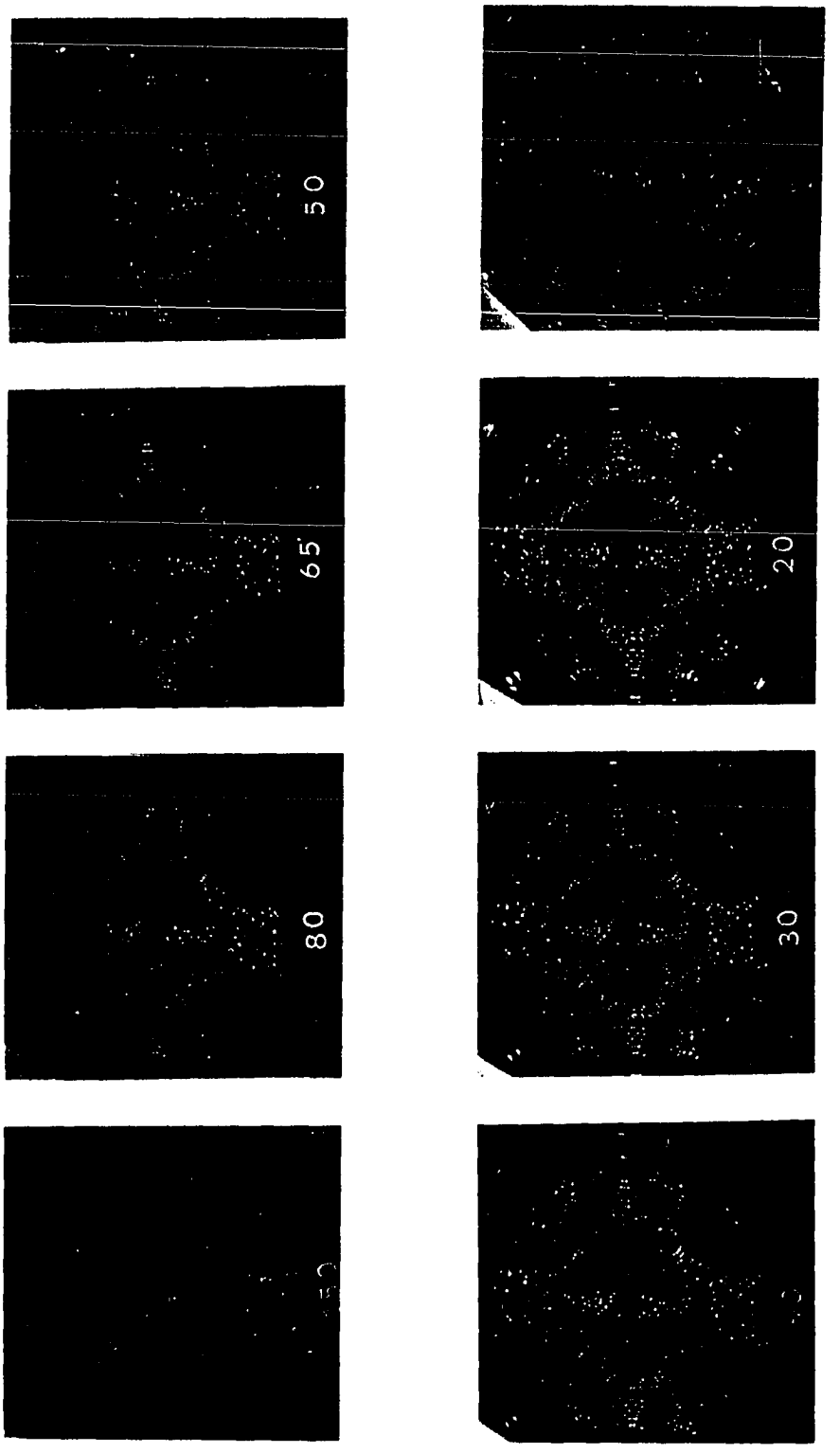
50
65
20
80
30

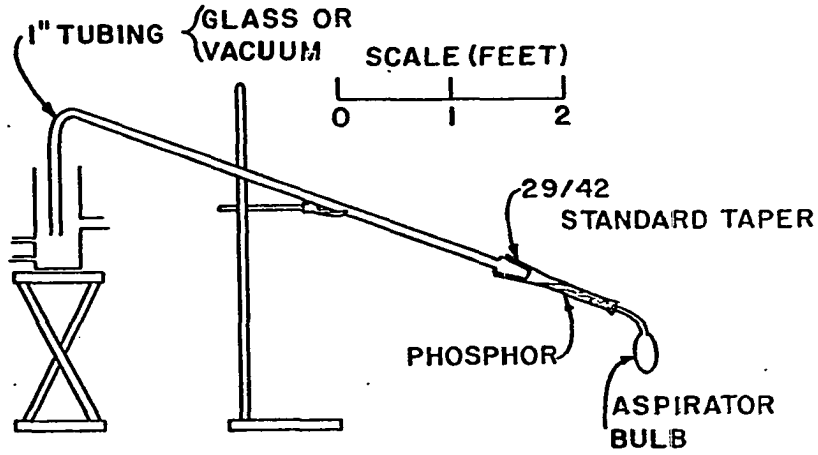

Figure 33. Puffer for depositing field ion screens

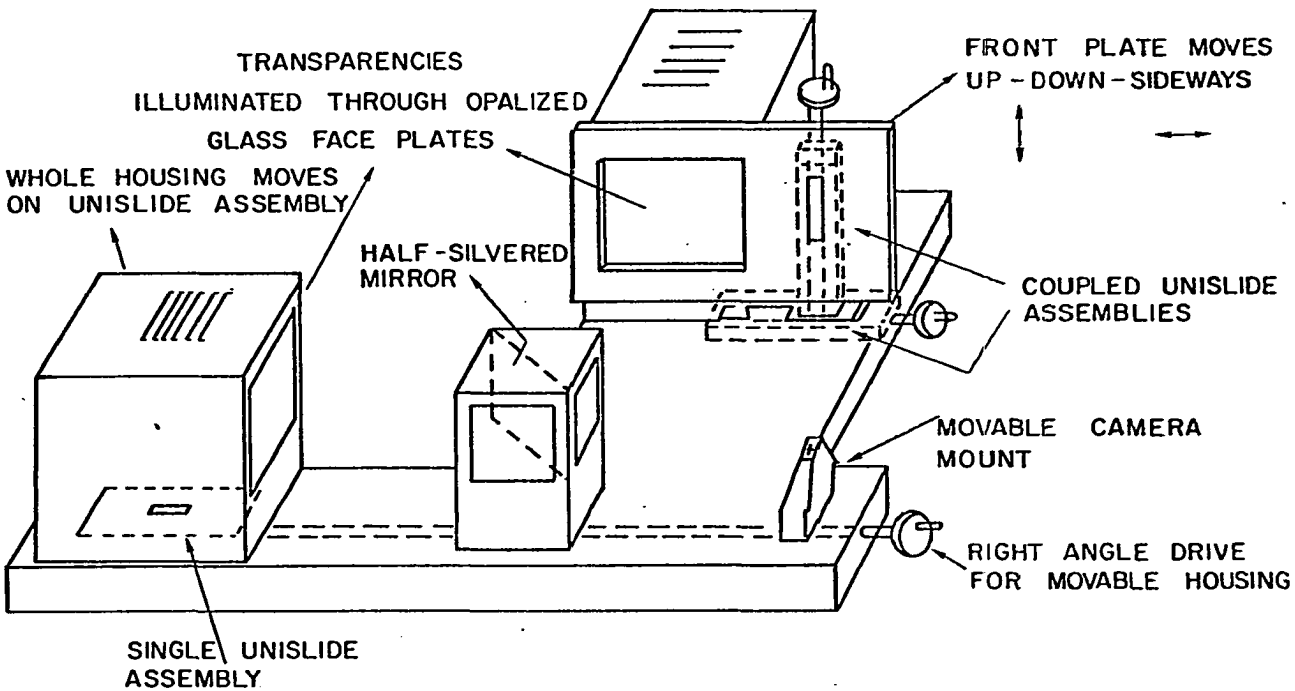

Figure 34. Field ion comparator

Figure 35. Illustration of the use of the FIM comparator

Left - clean tungsten surface
Right - after acetylene adsorption

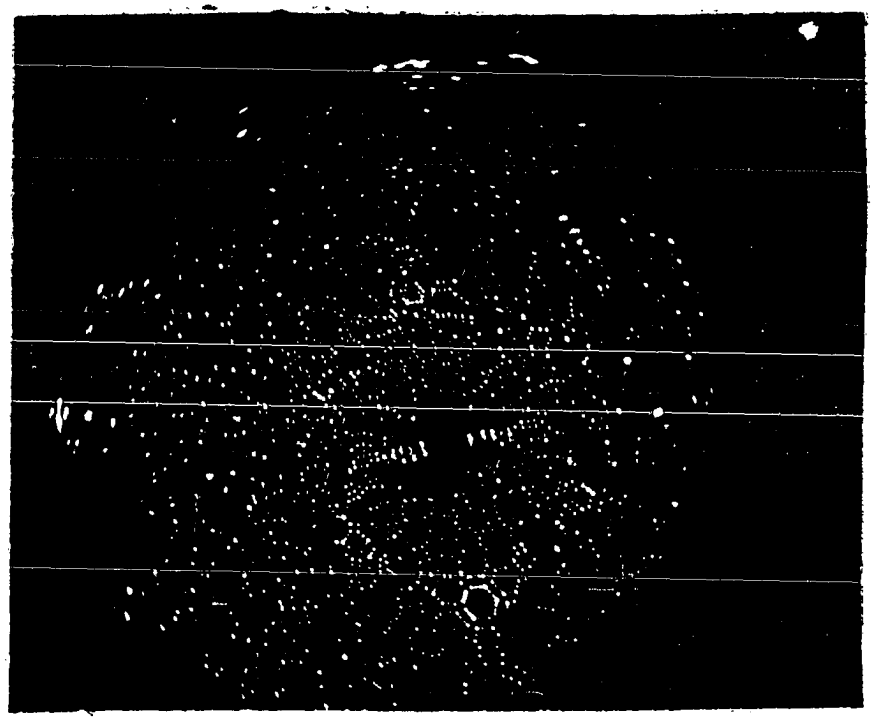

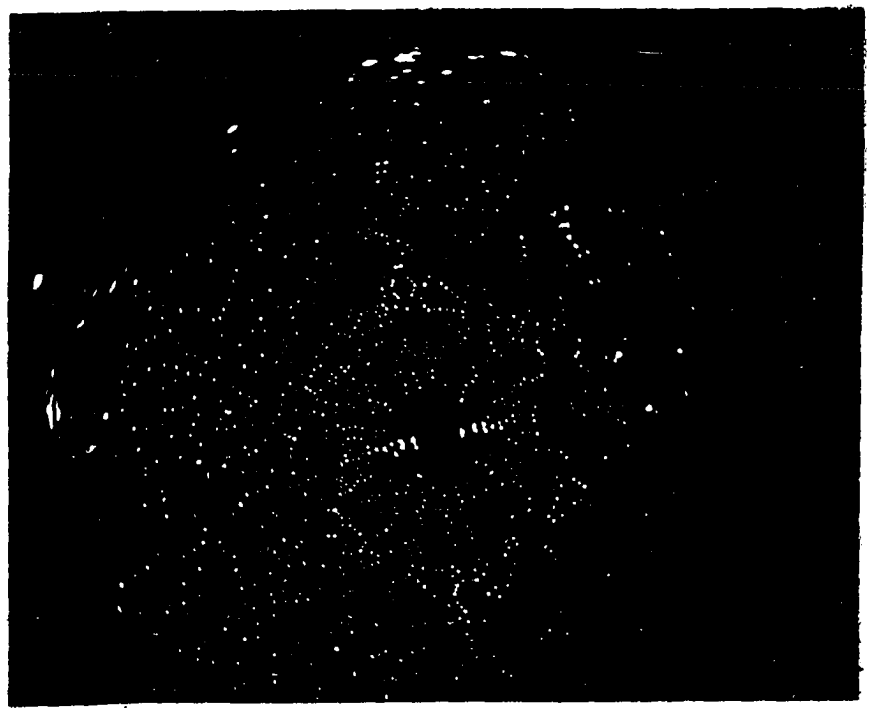

Figure 35. (Continued)

Color superposition of transparencies of previous two micrographs. Acetylene adsorption sites are indicated by the blue-green image points

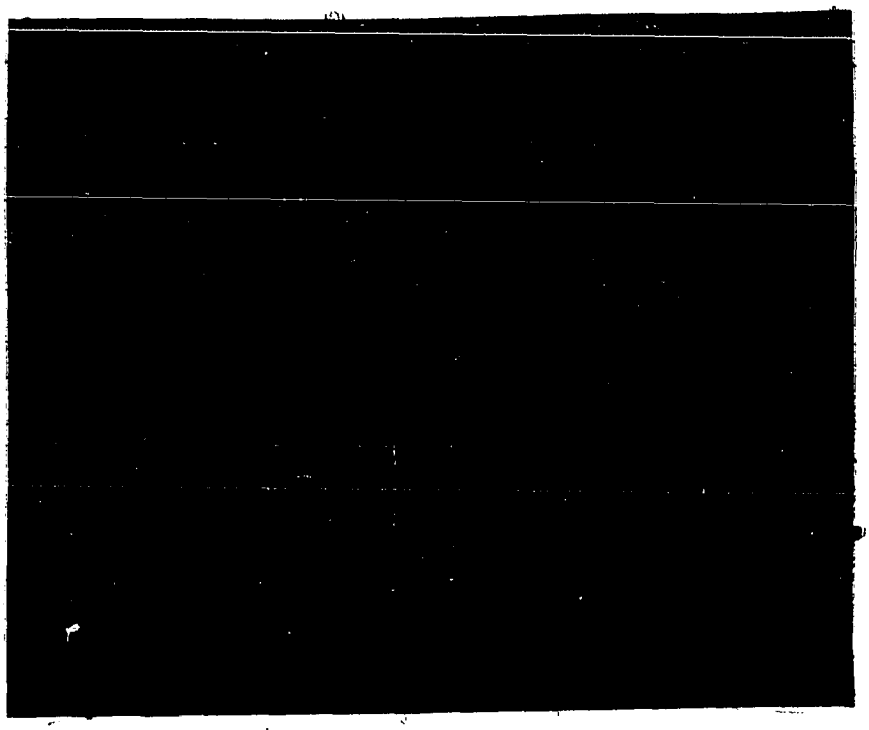

Figure 36. Liquid nitrogen cooled helium ion images

A grain boundary is visible running from lower left to upper right hand side of the micrographs

right- partially field evaporated surface
left - completely shaped tip

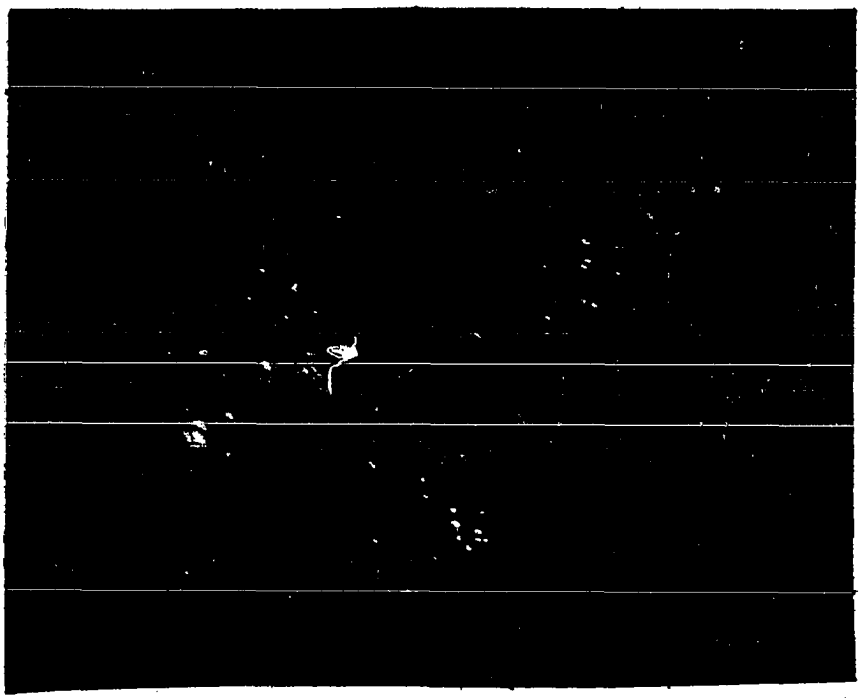

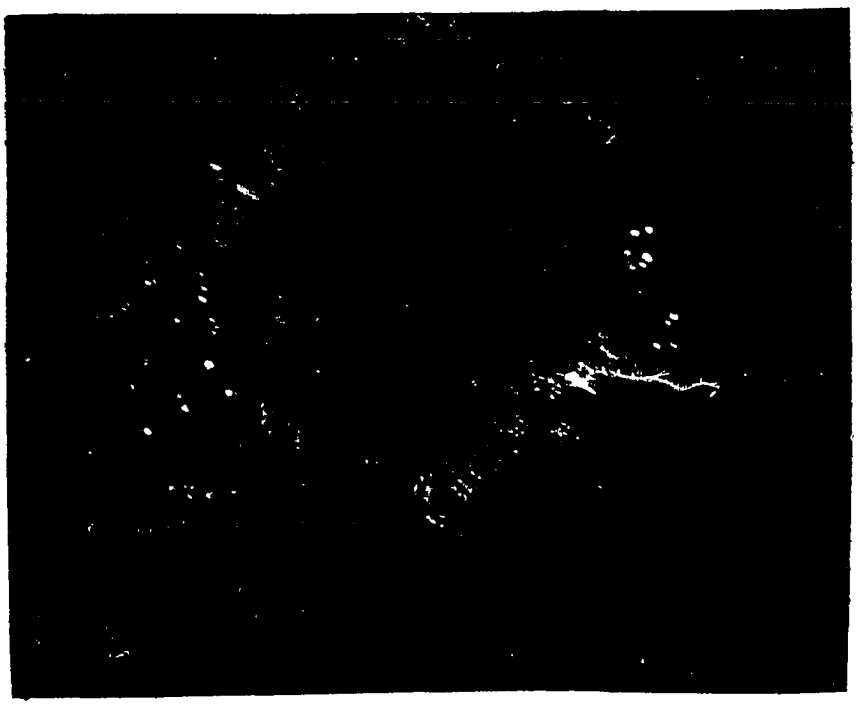

Figure 37. Further low temperature helium ion micrographs

Left - 11 atoms on (100) planes, 4 decoration atoms on (310) plane

Right - 2 decoration atoms on central (110) plane, (310) and (130) planes demonstrate 3.16Å spacings between atom rows

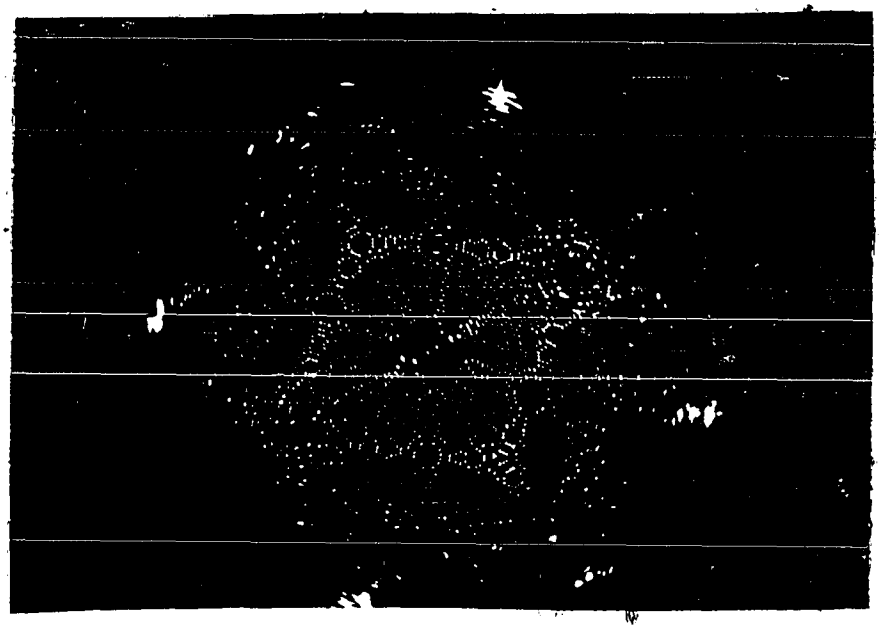

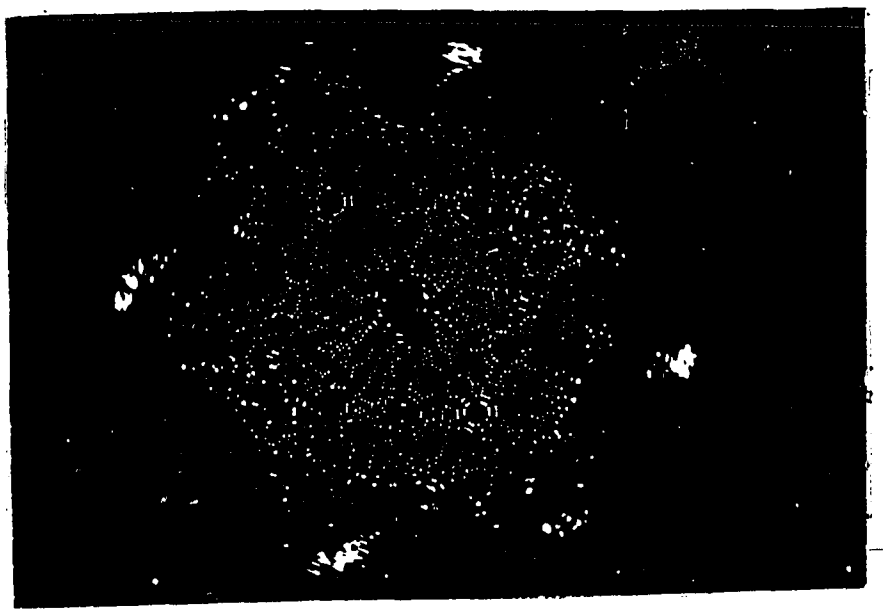

Figure 37. (Continued)

BIV for [110]-zone planes has been exceeded. The {110} planes, however, are resolved more clearly

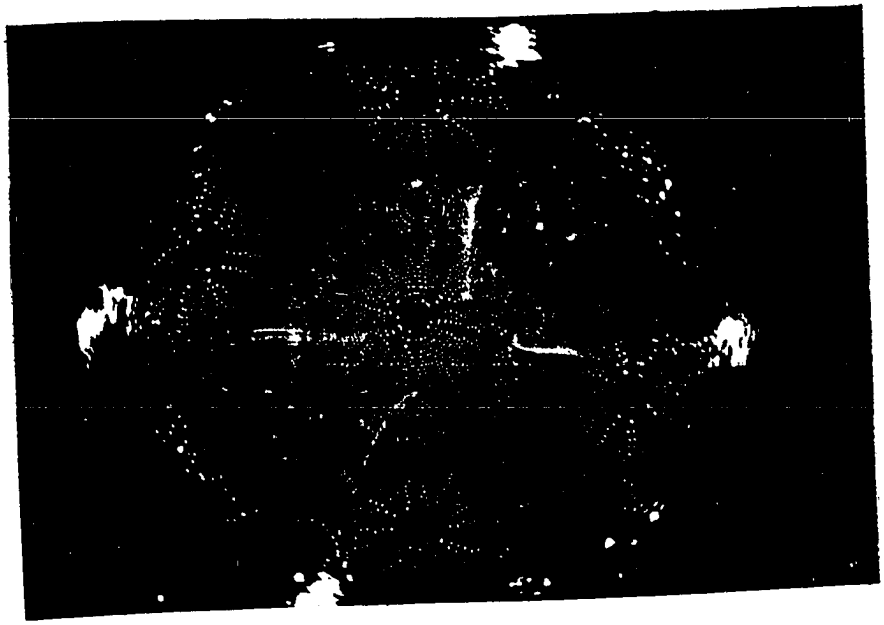

Figure 38. Further adsorption experiments in the FIM: acetylene on tungsten

left - clean surface
right - after acetylene adsorption

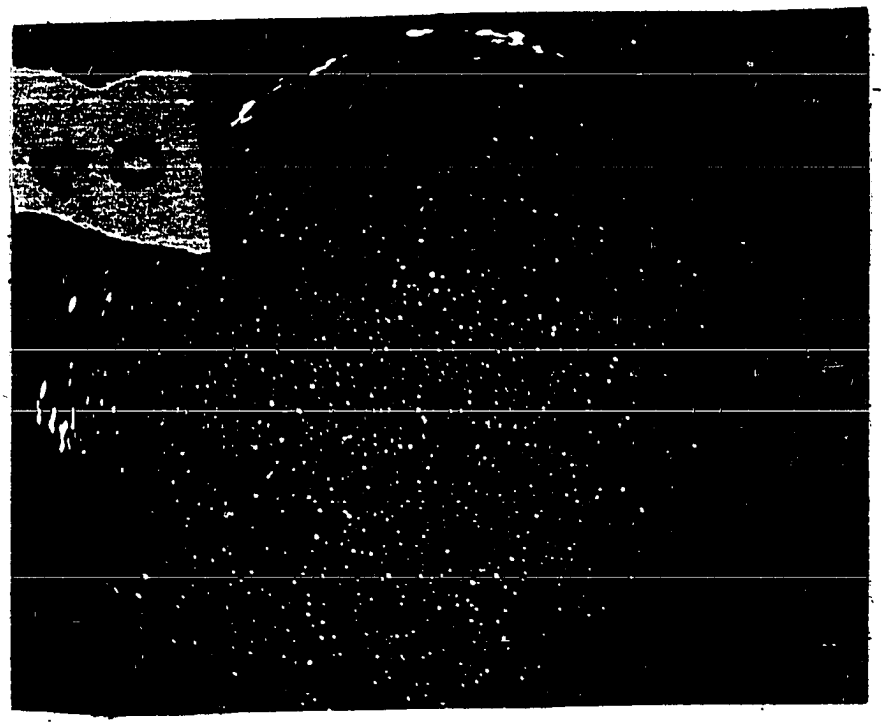

Figure 38. (Continued)

left - clean surface
right - after acetylene adsorption; a satellite image point is located inside the large circle

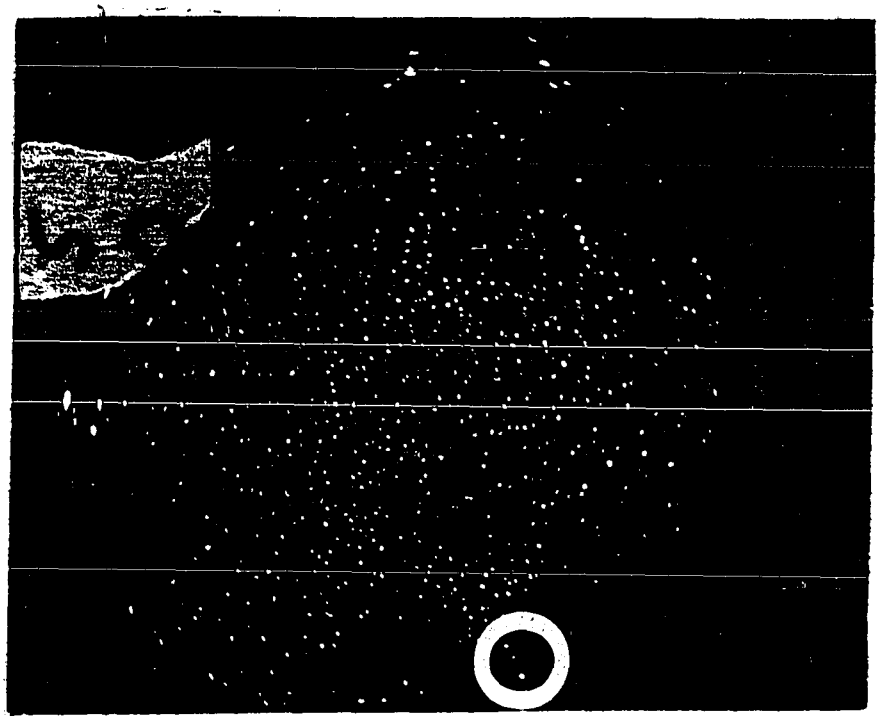

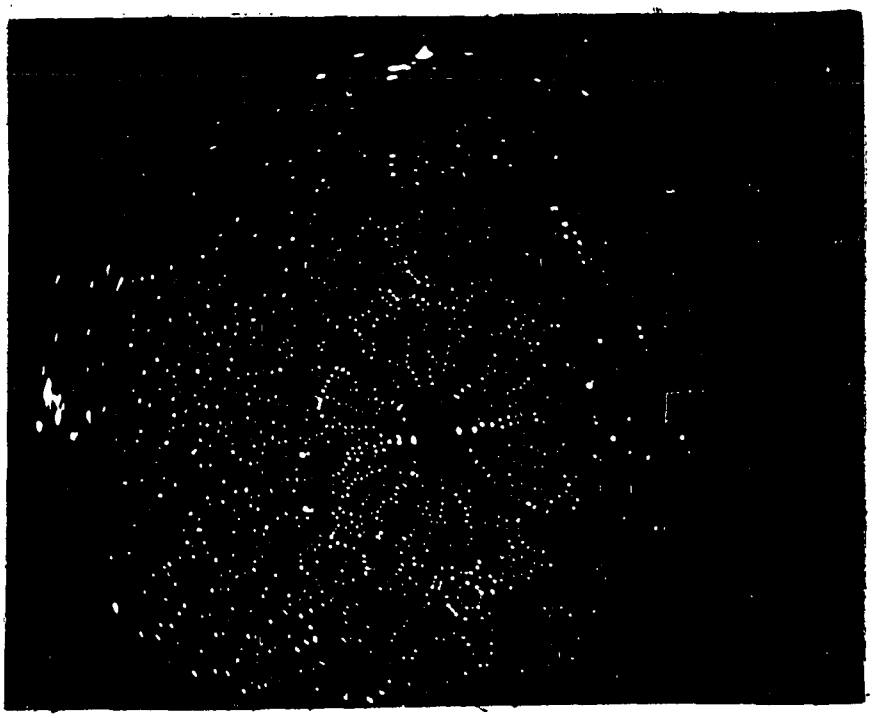

Figure 38. (Continued)

left - clean surface
right - after acetylene adsorption

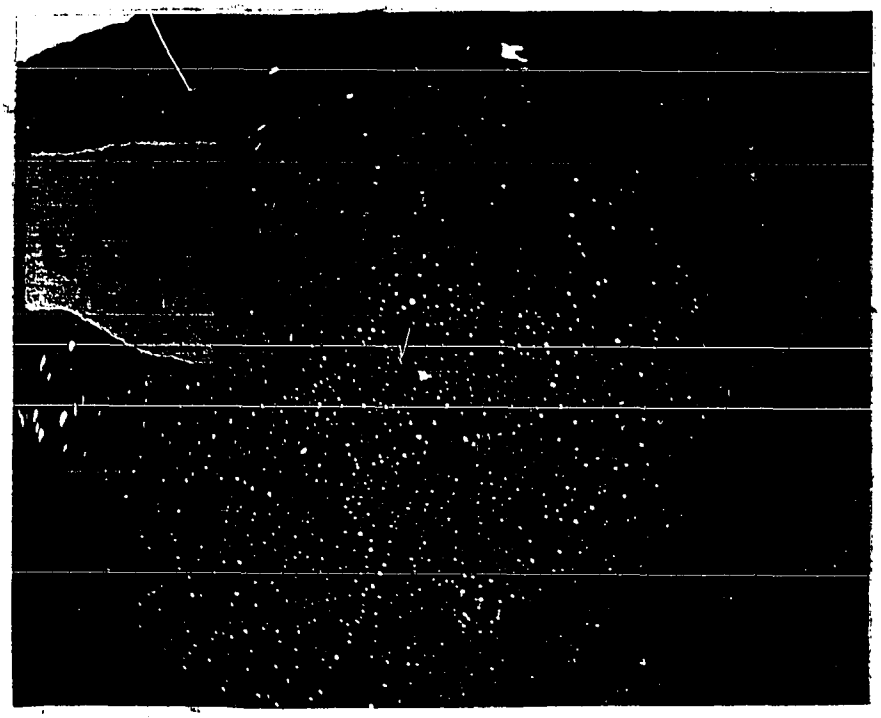

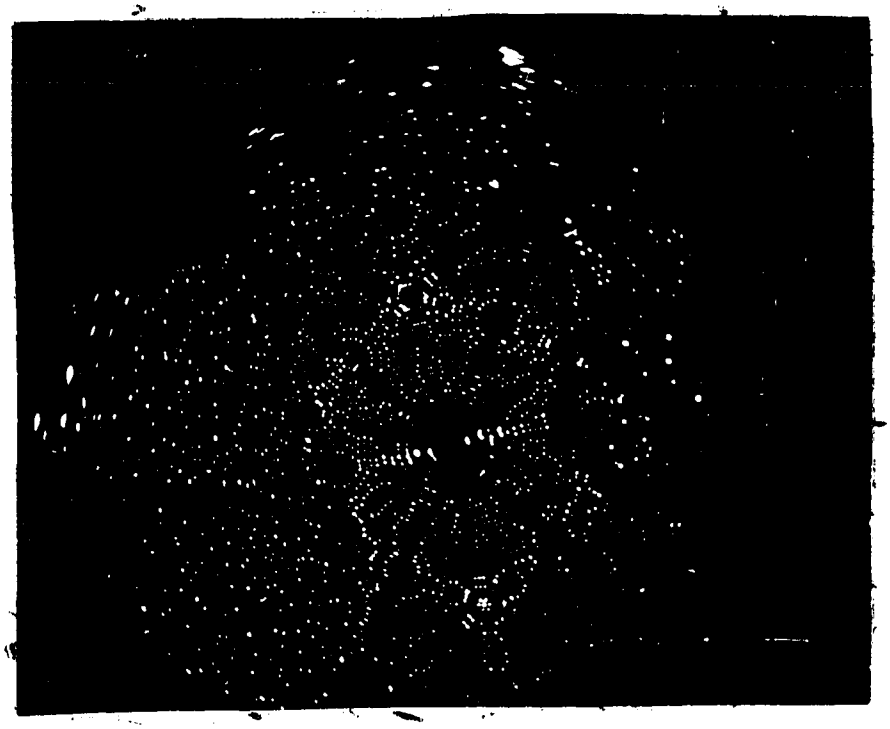

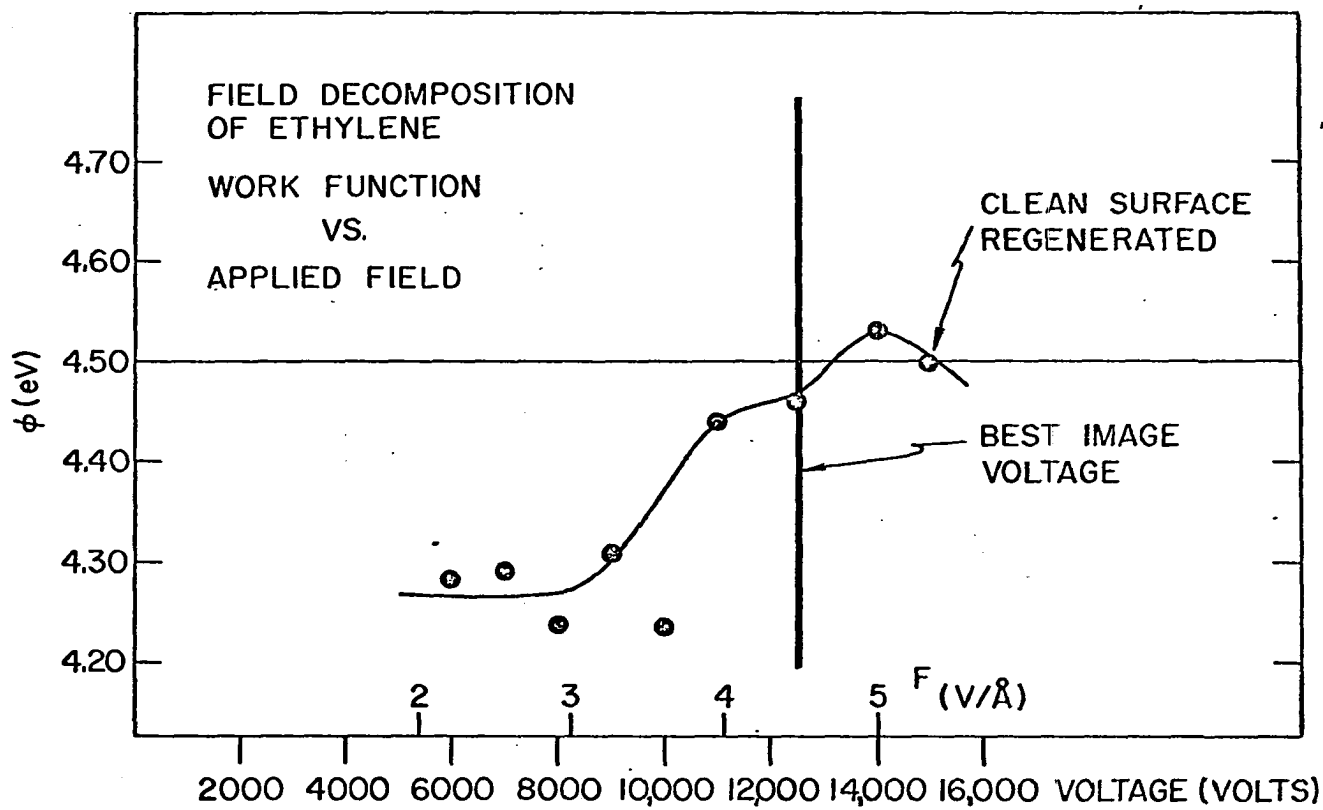

Figure 39. Field decomposition of ethylene

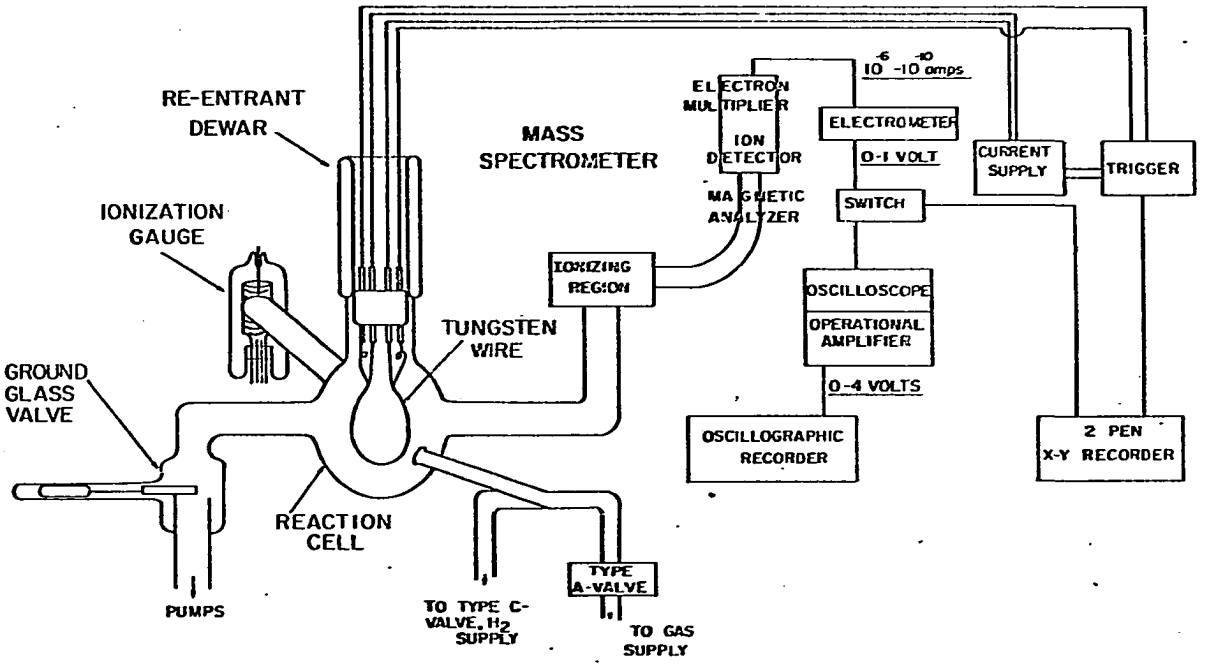

Figure 40. Flash filament spectroscopy cell with attendant electronic equipment

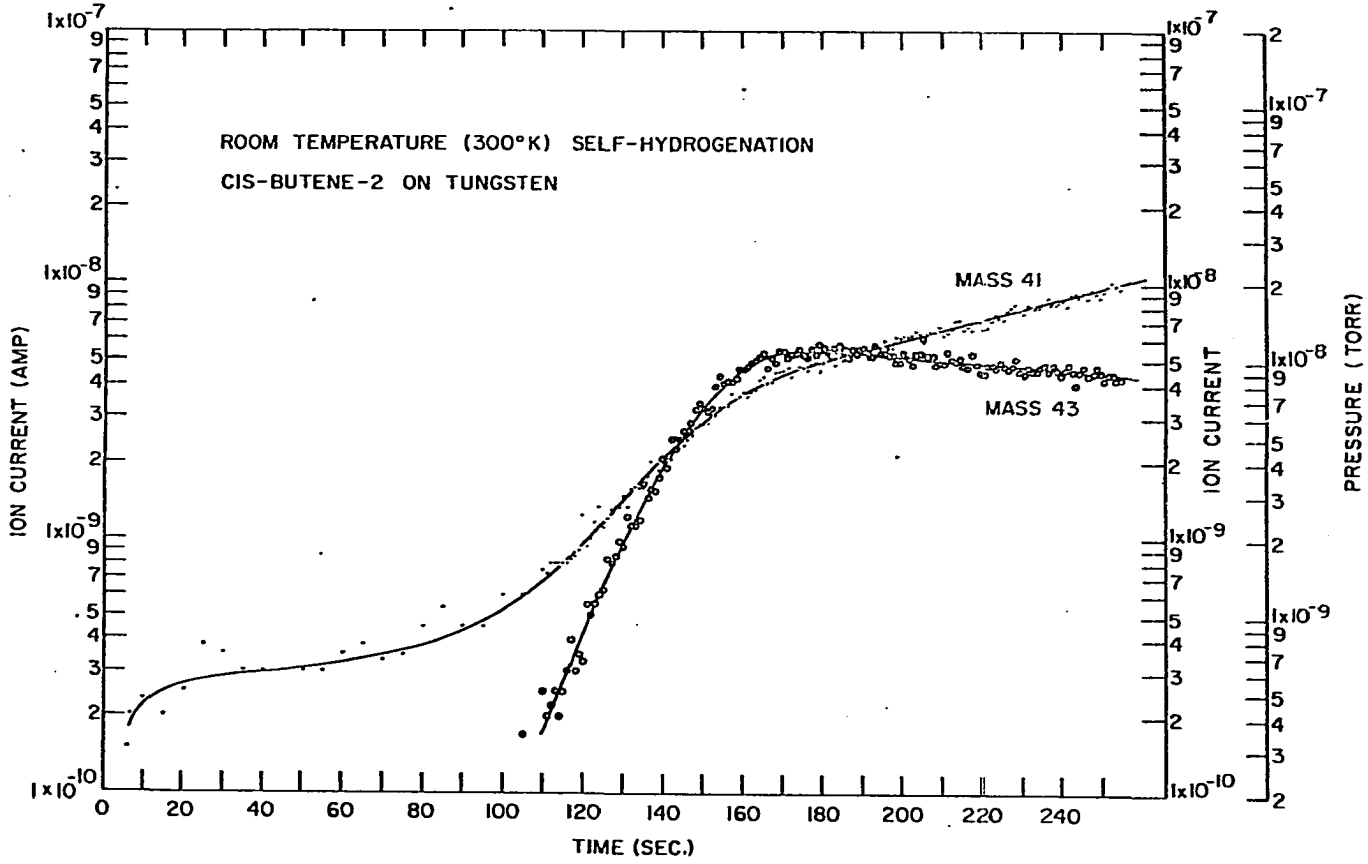

Figure 41a. Room temperature self-hydrogenation of cis-2-butene on tungsten. Relatively slow gas admission rate

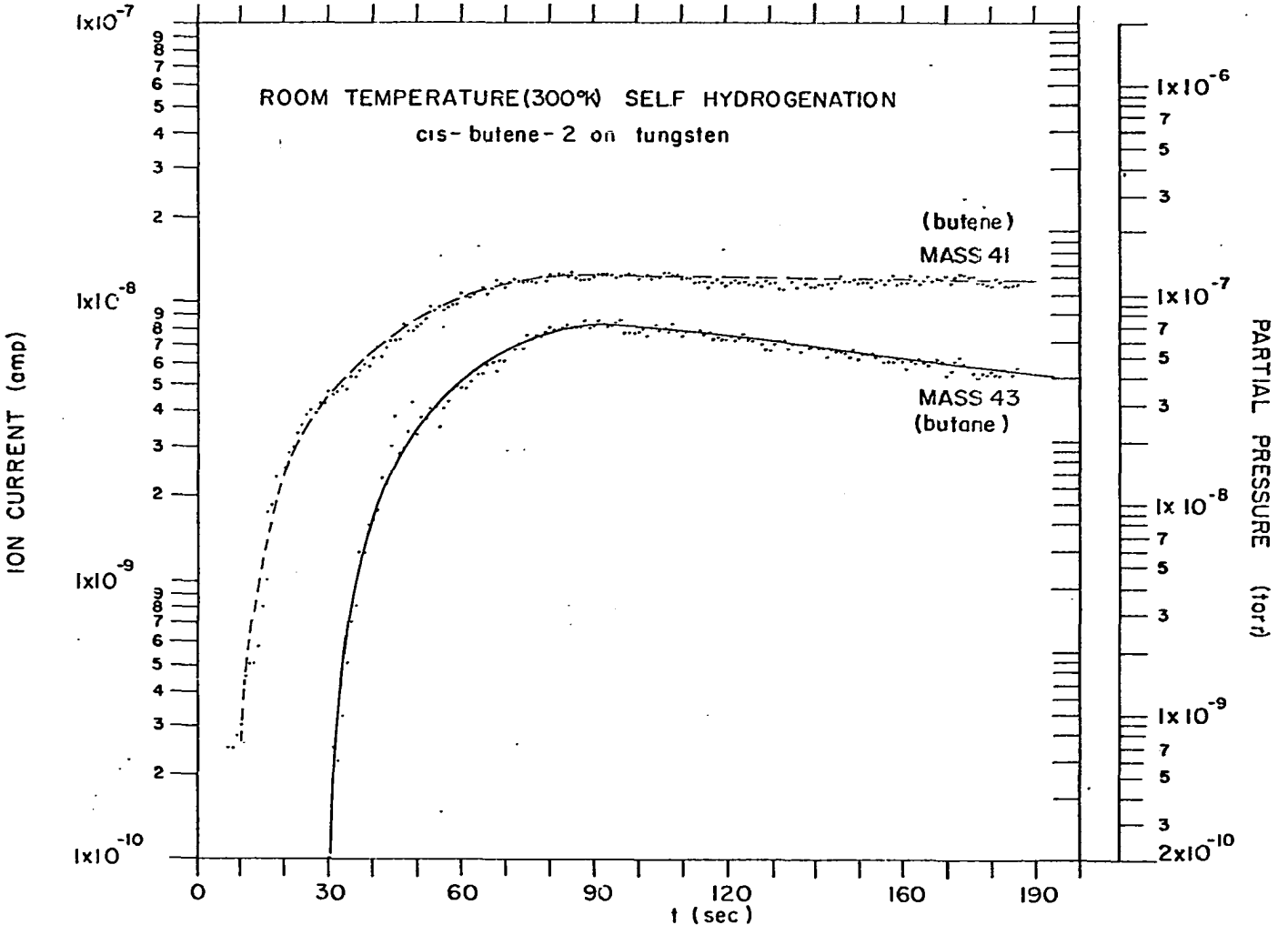

Figure 41b. Room temperature self-hydrogenation of cis-2-butene on tungsten. Faster gas admission rate

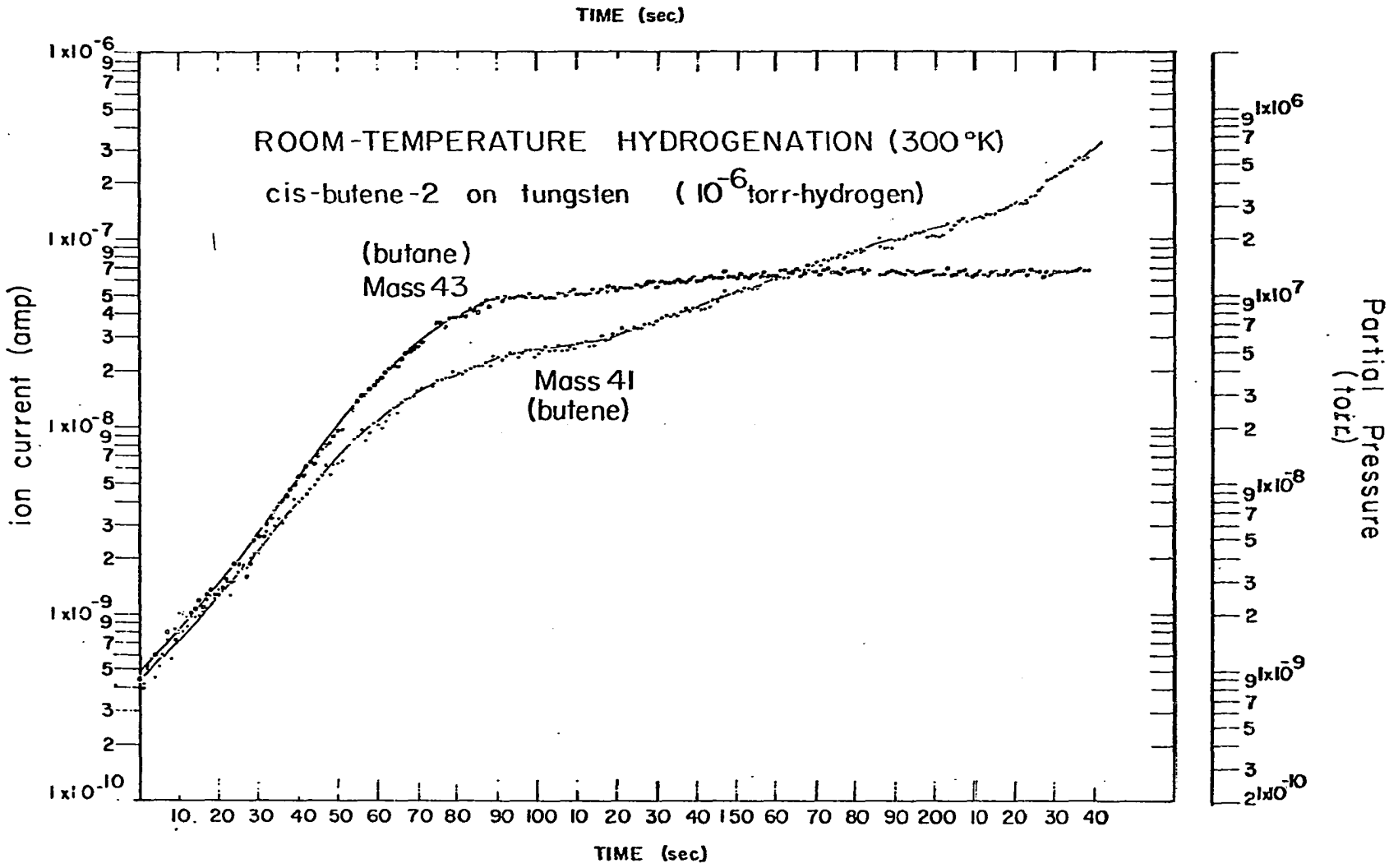

Figure 42. Room temperature hydrogenation (300°K) of cis-2-butene on tungsten in the presence of 10^{-6} torr hydrogen

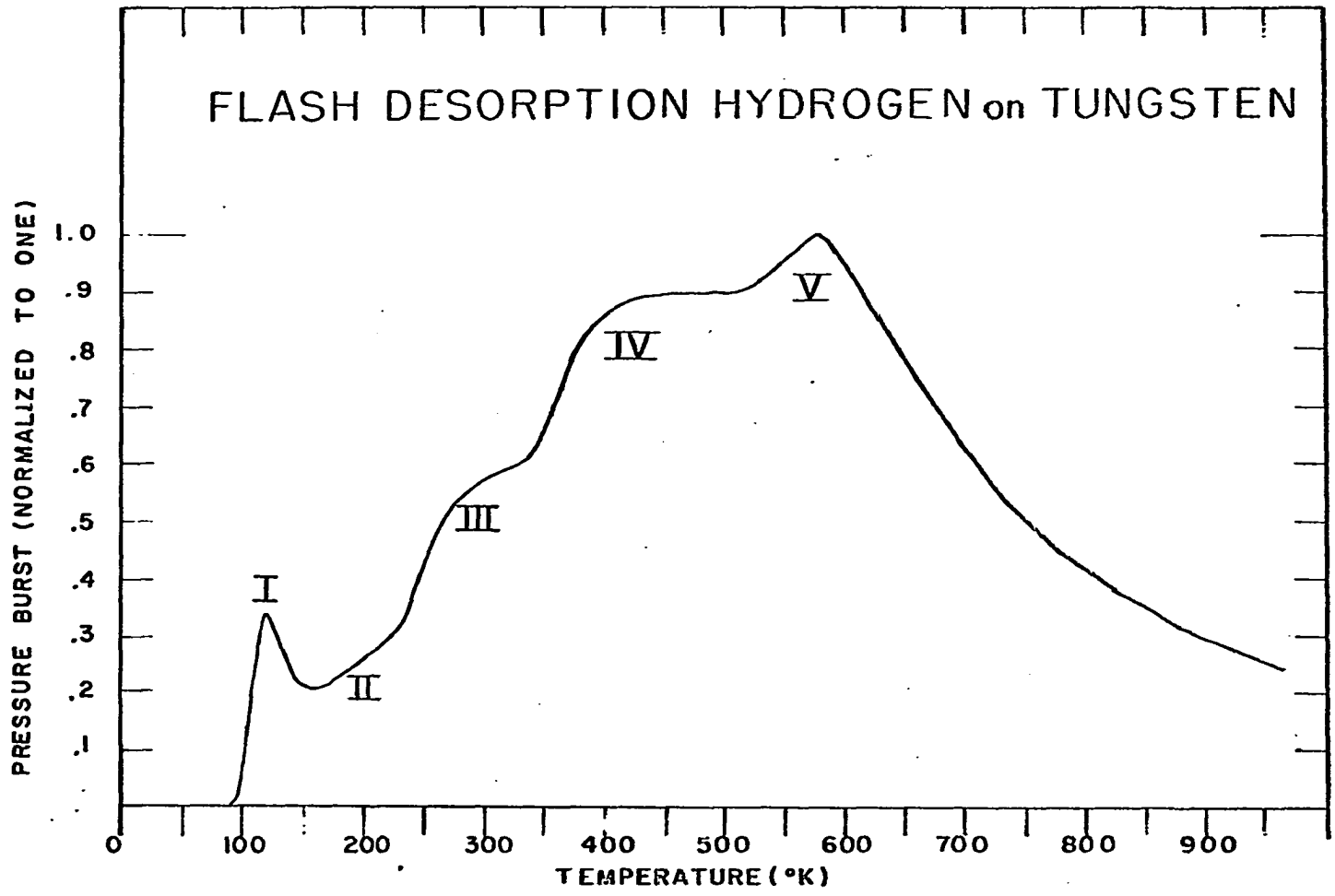

Figure 43. Flash desorption of hydrogen on tungsten. Adsorption at 95°K

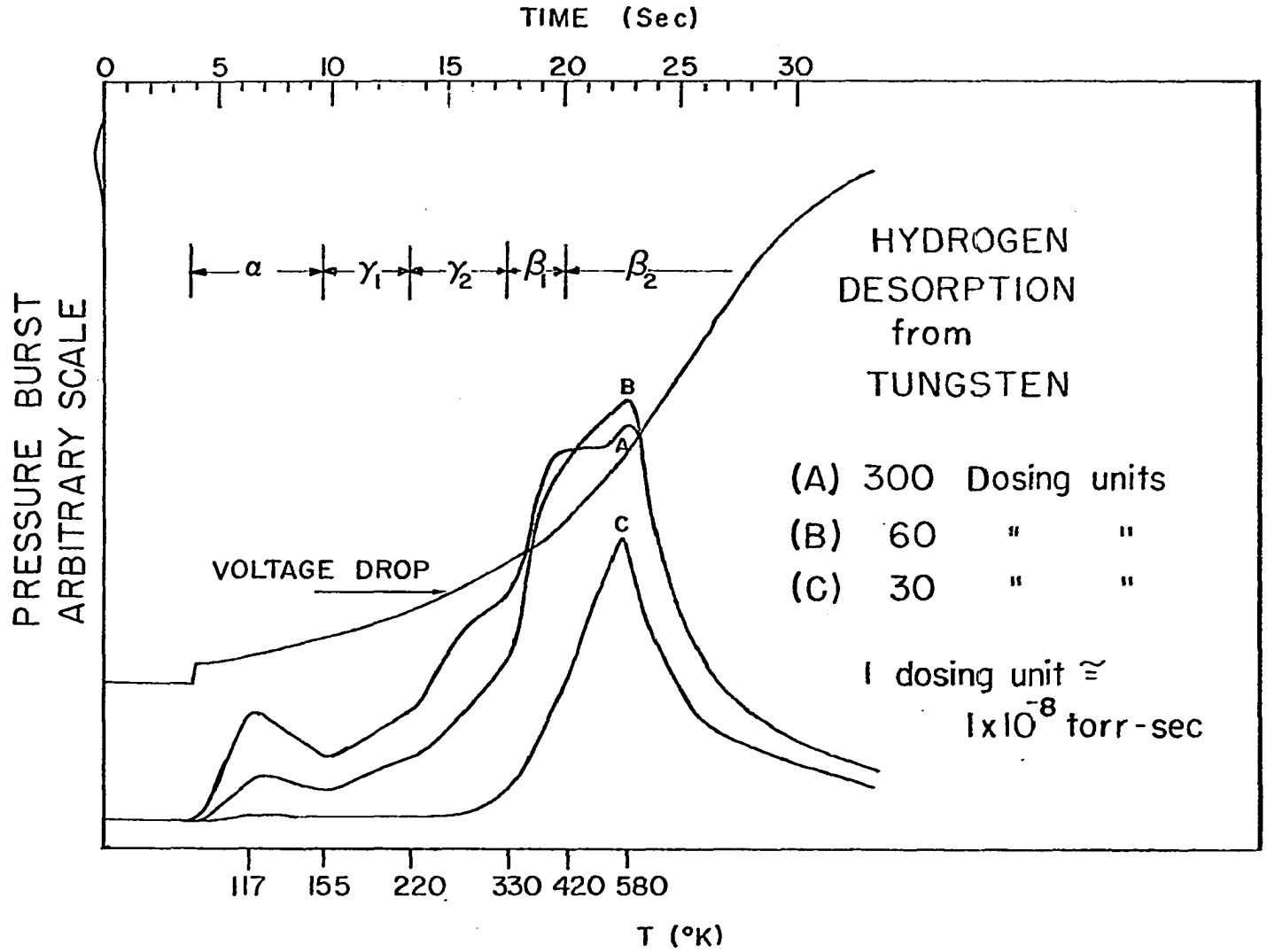

Figure 44. Hydrogen desorption from tungsten as a function of coverage

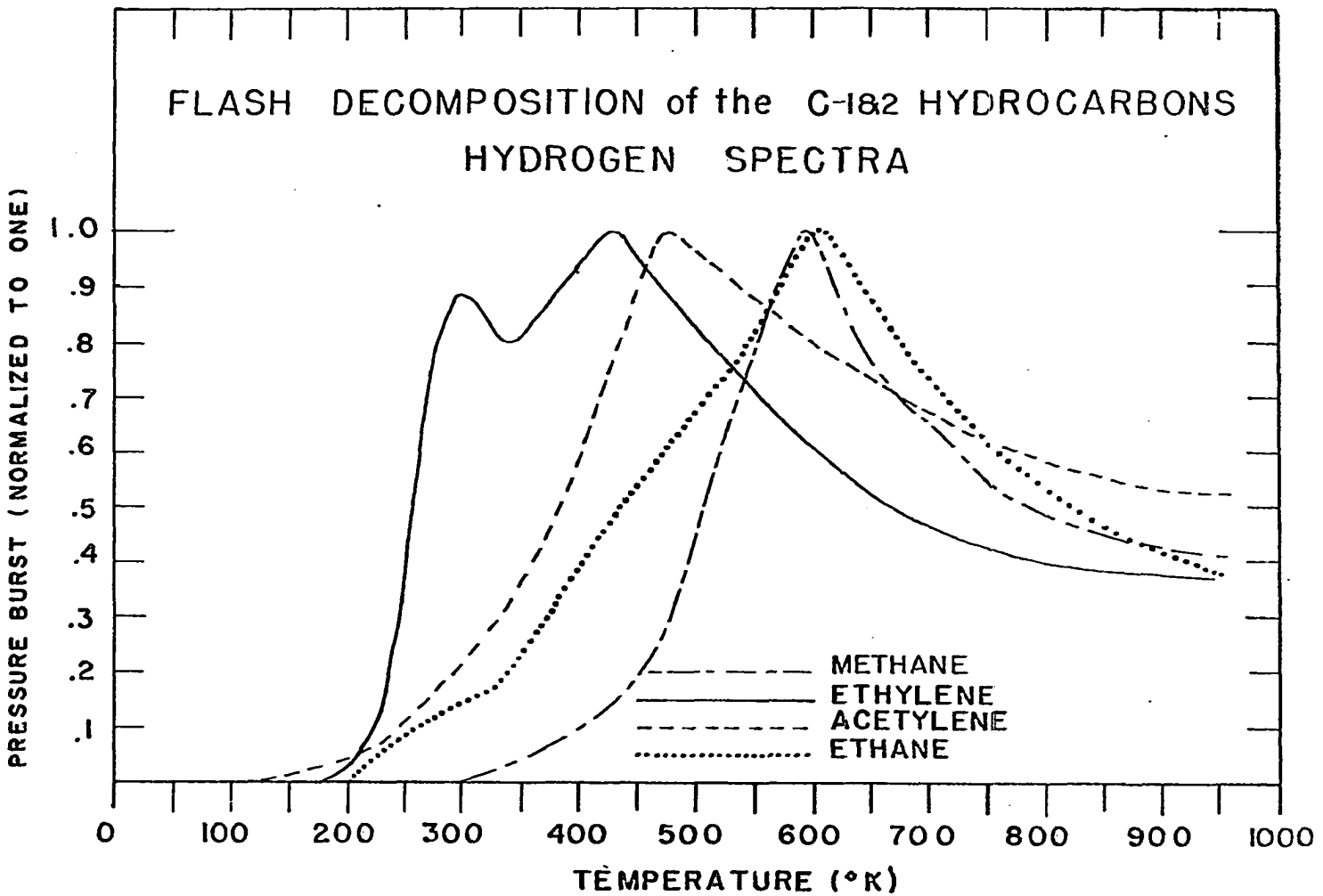

Figure 45. Flash decomposition of the C_1 and C_2 hydrocarbons. Adsorption at 95°K. Methane, ethane, ethylene, acetylene

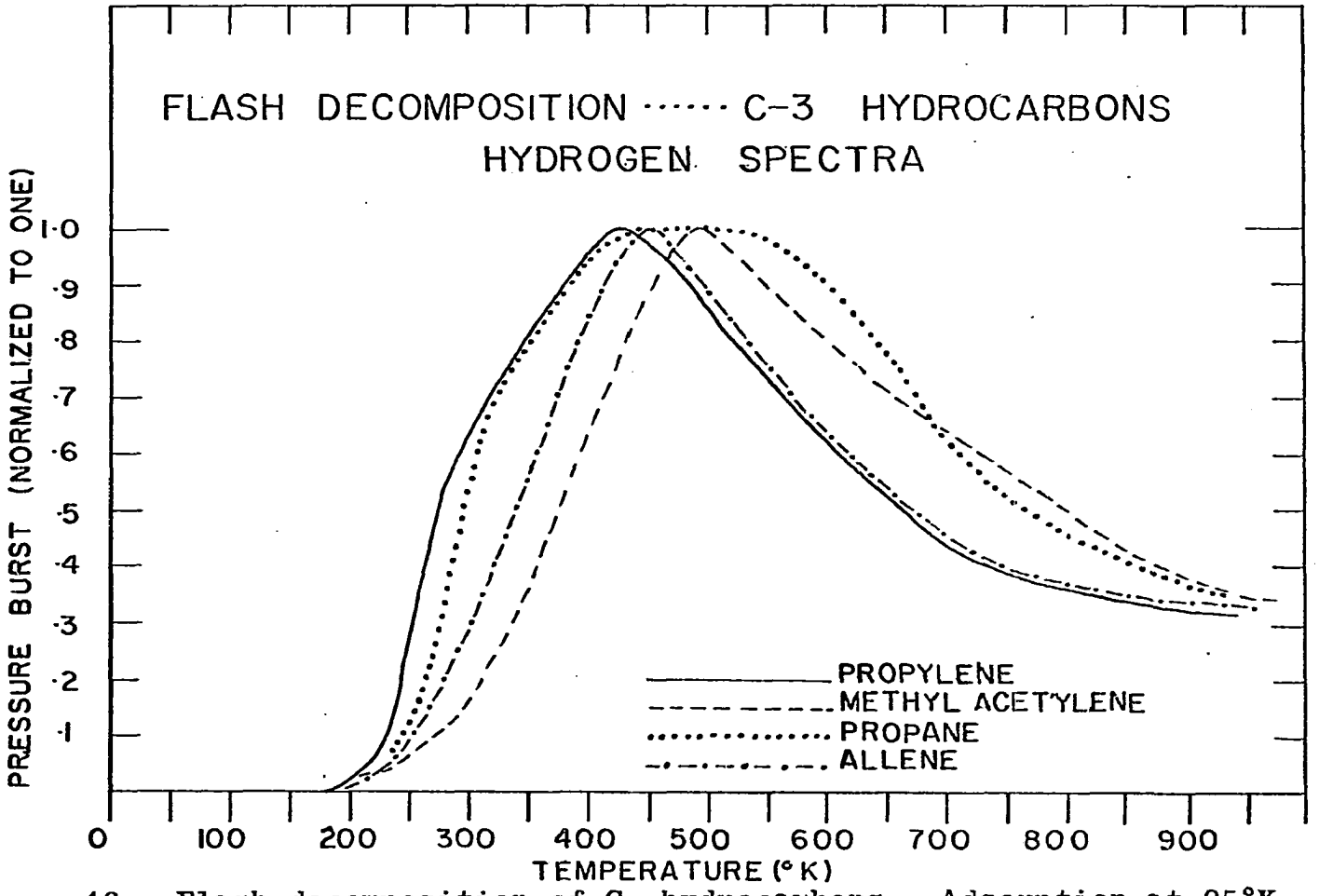

Figure 46. Flash decomposition of C_3 hydrocarbons. Adsorption at 95°K. Propane, propylene, methyl acetylene, allene

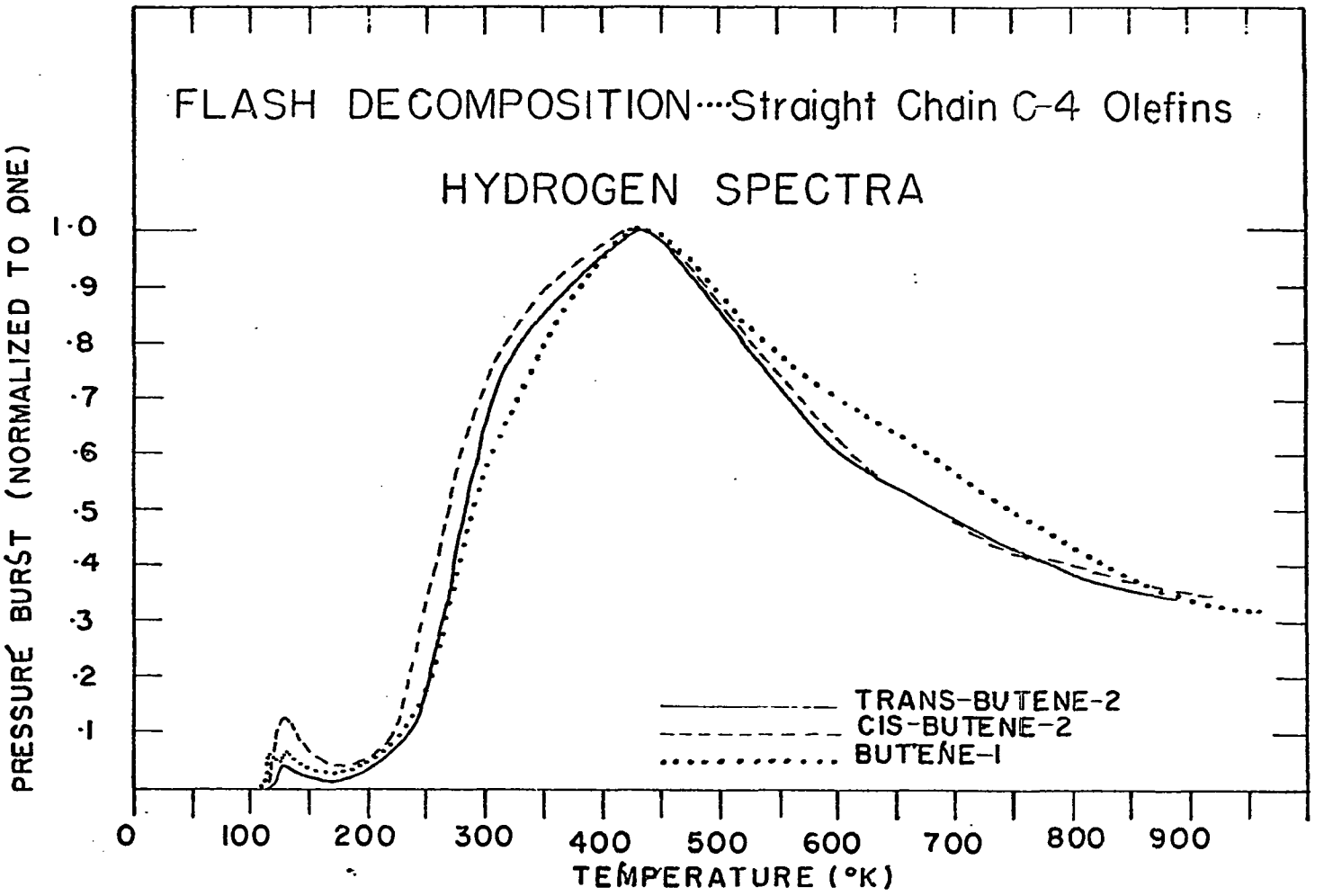

Figure 47. Flash decomposition of straight chain C_4 olefins. Adsorption at 95°K trans-2-butene, cis-2-butena and 1-butene

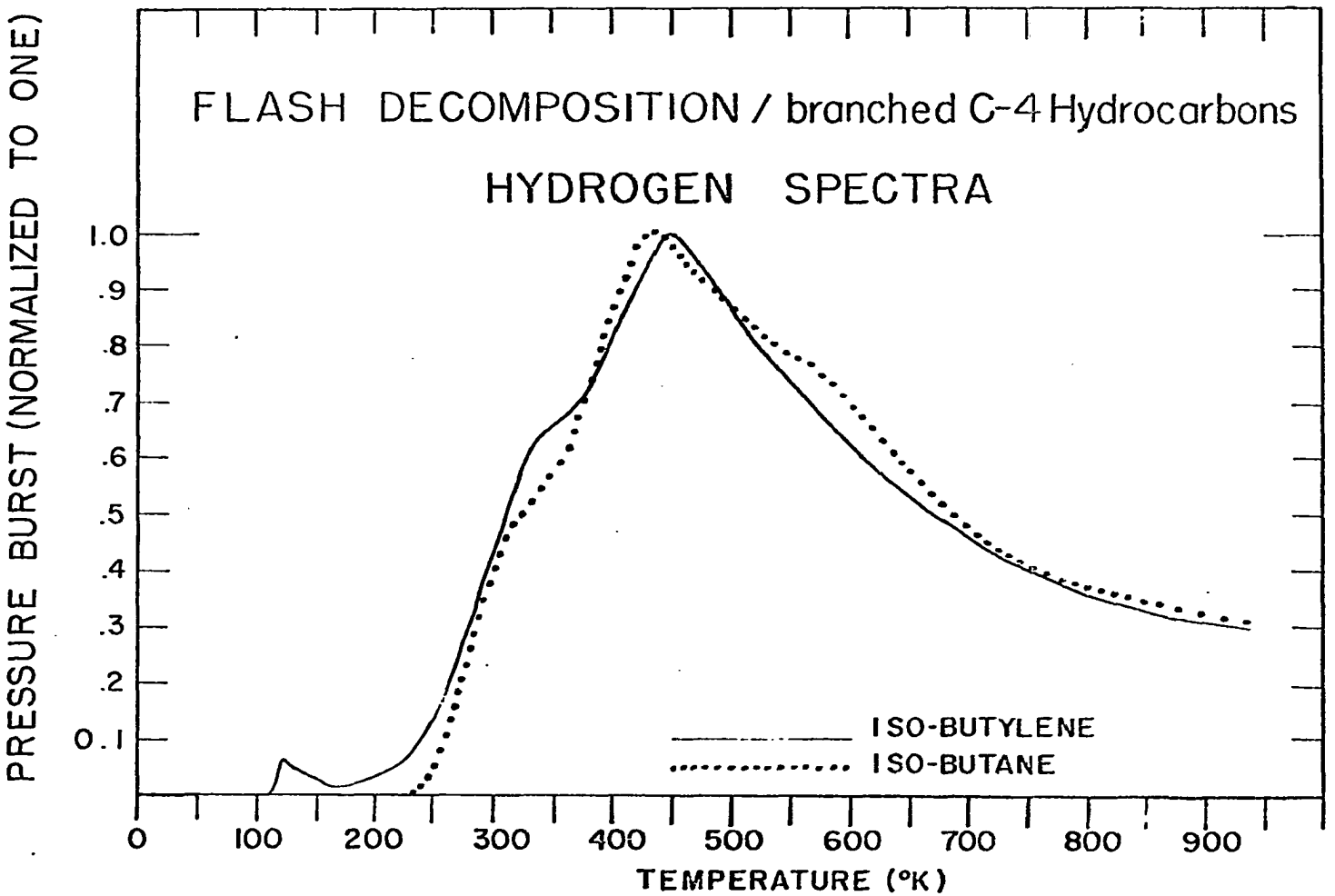

Figure 48. Flash decomposition of branch-chain C_4 hydrocarbons. Adsorption at 95°K. iso-butylene, iso-butane

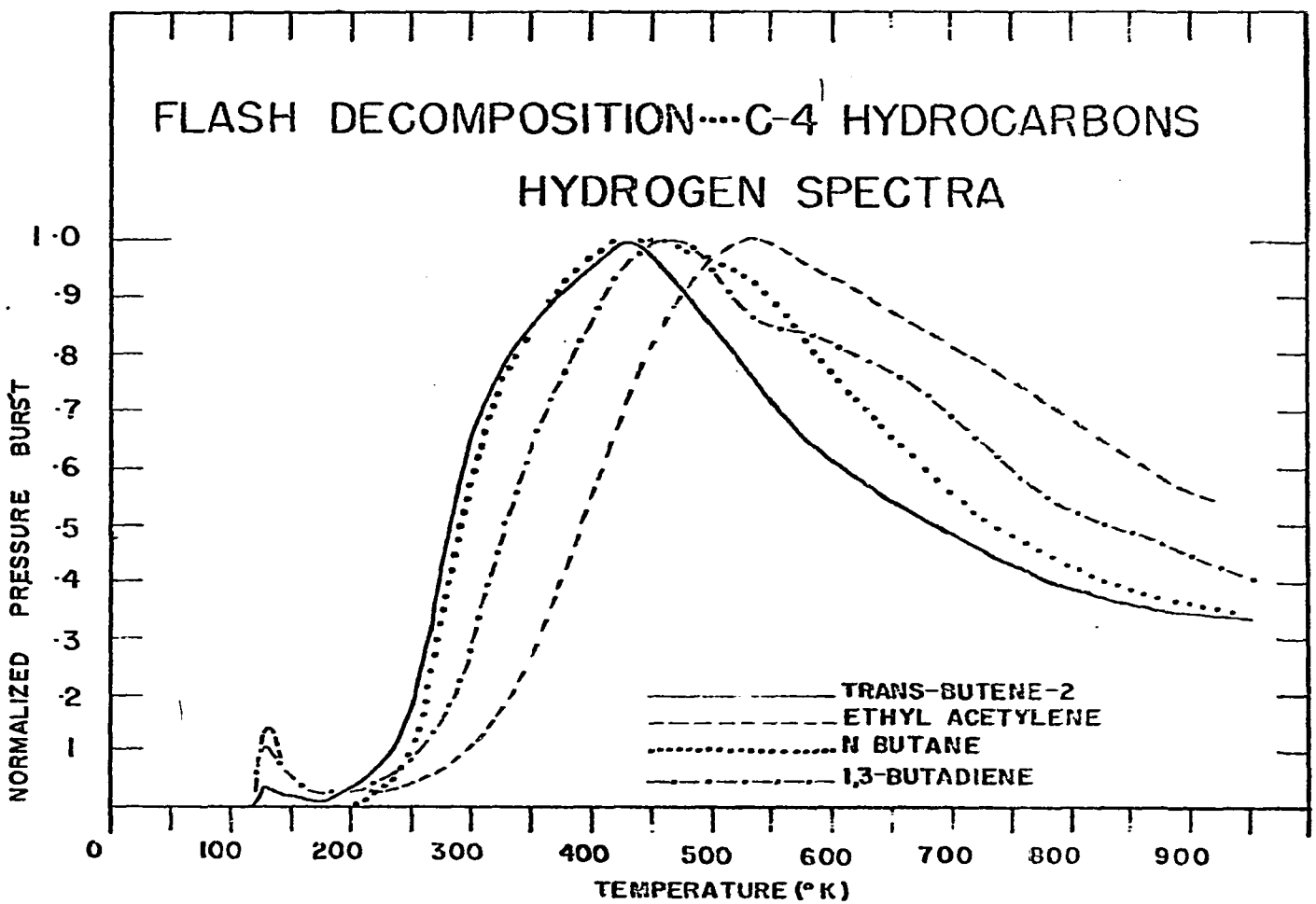

Figure 49. Flash decomposition of C_4 hydrocarbons. Adsorption at 95°K. trans-2-butene, ethyl acetylene, n-butane, 1,3-butadiene

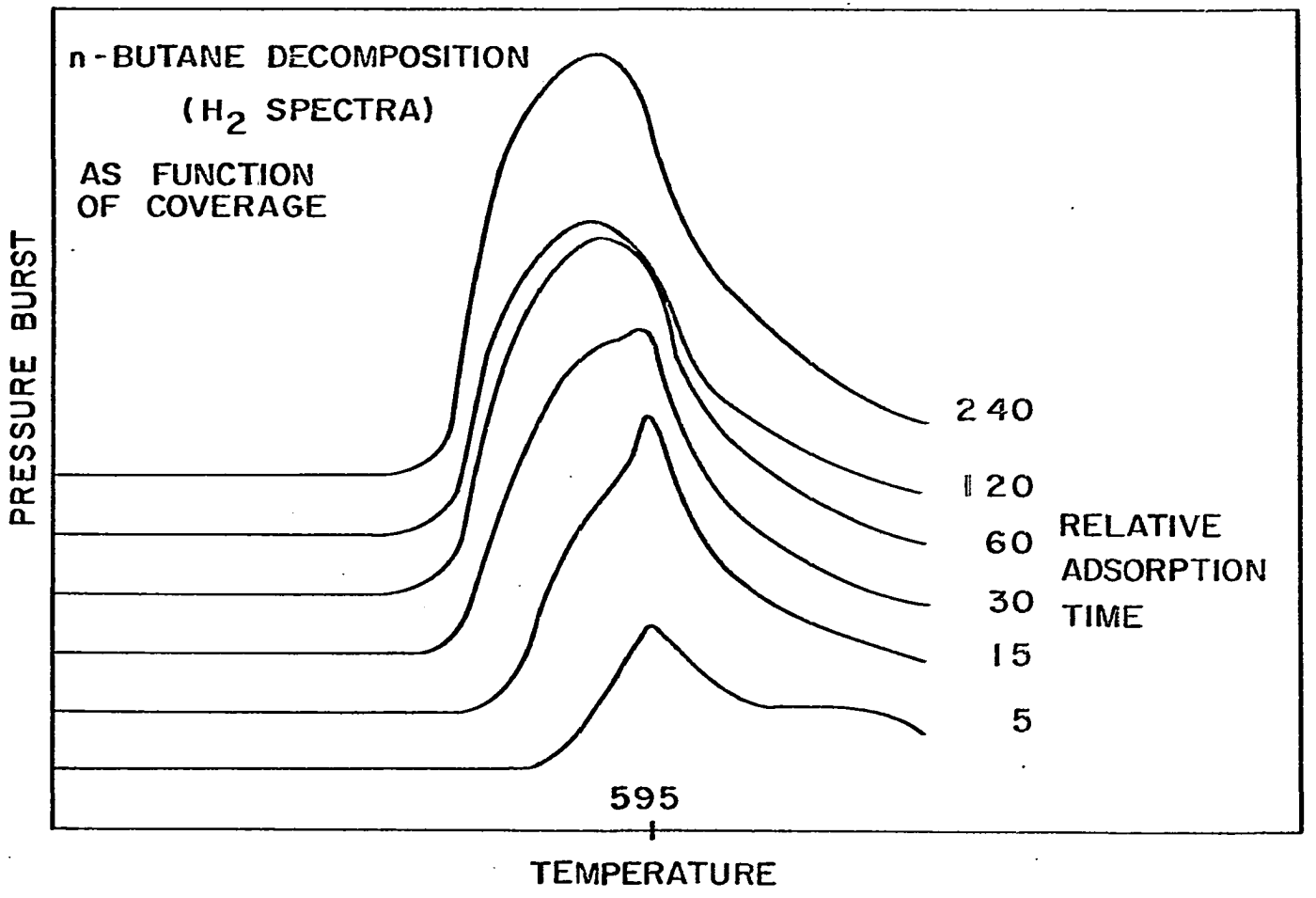

Figure 50. n-Butane decomposition spectra as a function of coverage

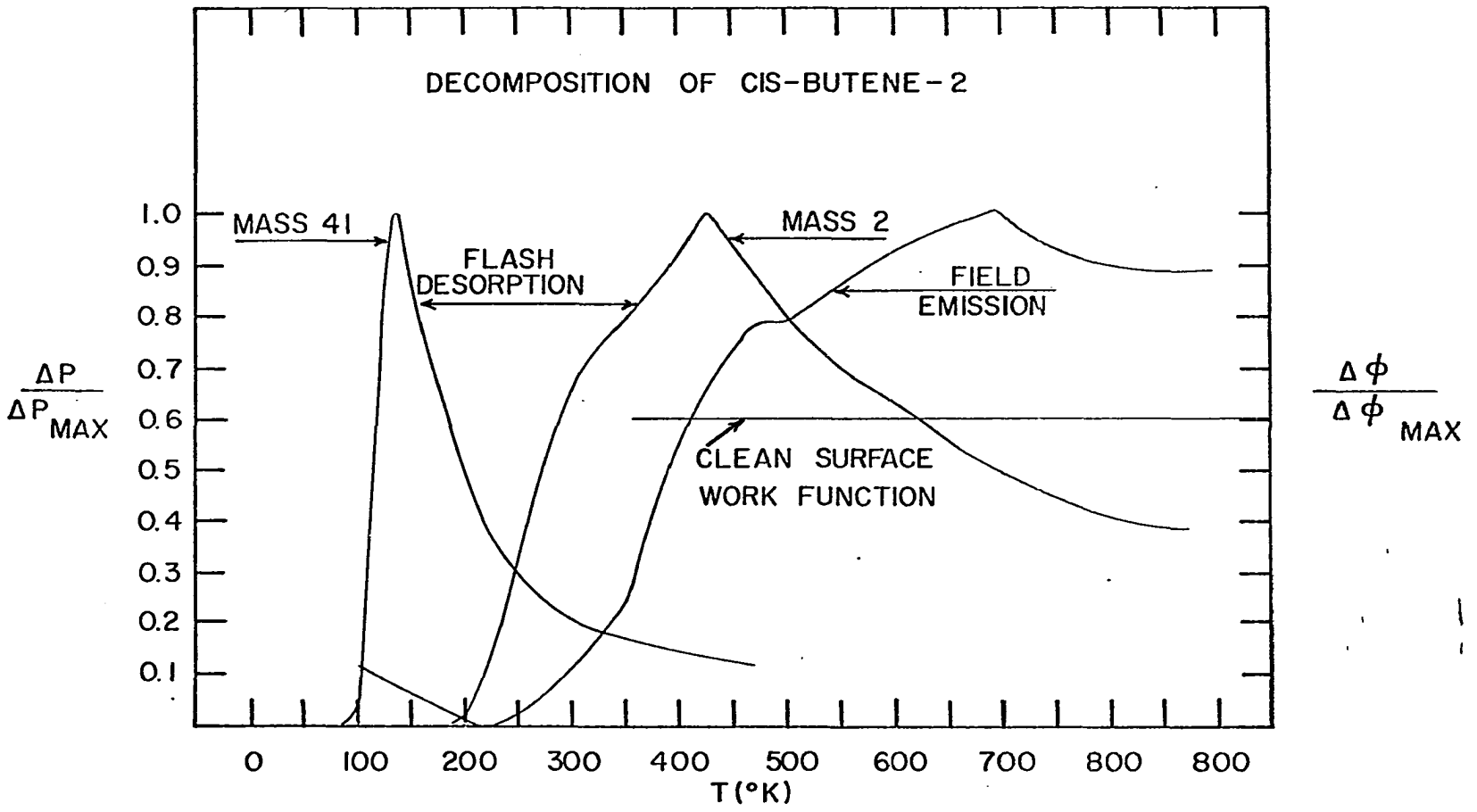

Figure 51. Comparison of normalized plots of pressure burst (FFS) and work function (FEEM) for cis-2-butene as a function of temperature

ERRATUM

The axes chosen to generate the hybrid d-orbitals in my presentation are rotated 45° from those ordinarily employed. The effect of using the proper axis would be to direct the t_{2g} orbitals for bulk metal atoms toward the corners of the body centered cube. This would result in the t_{2g} orbitals being lowered in energy relative to e_g orbitals. Type 1 bonding would, with this choice of coordination axes, involve suitably electron deficient t_{2g} orbitals. Back bonding in Type 2 bonding would involve suitably electron rich e_g orbitals.

Type 2 bonding would, however, still fail to account for the field emission observations reported in this presentation.